Title
Nuclear Magnetic Resonance Studies of Electronic Nematicity in Iron-based Superconductors

Author
Kissikov, Tanat

Publication Date
2021

Peer reviewed|Thesis/dissertation

Nuclear Magnetic Resonance Studies of Electronic Nematicity in Iron-based Superconductors

By

TANAT KISSIKOV

DISSERTATION

Submitted in partial satisfaction of the requirements for the degree of

DOCTOR OF PHILOSOPHY

in

Physics

in the

OFFICE OF GRADUATE STUDIES

of the

UNIVERSITY OF CALIFORNIA

DAVIS

Approved:

Nicholas J. Curro, Chair

Rena Zieve

Richard T. Scalettar

Committee in Charge

2021

Contents

List of Figures

List of Tables

Abstract

Nuclear magnetic resonance studies of ^{75}As under uniaxial stress were conducted on the parent and Co-doped $BaFe_2As_2$ iron-based superconductors. An NMR strain probe, that incorporates piezoelectric-based apparatus from Razorbill Instruments, was designed to apply the uniaxial stress. Nuclear quadrupolar splittings of the parent compound were measured as a function of strain. The electric field gradient tensor responds linearly to the presence of a strain field in the paramagnetic phase. The nematic susceptibility was extracted from the slope of this linear response as a function of temperature and it diverges near the structural transition. The detailed spin-lattice relaxation rate dependence on strain was measured for the parent $BaFe_2As_2$. The magnetic fluctuation spectrum in the paramagnetic phase acquires an anisotropic response in spin-space upon application of a tetragonal symmetry-breaking strain field. This result unveils an internal spin structure of the nematic order parameter, indicating that electronic nematic materials may offer a route to magneto-mechanical control. A second horseshoe device was used to apply strain, and the in-plane anisotropy of spin-lattice relaxation rate under uniaxial stress was measured in Co-doped $BaFe_2As_2$. The anisotropy reaches a maximum of 30% at T_N, and the recovery data reveal that the glassy behavior of the spin fluctuations present in the twinned state persist in the fully detwinned crystal.

Chapter 1

Introduction

Iron-based superconductors have rich phase diagrams with several competing degrees of freedom - lattice, orbital, and magnetic [10, 11]. At high temperatures, the parent undoped compounds are tetragonal paramagnets and at lower temperatures they undergo simultaneously an orthorhombic structural phase transition and an antiferromagnetic spin density wave transition. Under hole or electron doping, the structural and magnetic orders get suppressed and at certain doping levels superconductivity emerges.

Early NMR measurements [4] showed large EFG change across the structural phase transition that were inconsistent with the orthorhombicity of the lattice constant of less than 1%. This was further confirmed by the resistivity measurements under mechanical uniaxial stress [3]. This inconsistency has since been explained in terms of electronic nematicity, in which the electronic degrees of freedom break tetragonal symmetry. Since the lattice is coupled to and responds to the electronic system. Thus, relevant low energy physics is dominated by the *electronic nematicity* - the tendency of degenerate iron d-orbitals to spontaneously split in energy.

This work presents ^{75}As NMR studies under uniaxial stress of the parent $BaFe_2As_2$ and $Ba(Fe_{1-x}Co_x)As_2$ with doping level $x = 0.048$. The next two chapters focus on the basics of NMR and the details of the NMR strain probe. The fourth chapter discusses electronic

nematicity and nematic susceptibility. In the fifth chapter EFG measurements are presented that let us probe local nematic susceptibility. The first strain measurements appear in chapter six. $Ba(Fe_{1-x}Co_x)As_2$ with doping level $x = 0.048$ NMR measurements under strain were among the first experiments that showed the in-plane spin-lattice relaxation anisotropy in the detwinned states. This result motivated us to continue more precise NMR measurements under strain of the spin-lattice relaxation rate using the CS100 strain device. These experiments show the close relationship between the spin degrees of freedom and the electronic nematic order. The seventh chapter is the highlight of our work where our experimental results reveal the internal spin structure of nematic order in $BaFe_2As_2$.

Chapter 2

Solid State NMR

2.1 Pulsed NMR

Pulsed NMR spectroscopy is a great tool to study magnetic and electronic properties of solids. By applying a sequence of pulses one can obtain a spectral response of a collection of nuclei. This response in turn depends on the environment in which these nuclei are present. In this chapter we will focus on basics of NMR (Free induction decay, Spin Echo) and different measurements (Knight shift, Spin-Spin and Spin-Lattice Relaxation, Quadrupolar Splitting) that can be performed to obtain information about a material under study .

2.1.1 Nuclear Magnetic Moment

The presence of a nuclear magnetic moment allows one to do NMR. If a given nucleus has an uneven number of protons or neutrons or both, it usually has a non-zero magnetic moment, μ, and a total angular momentum, L, and one can consider these two vectors as parallel [12]. We can then write

$$\hat{\mu} = \frac{ge}{2m}\hat{L} \tag{2.1}$$

where g is the g-factor associated to the magnetic moment of a nucleus, e is the electron charge and m is the mass of the proton. The proportionality constant, $ge/2m$ is called a

Isotope	Spin I	Natural Abundance %	Gyromagnetic ratio $\gamma/2\pi \cdot 10^6$ i.e. MHz per Tesla
^{1}H	1/2	100	42.58
^{2}H	1	0.02	6.54
^{3}He	1/2	0.0001	32.44
^{7}Li	3/2	92	16.55
^{13}C	1/2	1.1	10.71
^{19}F	1/2	100	40.06
^{23}Na	3/2	100	11.26
^{29}Si	1/2	4.7	8.46
^{35}Cl	3/2	75	4.17

Table 2.1: Gyromagnetic ratios and abundances of some nuclei [9]

gyromagnetic ratio γ and has a unique value for a given nucleus. Some of them are shown in Table 2.1. When placed in an external magnetic field, $\vec{H}_0$ [1], the magnetic moment will experience a torque and its associated angular momentum will precess around $\vec{H}_0$. The nuclear spin Hamiltonian in an external magnetic field can be written in the following way:

$$\hat{\mathcal{H}} = -\hat{\mu} \cdot \vec{H}_0 = -\gamma \hat{L} \cdot \vec{H}_0 \tag{2.2}$$

The expectation value of $\hat{L}$ is given as:

$$\frac{d\langle \hat{L} \rangle}{dt} = \hat{\mu} \times \vec{H}_0 \tag{2.3}$$

The rate of precession is equal to $\omega_0 = \gamma H_0$ and is called the Larmor frequency. It is important to note that the angular momentum expectation value has the same form as the precession of a classical spin.

[1] In Gaussian units $\mathbf{B} = (1 + 4\pi\chi)\,\mathbf{H}$. In the paramagnetic state, χ is normally very small and we can take $\mathbf{B} \approx \mathbf{H}$.

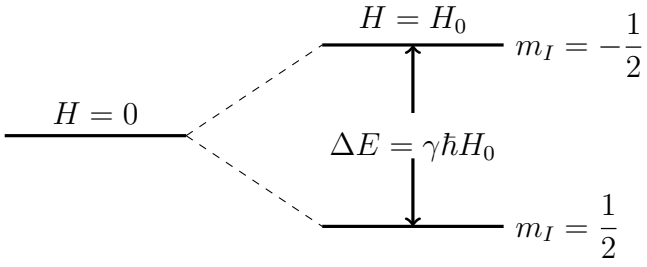

Figure 2.1: Energy levels in a magnetic field of a system with the nuclear spin $I = 1/2$

2.1.2 Resonance phenomena

Let's consider a nucleus with nonzero nuclear spin that is placed in a uniform external magnetic field H_0. The Hamiltonian is:

$$\hat{\mathcal{H}} = -\hat{\mu} \cdot \vec{H_0} \tag{2.4}$$

where $\hat{\mu} = \gamma\hbar\hat{I}$ where we introduce I for the nuclear spin. If $\vec{H} = H_0\hat{z}$ then the energy of interaction with the applied magnetic field [13]:

$$E = -\mu_z H_0 = -\gamma\hbar H_0 I_z \tag{2.5}$$

The allowed values of I_z are $m_I = I, I-1, ..., -I$ and $E_m = -m_I\gamma\hbar H_0$. Let's consider a hydrogen nucleus H, where $\gamma/2\pi = 42.58MHz$ and nuclear spin is $I = 1/2$. In a uniform magnetic field it will have two energy levels corresponding to $E_m = \pm\frac{1}{2}\gamma\hbar H$ (Fig. 2.1). The energy difference is

$$\Delta E = \gamma\hbar H_0 \text{ or } \Delta E = \hbar\omega_0 \tag{2.6}$$

So if we irradiate our nucleus with an electromagnetic field of the right frequency, $\hbar\omega = \Delta E$ we can excite nuclear spin transitions. For example, for a hydrogen nucleus in a 5T magnet, the resonance frequency would be at $\omega_0 = 42.58MHz/T \cdot 5T = 212.9MHz$. By sweeping ω at fixed field we can map out the NMR spectrum.

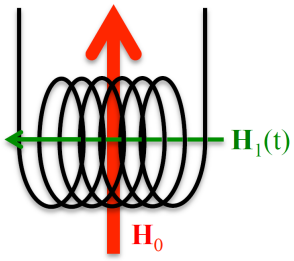

Figure 2.2: Schematic diagram of an NMR coil. $\vec{H}_0$ is a static external magnetic field and $\vec{H}_1(t)$ is a time-dependent magnetic field [1].

2.1.3 Rotating Reference Frame

To excite nuclear spins from a lower to a higher energy states we need to perturb the nuclear spin system. We need to apply an oscillating magnetic field whose frequency is equal to the resonance frequency of a nucleus. Let's write down the Hamiltonian for a single nuclear spin in a static external magnetic field $\vec{H}_0 = H_0\hat{z}$ with a perpendicular time varying magnetic field $H_1 = H_{1x}\cos(\omega t)$ (see Fig. 2.2):

$$\begin{aligned} \mathcal{H} &= \mathcal{H}_0 + \mathcal{H}_1 \\ \mathcal{H} &= -\gamma\hbar I_z H_{0z} - \gamma\hbar I_x H_{1x}\cos(\omega t) \end{aligned} \tag{2.7}$$

If one works out the equation of motion of a nuclear spin in an external magnetic field using quantum mechanics then one arrives at an expression that is identical to the classical one. This allows us to draw some classical analogies to explain the basic physics of NMR. One of the useful tools is the rotating reference frame. Let's go back to Eq. 2.3. It can be solved using methods of differential equations. However, it's more useful to use a rotating reference frame. If we define $D\vec{\mu}/Dt$ as the rate of change of $\vec{\mu}$ as seen from a reference frame rotating with frequency Ω with respect to laboratory frame, then we can write [14]:

$$\frac{d\vec{\mu}}{dt} = \frac{D\vec{\mu}}{Dt} + \Omega \times \vec{\mu} \tag{2.8}$$

Combining 2.2, 2.3 and 2.8 we find that

$$\frac{D\vec{\mu}}{Dt} = \gamma\vec{\mu} \times (\vec{H} + \frac{\vec{\Omega}}{\gamma}) \tag{2.9}$$

In a rotating reference frame the magnetic moment precesses around an effective field $\vec{H}_{eff} = \vec{H} + \vec{\Omega}/\gamma$. This tells us that if we choose a rotating frame that rotates in the opposite direction to the spin precession in the stationary frame with an angular velocity of γH then the spin will be stationary in a rotating reference frame. This allows us to get rid of the time dependence in the nuclear spin Hamiltonian.

2.1.4 Free Induction Decay

In thermal equilibrium, the nuclear magnetization is parallel to the static external magnetic field $\vec{H}_0$. If we turn on the time dependent magnetic field $\vec{H}_1(t)$ that satisfies the resonance condition then the nuclear magnetization would rotate around the $\vec{H}_1$. By applying a $\pi/2$ pulse, which turns on and off $\vec{H}_1$, we can turn the nuclear magnetization perpendicular to a static external field H_0. Following the $\pi/2$ pulse the nuclear magnetization would precess around $\vec{H}_0$ in the plane perpendicular to $\vec{H}_0$. Due to interactions of the nuclear spins with its surroundings the nuclear magnetization would relax back to equilibrium to align along $\vec{H}_0$. During that process the precessing nuclear magnetization will generate an emf via Faraday's law in the same coil that was used to excite nuclear spins. This detected signal is called the free induction decay or FID.

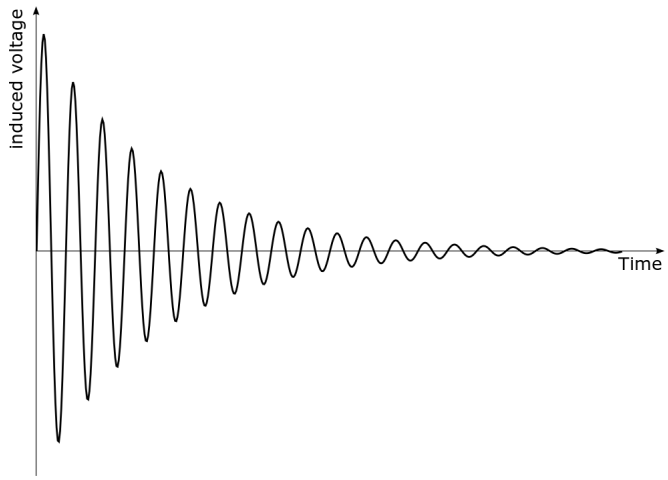

Figure 2.3: An FID oscillates at the Larmor frequency and decays exponentially over time. The typical timescale and voltage are on the order of μs and μV respectively.

2.1.5 Spin Echo

A technique in pulsed NMR is the Spin Echo, discovered by Erwin Hahn [15]. In principle one can perform a single $\pi/2$ pulse and observe the FID as discussed in the previous section. However, there are two problems here. First, there will be ringing that will add extra noise. The second has to do with dephasing of nuclear spins. There are two contributions to dephasing. First, an external static magnetic field is not perfectly uniform and will have some width ΔH_0. Second is the nuclear spin-spin interaction. External field inhomogeneity can dephase spins faster than the spin-spin interaction. As a result we lose useful information. If one applies a specific sequence of pulses then it's possible to cancel out the effects of field inhomogeneity and ringing. This sequence is called Spin Echo and consists of $\pi/2 - \tau - \pi - \tau - echo$. After applying $\pi/2$ we let the system of nuclear spins to dephase for some time τ after which we apply another π pulse that inverts all spins and has them rephase. All of the NMR measurements in this thesis were carried out using the echo technique.

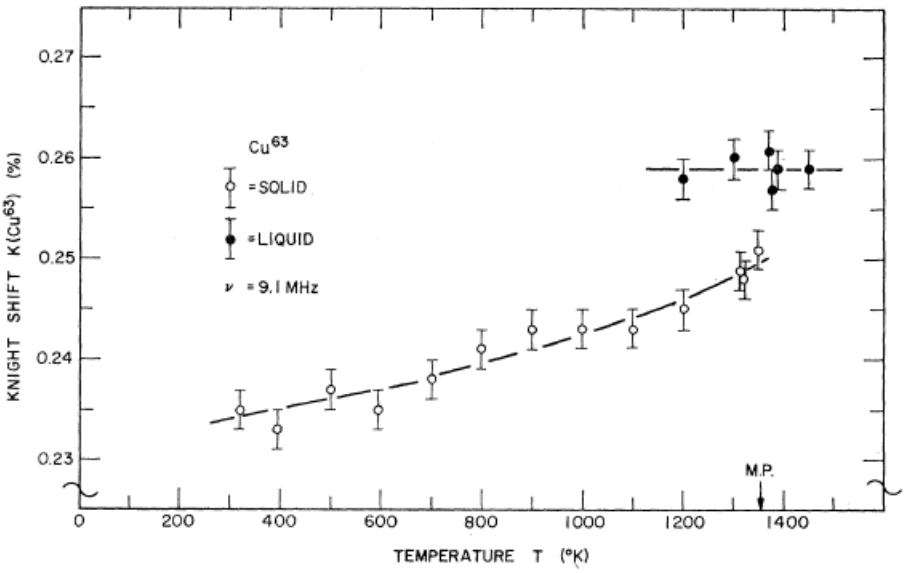

Figure 2.4: Knight shift of Cu as a function of temperature [2].

2.2 NMR Measurements

2.2.1 Knight Shift

Nuclei within materials have different resonance frequencies than isolated nuclei. This shift in resonance frequency is known as the Knight shift, which is named after Walter Knight who first observed it in metals [16]. In general, the Knight shift can be written as

$$\begin{aligned} \omega &= \omega_0(1+K) \\ K &= A\chi \end{aligned} \tag{2.10}$$

where A is the hyperfine coupling, χ is the Pauli paramagnetic susceptibility per atom [17], K is the Knight shift, ω_0 is the resonance frequency of a bear nucleus. The observed shifts in metals reflects the local magnetic field produced by the conduction electrons. Normally for simple metals, the Knight shift is nearly temperature independent, but any temperature dependence reveals important aspects of the material. Fig 2.4 shows typical Knight shift behavior of Cu at high temperatures. The slight dependence on temperature might be due to the thermal contraction that affects the magnetic susceptibility χ.

2.3 Electric Field Gradient

Any nucleus with a nuclear spin $I > 1/2$ has non-zero quadrupole moment. A nucleus that has non-zero quadrupole moment has a non-spherical charge distribution that is going to be affected by the electric field gradients that the nucleus experiences due to a non-symmetric charge distribution around it. The effective quadrupole interaction can be written in the following way [12]:

$$\mathcal{H}_{\mathcal{Q}} = \frac{eQ}{4I(2I-1)}[V_{zz}(3I_z^2-I^2) + (V_{xx}-V_{yy})(I_x^2-I_y^2)] \tag{2.11}$$

where $V_{\alpha\beta} = \partial^2 V/\partial x_\alpha \partial x_\beta$ is the gradient of electric potential at the nucleus, Q is the quadrupole moment, I is the total nuclear spin, e is the proton charge. Here we introduce a common convention. We define *asymmetry parameter* η in the following way:

$$\eta = \frac{V_{xx}-V_{yy}}{V_{zz}} \tag{2.12}$$

Also, from the Laplace equation, $\nabla^2 V = 0$, we get

$$V_{xx} + V_{yy} + V_{zz} = 0 \tag{2.13}$$

Later, we will use η as a microscopic electronic nematic order parameter. It should be pointed out that $V_{\alpha\beta}$ is a second rank tensor:

$$\begin{pmatrix} V_{xx} & V_{xy} & V_{xz} \\ V_{yx} & V_{yy} & V_{yz} \\ V_{zx} & V_{zy} & V_{zz} \end{pmatrix}$$

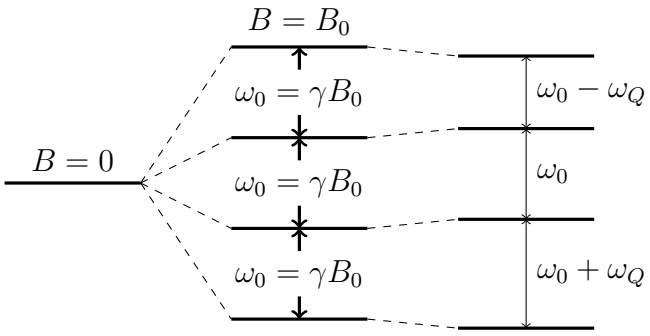

Figure 2.5: Splitting of energy level in a magnetic field

In the case of ^{75}As in the $BaFe_2As_2$ the tetragonal crystal symmetry and the Laplace equation simplify this tensor to:

$$\begin{pmatrix} \frac{1}{2}(\eta-1)V_{zz} & 0 & 0 \\ 0 & -\frac{1}{2}(\eta+1)V_{zz} & 0 \\ 0 & 0 & V_{zz} \end{pmatrix}$$

The effective quadrupole interaction can be written:

$$\mathcal{H}_{\mathcal{Q}} = \frac{eQV_{zz}}{4I(2I-1)}(3I_z^2 - I^2) \tag{2.14}$$

If we treat $\mathcal{H}_{\mathcal{Q}}$ as small compared to magnetic interaction then we can use the first order perturbation theory to find the energy shifts due to quadrupolar interaction. The full Hamiltonian can be written as:

$$\mathcal{H} = -\gamma\hbar H_0 I_z + \frac{eQV_{zz}}{4I(2I-1)}(3I_z^2 - I^2) \tag{2.15}$$

The energy levels are given:

$$E_m = -\gamma\hbar H_0 m + \frac{eQV_{zz}}{4I(2I-1)}[3m^2 - I(I+1)] \tag{2.16}$$

The effect of the quadrupolar interaction can be illustrated as shown in Fig. 2.5.

2.4 Spin-Lattice Relaxation

Using Bloch's equations we can derive a simple quantitative formula for spin-lattice relaxation. The Bloch's equations are the equations of motion for the macroscopic nuclear magnetization which is the sum of all the nuclear magnetic moments. For the static external magnetic field along the $\hat{z}$ we can write the Bloch's equations [12]

$$\begin{aligned} \frac{dM_z}{dt} &= \gamma(M \times B)_z + \frac{M_0 - M_z}{T_1} \\ \frac{dM_x}{dt} &= \gamma(M \times B)_x - \frac{M_x}{T_2} \\ \frac{dM_y}{dt} &= \gamma(M \times B)_y - \frac{M_y}{T_2} \end{aligned} \tag{2.17}$$

where M is the nuclear magnetization, T_1 is the spin-lattice relaxation rate, and T_2 is the spin-spin relaxation rate. We can solve for M_z using the first eqaution:

$$M_z = M_0(1 - e^{-t/T_1}) \tag{2.18}$$

One way to think about nuclear relaxation mechanism is through the "spin temperature" i.e. where the system of N nuclei is in thermal equilibrium with the lattice that acts like heat bath. By irradiating the sample we increase the total energy of the nuclear spin system which after the pulse goes back to thermal equilibrium with the lattice.
The general expression for the spin-lattice relaxation rate due to a magnetic field applied in an arbitrary direction can be written in the following way:

$$\left(\frac{1}{T_{1,z}T}\right)_\mu = \frac{\gamma^2}{2} \lim_{\omega \to 0} \sum_{\mathbf{q},\alpha,\beta} \mathcal{F}^{(\mu)}_{\alpha\beta}(\mathbf{q}) \frac{Im\chi_{\alpha\beta}(\mathbf{q},\omega)}{\hbar\omega} \tag{2.19}$$

where $\mathcal{F}^{(\mu)}_{\alpha\beta}$ is the hyperfine form factor that depends on magnetic field direction μ and describes the nuclear-electron interaction [18], $\chi_{\alpha\beta}(\mathbf{q},\omega)$ is the dynamical magnetic susceptibility, and $\alpha, \beta = (x, y, z)$. The equation 2.19 is known as the Moriya formula [19]. This

formula comes from the following considerations. In general, the spin-lattice relaxation is given by:

$$\frac{1}{T_1} = \frac{\gamma^2}{2} \int_0^\infty \langle h_\perp(t)\, h_\perp(0) \rangle e^{i\omega_0 t} dt \tag{2.20}$$

where $\langle h_\perp(t)\, h_\perp(0) \rangle$ is the correlation function, $h_\perp$ is the component of $h(t)$ perpendicular to the static magnetic field. $h(t)$ is the fluctuating field of neighboring electrons. In the case of $BaFe_2As_2$ it's the fluctuating field at the ^{75}As nucleus due to the electrons of the four Fe atoms that surround it. By using the fluctuation-dissipation theorem we rewrite the correlation function in terms of dynamical susceptibility which enables us to get to 2.19 [12, 18].

2.5 Stretched Exponential Behavior of T_1

When we do the spin-lattice relaxation measurements to extract T_1 we fit it to the magnetization recovery function described in B.1 for the case of spin-3/2 nucleus. However, in some systems the spin-lattice relaxation behavior takes the form of stretched exponential [20]. That is normally the result of intrinsic inhomogeneity (in case of high quality crystals). Different nuclei in the system are in a different environment which affects the relaxation time. In such cases it's a common practice to analyze these systems using stretched exponential. The general expression for the stretched exponential relaxation [21]:

$$n = n_0 e^{-(\lambda^* \cdot t)^\beta} \tag{2.21}$$

where n is a relaxing quantity, λ^* is a characteristic relaxation rate, and the stretching exponent β is in the range $0 < \beta < 1$. In our case, $\lambda^* = T_1^{-1}$ and $n = M$ where M is the nuclear magnetization. β captures the width of the distribution. If $\beta = 1$ then it's the delta function distribution meaning all nuclei have the same relaxation rate. As β gets smaller relaxation distribution gets broader.

Chapter 3

Experimental Techniques and Instrumentation

3.1 Magnets

3.1.1 PPMS

The PPMS, Physical Properties Measurement System, is a 9T magnet with the possibility of doing field sweeps. In NMR experiments, one can do frequency sweeps to obtain spectra. If the spectrum is sufficiently wide, then one has to adjust the tuning and matching as frequency changes. This requires the presence of an experimenter to do that adjustment. The automation "field-sweep" script is thus very helpful. In this case, the NMR coil remains tuned to a fixed resonance frequency and only field is changed. We can use our custom-made "Fieldsweep" Python code to control the magnetic field values.

3.1.2 Oxford Magnet

The Oxford is an 11.7T magnet from Oxford Instruments. Unlike the PPMS magnet, the Oxford's magnetic field is fixed. It was charged in 2010 and it's been running very stable. It consists of several parts: a Nb_3Sn superconducting magnet immersed in liquid helium,

an insulation layer, and a liquid nitrogen space for extra shielding to reduce He boil off rate. The cooling of the sample space is done via a closed-cycle helium cryostat cooled by a Sumitomo compressor, and temperature control of the sample space is established by a resistive heating element.

3.1.3 Safety

Both magnets that we have in our lab are "wet" superconducting magnets, meaning they have to be always immersed in liquid helium. If the magnet temperature rises above 4.2K, the windings of the magnet will become resistive, which in turn will generate heat that will cause a quench - a rapid boil-off of helium. This potentially can lead to an explosion. Another potential hazard is asphyxiation due to a large amount of helium gas in a closed room that can displace oxygen, which will lead to oxygen deprivation. To avoid quenching, helium/nitrogen transfers have to performed regularly. For the PPMS magnet, if the magnet is on, then the liquid level can't be less than 40%. However, it's important to be on the safe side so we normally fill the magnet when it gets down to 60% level. Once the magnet is filled, this gives us 4-5 days before the next fill. As for the Oxford magnet, we don't want the liquid level go below 30%. The boil-off rate for the Oxford magnet is about 1.5%/day. Therefore, if it's filled to about 60% then one has about 20 days before the next fill. However, it's a good practice to constantly monitor liquid levels on the magnets. Working in the lab is like babysitting, it's better to take a look and make sure that everything is ok. The liquid helium transfer has to be done by at least two qualified personnel. Our lab convention is that whoever is running measurements on the system is responsible for maintaining liquid levels.

3.2 NMR Probes

We have multiple probes in our lab that are designed to be compatible with the PPMS and Oxford magnets. Oxford probes are longer than PPMS ones. Therefore, we have an extension that allows us to use Oxford probes on the PPMS magnet, since the distance to the sweet spot of the magnet in the PPMS is shorter than in Oxford.

3.2.1 PPMS Probe

The probe that we used for strain experiments was designed also by Quantum Design, Inc. For the purpose of our experiments we had to make several modifications to the original probe in order to mount the CS100 strain device.

3.2.2 Goniometer Probe

Our dual axis goniometer probe design is based on [22]. It consists of multiple worm gears connected together with tuning rods that allow in situ orientation change with respect to an external magnetic field. Since a lot of our studies focus on anisotropic properties of materials it is important to have the ability to change the orientation of a sample without exposing it to big thermal cycling (which can cause degradation of a sample). Figure 3.1 is a schematic diagram of our dual axis goniometer probe. The stage (1) can be rotated around *y-axis* (red) using the driving worm gear (7) which meshes with worm gear (4) which, in turn, meshes with gear (2). The drive worm (3) meshes with the worm gear (5) that rotates the stage around *x-axis*. Note that these two degrees of freedom are not independent, so that the *y-axis* can be rotated around the *x-axis*. The magnetic field lies along the *z-axis*.

We define the angle of rotation around the *x-axis* as α and the angle of rotation around the *y-axis* as β. If we rotate around *y-axis* first and then *x-axis*, the final orientation of sample's

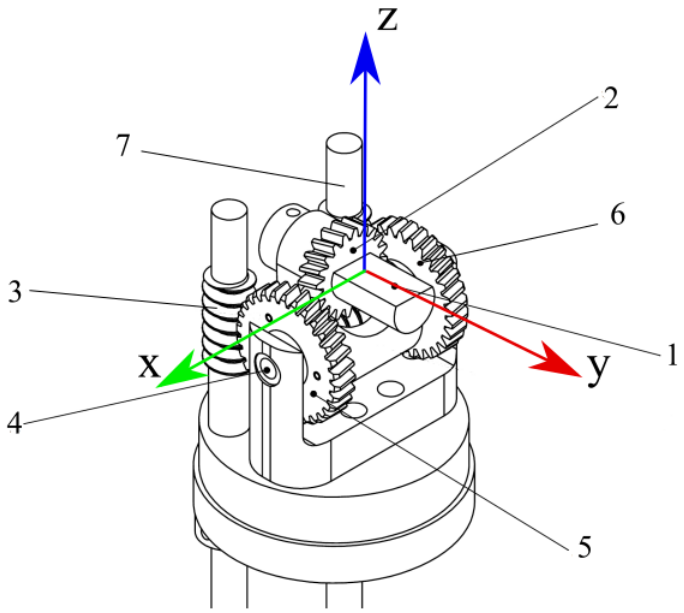

Figure 3.1: Dual axis goniometer probe head. Labels are defined in the text.

$\hat{c}$ axis can be found using rotation matrices:

$$R_y = \begin{pmatrix} \cos\beta & 0 & \sin\beta \\ 0 & 1 & 0 \\ -\sin\beta & 0 & \cos\beta \end{pmatrix}$$

$$R_x = \begin{pmatrix} 1 & 0 & 0 \\ 0 & \cos\alpha & -\sin\alpha \\ 0 & \sin\alpha & \cos\alpha \end{pmatrix}$$

The vector being rotated is the $\hat{c} = \{0, 0, 1\}$ axis of the sample (originally along the $z - axis$ parallel to $\vec{\mathbf{H}}_0$)

$$R_x R_y \begin{pmatrix} 0 \\ 0 \\ 1 \end{pmatrix} = \begin{pmatrix} \sin\beta \\ -\sin\alpha\cos\beta \\ \cos\alpha\cos\beta \end{pmatrix}$$

Now we need to convert our α and β angles into polar angles θ, ϕ relative to $\vec{\mathbf{H}}_0$. Our rotated $\hat{c}$ vector is:

$$\hat{c}' = \sin\beta \cdot \hat{x} - \sin\alpha\cos\beta \cdot \hat{y} + \cos\alpha\cos\beta \cdot \hat{z}$$

From this equation we get:

$$\cos\theta = \cos\alpha\cos\beta \tag{3.1}$$

$$\cos\phi = \frac{\sin\beta}{\sin\theta} = \frac{\sin\beta}{\sqrt{1-\cos^2\alpha\cos^2\beta}} \tag{3.2}$$

Equations 3.1 and 3.2 thus give the orientation of the crystal relative to the field direction $\vec{\mathbf{H}}_0$. Note that if $\alpha = 0$, then we have essentially a single-axis goniometer by changing β. This axis has a high gear ratio (600:1) giving us precision of about 0.2° in β.

3.2.3 NMR tank circuit

To excite the nuclei of a specimen there is an important component of NMR probes called the tank circuit, which is sketched in Fig. 3.2 below. It consists of two tunable capacitors - tuning capacitor C_t and matching capacitor C_m - and an inductive coil L that has resistance R. An RF signal arrives through the 50 Ohm semi-rigid coaxial cable. To effectively deliver input power to the sample we need to make sure that the circuit is appropriately tuned. That means we need to minimize the reflected power. The reflected power can be calculated using reflection coefficient ρ

$$\rho = \frac{Z - 50\Omega}{Z + 50\Omega} \tag{3.3}$$

where Z is the complex impedance of our circuit which is a function of C_t and C_m. It is equal to

$$Z = \frac{1}{i\omega C_t + (i\omega L + R)^{-1}} + \frac{1}{i\omega C_m} \tag{3.4}$$

The minimum reflected power we can get is equal to 0. That means $\Re[Z] = 50\Omega$ and $\Im[Z] = 0\Omega$. This condition, when we match the impedance of the tank circuit to 50Ω, is called the resonance condition.

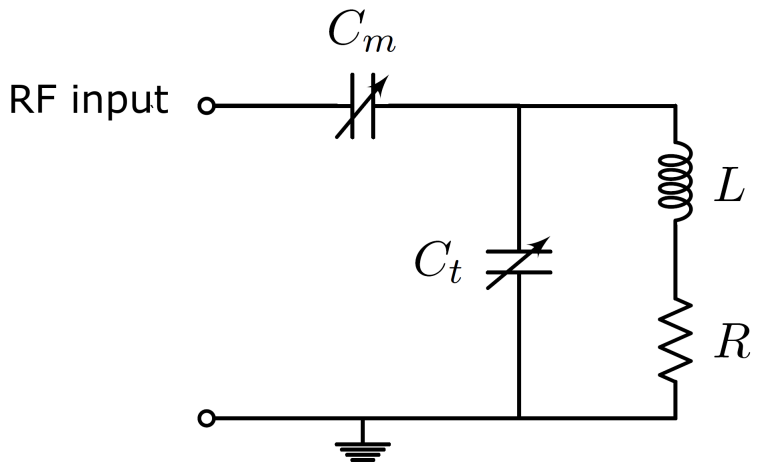

Figure 3.2: NMR tank circuit [1]

3.3 CS100 Strain Device

Our initial NMR measurements under strain used a horse-shoe clamp device (Fig. 3.3), in which the crystal is suspended on fine wires and tensile stress is applied by tightening a screw [23]. In this case, stress on the order of a few MPa is applied at room temperature, but the strain is poorly controlled at cryogenic temperatures due to differential thermal contraction between the clamp and the crystal. Furthermore, stress can only be applied at room temperature, requiring significant adjustments to the probe head with the possibility of misalignment. Finally, thermal contraction may give rise to unbalanced torques and hence crystal misalignment at low temperatures.

The CS100 device is a piezoelectric-based apparatus developed by Hicks and collaborators [24], and commercially available from Razorbill Instruments Ltd. (Edinburgh, UK). It is superior because it offers precision control of the strain through a combination of piezoelectric stacks and a capacitive position sensor. This combination enables active feedback control to achieve sub-nanometer position control over time scales of several hours.

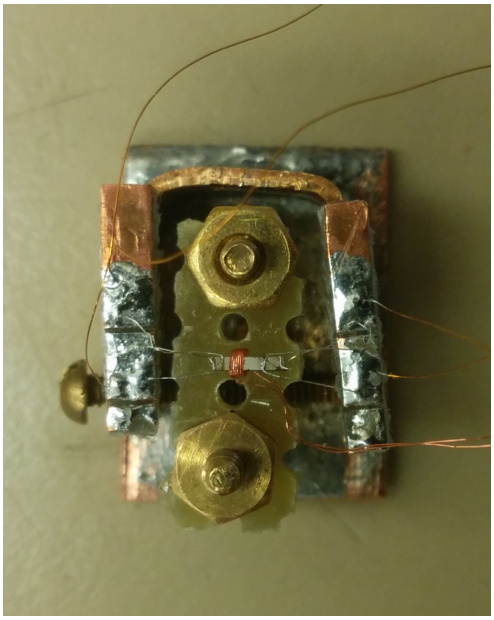

Figure 3.3: Horseshoe strain device

3.3.1 Principles of Operation

The CS100 consists of two sets of piezoelectric stacks, one inner and two outer, that can apply either tensile or compressive stress in situ through the application of a bias voltage, as illustrated in Fig. 3.4. The outer stacks expand the displacement gap (the gap between parallel plate capacitors inside CS100 cell) with positive voltage, and the inner stack contracts the displacement with positive voltage. Because the piezoelectric stacks are arranged to cancel out thermal expansion, strains induced by differential thermal expansions are significantly reduced, and can be overcome by applied voltage to the piezo stacks.

In tandem, the two sets of stacks can cover a range of approximately 6 μm, depending on the temperature and applied voltages, as shown in Fig. 3.5 The voltage is controlled via two high performance voltage amplifiers (PDm200B, PiezoDrive), and a 14-bit USB digital-to-analog converter (USB-6001 DAQ, National Instruments) interfaced with a desktop computer. The four voltage leads are connected via 0.8 mm PTFE insulated copper cables to the top of the probe. At the top of the probe, the four voltage wires are soldered to a 4-pin panel mount hermetic LEMO connector.

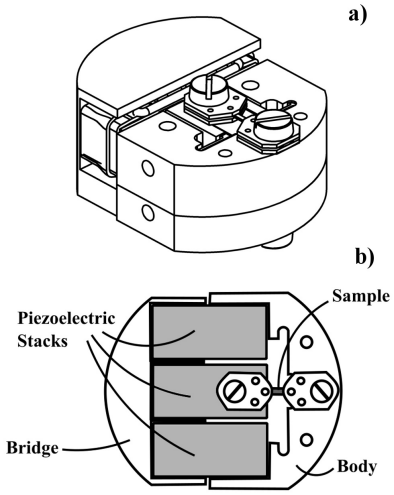

Figure 3.4: (a) Diagram of the Razorbill Instruments CS100 device, showing (b) the piezoelectric stacks and the mounted sample. The diagram is taken from the Razorbill Instruments Datasheet for CS100.

The displacement is measured by a parallel-plate capacitor integrated within the CS100 device, with a nominal spacing of approximately 40-60 μm and an area of 2.5×2 mm. Two SC-type ultra miniature coaxial cables connected to the parallel capacitor plates are also connected to the top of the probe via hermetic panel-mount BNC connectors. The capacitance is measured with an Andeen-Hagerling Capacitance Bridge (AH2550A), with a resolution of 0.5 attofarads at 1 kHz. This device enables us to measure the displacement with sub-nm precision.

3.3.2 NMR Strain Probe Head

The NMR probe consisted of a Model 450A/B PPMS Multi-function probe that was originally designed with a series of electrical connections at the base to connect to the PPMS electronics. The advantage of this approach is that it enables us to easily connect electrical leads to the strained sample for resistivity measurements using the PPMS system. The CS100 cell is mounted several cm from the base, such that the sample is located in the region of the highest field homogeneity. Two tunable cryogenic capacitors (non-magnetic panel mount NMTM120CEK-2L, 1-120pF, Voltronics) are mounted above the cell, as shown

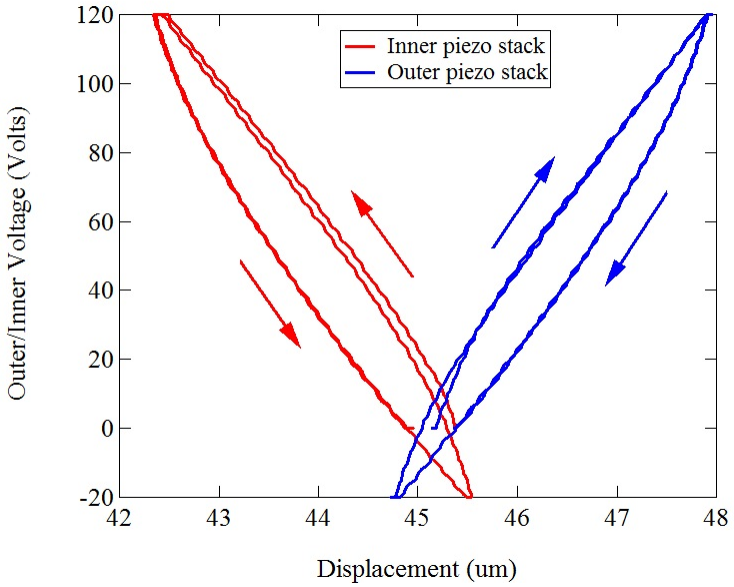

Figure 3.5: Voltage applied to the inner (red) and outer (blue) piezoelectric stacks versus the measured displacement at room temperature. Positive voltage expands the piezo stacks, leading to an expansion of the displacement for the outer stacks and a contraction of the displacement for the inner stacks. The response is hysteretic, and arrows indicate the sequence versus time.

in Fig. 3.6. These connect via a semi-rigid coaxial line to form a resonant circuit with the NMR coil. The CS100 chassis is fabricated from titanium, which has a low magnetic susceptibility and thus does not significantly affect the magnetic field homogeneity at the sample.

An important issue for the design of the probe is the isolation of the radiofrequency coaxial cable from the high voltage piezo driver lines as well as the sensitive capacitance coaxial cables. To achieve this isolation, the radiofrequency coax passes through a stainless steel tube up to the top of the probe to hermetic BNC connections. Shielded coaxial lines connect the RF electronics and capacitance bridge devices to the probe, as shown schematically in Fig. 3.7.

For this thesis we primarily measured $Ba(Fe,Co)_2As_2$. Single crystals are cut to dimensions of approximately 0.5 mm wide by 2 mm long by 0.1 mm thick. The length of the crystals is chosen to make sure we have enough space to glue the crystal from both ends to

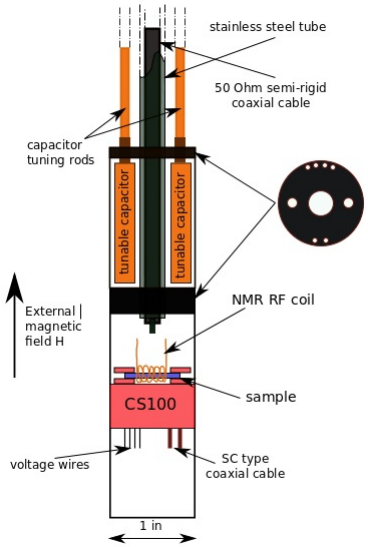

Figure 3.6: Schematic diagram of the probe head. High power radiofrequency pulses are delivered to the sample via a semi-rigid coaxial cable and a tuned tank circuit using two cryogenic capacitors. The CS100 device is mounted below at the sweet spot of the magnetic field. Four high power DC voltage wires for the piezoelectric stacks and two flexible coaxial cables for the capacitive displacement meter (not shown) go to the top of the probe.

CS100 cell's sample holders and enough space for the NMR coil in the middle. The samples were grown and prepared as described in Refs. [23] and [25]. Free standing rigid NMR coils with the appropriate inductance are placed around the sample (see Fig. 3.9), and the crystal is secured to the CS100 strain device by epoxy (UHU Plus 300 heat-cured epoxy resin).

To mount crystals with the magnetic field oriented parallel to the c-axis, a sample plate guide was used as shown in Fig. 3.8. First, two sample plates were fastened to the cell using M2 brass screws and aligned parallel using the sample plate guide, which itself is fastened to the cell using M1.6 screws. The distance between the two mounting pieces along the strain axis were chosen to ensure that the NMR coil fits in between and sits freely. A drop of UHU 300 heat-cure epoxy is then deposited to the two ends of the sample plates using a thin stainless steel wire. In principle, two thin wires should be placed along with epoxy so that crystal is aligned parallel to the cell's surface. After the sample is secured, another layer of epoxy is deposited to the upper surface of the sample. Sample plate spacers, which have been polished down to limit the epoxy thickness to 30-50 μm on both sides of the crystal,

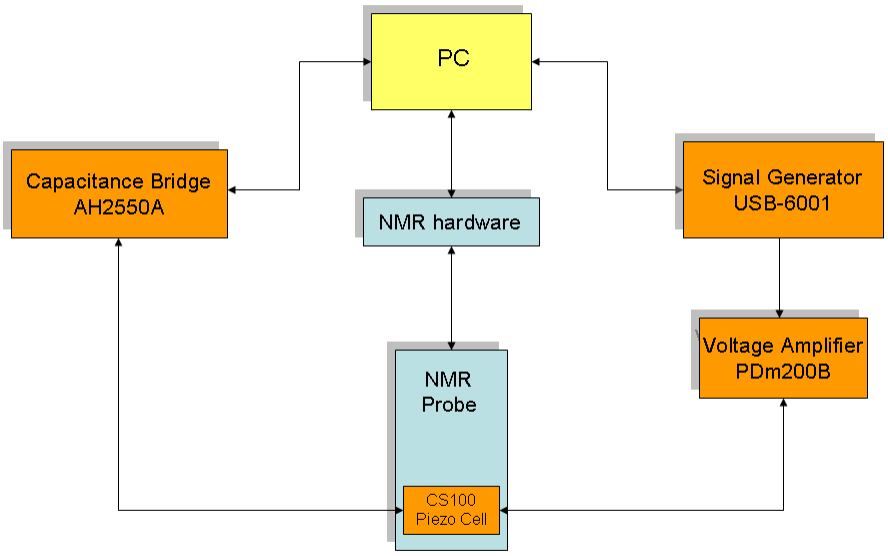

Figure 3.7: The piezoelectric stacks in the strain cell are controlled by voltage amplifiers via a signal generator controlled by the computer. The capacitive position sensor interfaces with a high precision capacitance bridge. The voltage applied to the piezo stacks is controlled via active feedback from the computer.

are placed on both the sample plates. Finally, the upper sample plates are placed above the sample plate spacers and epoxy, and fastened to the cell using M2 brass screws. The cell with the sample is then placed under a heat lamp to let the epoxy cure at around 75-80 °C for 40 minutes.

For crystals mounted with the field oriented perpendicular to the c-axis, we constructed a mounting device that consists of two blocks each one holding two smaller blocks that are glued so that enough space is created for the sample to be mounted (see Fig 3.9). Holes were tapped to secure the two mounting pieces on the cell using the M2 screws. The two slits are aligned along the strain axis under a Nikon SMZ800 microscope by carefully gluing two smaller blocks onto mounting piece using superglue, and with the modified mounting pieces we can use the sample plate guide. The crystal is placed into the NMR coil and then the whole thing is carefully lifted with tweezers, holding the ends of the NMR coil and making

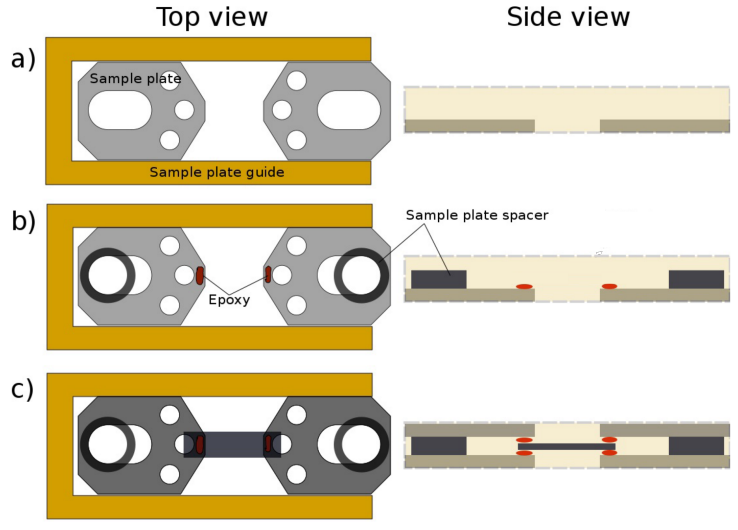

Figure 3.8: Mounting sequence: (a) The sample plates are aligned with the sample plate guide; (b) the sample is secured with epoxy; and (c) the upper sample plates are secured at a distance determined by the sample plate spacers.

sure that the crystal doesn't fall off, to put it on top of the slits. Then, using fine tools, such as needles, the crystal can be carefully pushed into the slits. After the crystal with the free standing NMR coil is placed between the holders, UHU Plus 300 heat-cured epoxy is deposited into the slits to fill the space between the crystal plates and the walls in the slits. The slits are sufficiently narrow and the viscosity of the epoxy is sufficiently high that we do not encounter any problems with the epoxy flowing out of the slits on the open sides. Nevertheless, the epoxy is filled in over a sequence of several small steps, and is allowed to cure each time. Epoxy curing consists of two stages. First, we use IR lamp to maintain the epoxy at 70° for about 45mins. Then, another 24 hours is needed to achieve good bonding.

In principle, the CS100 can also be rotated by 90 degrees, however in this case the strain axis is vertical, parallel to the applied field. This orientation is unacceptable, though, because the NMR RF field, $\vec{H}_1$, must be perpendicular to the applied field in order to induce a signal. Therefore, a solenoidal coil around the sample that is oriented along the strain axis would not work. We have had some success with a Helmholz coil design, which would enable the field to be oriented along the strain axis, while $\vec{H}_1$ is perpendicular to the applied field. However, the signal-to-noise for this orientation was significantly reduced. Alternatively, a

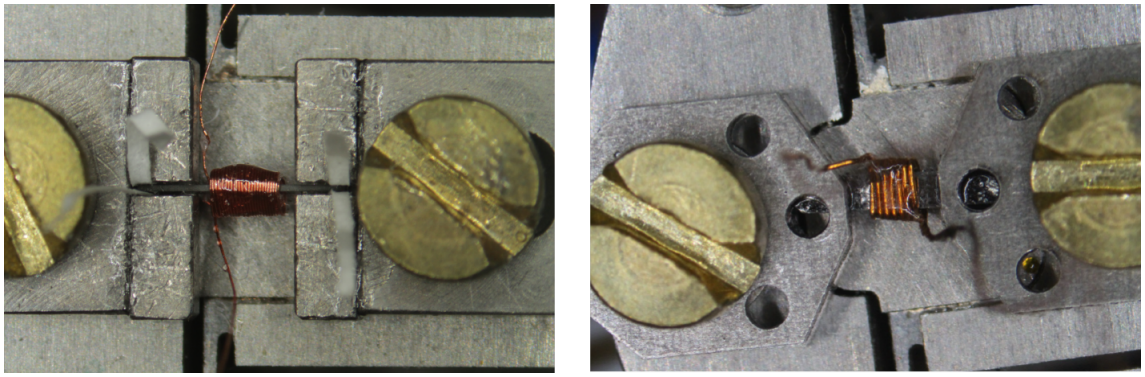

Figure 3.9: NMR coil and sample mounted for field parallel to the crystalline $\hat{c}$-axis (left) and perpendicular (right).

rigid coil that is larger than the sample, but oriented such that $\vec{H}_1$ has a component perpendicular to $\vec{H}_0$ can be used [23]. Note, however, that it is possible to investigate the in-plane anisotropy without orienting the strain axis along $\vec{H}_0$. By symmetry, negative (compressive) strain with $\vec{H}_0$ perpendicular to the strain-axis is approximately equivalent to positive (tensile) strain with $\vec{H}_0$ parallel to the strain axis. For materials with a sufficiently large Poisson ratio there are strains introduced along the directions perpendicular to the strain axis, and other strain modes such as $\epsilon_{xx} + \epsilon_{yy}$ may be present. As a result, the equivalence between the field directions and a real rotation of the sample is broken, which could produce asymmetries in quantities measured via this method. However, we have found linear behavior over a broad range of strains in the $BaFe_2As_2$ sample studied here, suggesting that these other modes do not play a significant role in this case [26].

3.3.3 PID control

The creep behavior of the piezoelectric actuators, in which the length changes at constant voltage, presents a challenge for long-term NMR measurements. After setting a new voltage or temperature, the displacement of the stacks drifts by several percent over the course of several minutes to hours. If the NMR properties under investigation are strain-sensitive, this creep can give rise to unacceptable errors. Long-term stability is also important for other measurements, such as specific heat, μSR, and neutron scattering where time duration is an

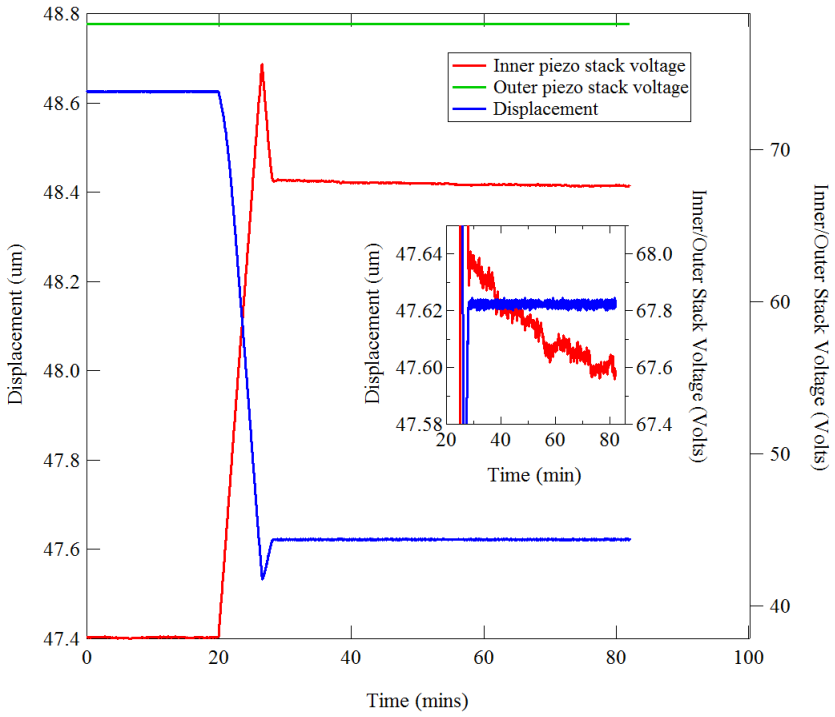

Figure 3.10: Displacement (blue), inner (red), and outer (green) stack voltages versus time. At approximately 20 mins, the setpoint displacement was set to 47.6μm. The setpoint was reached and stabilized by approximately 28 mins. The applied voltage drifted over time as the active feedback compensated for the drift of the piezoelectrics. The inset shows a closer look at voltage drift over time

important factor. For example, at large-scale facilities with limited beam time availability, waiting for the piezoelectric stacks to relax would be prohibitively expensive. In order to overcome these issues, we implemented active feedback control using a PID control loop. A Python script running on the computer uses the input signal from the capacitance bridge and determines an error based on a desired displacement setpoint. The output voltage is then determined based on this error signal. Depending on the setpoint, either the inner or the outer stack is used for the feedback control, while the other set of stacks is left to drift at a fixed voltage. Fig. 3.10 shows the time-dependence of the displacement and voltage after a new setpoint is implemented. Using this approach, we have been able to achieve displacements that stabilize quickly and remain stable over days with 0.9 nm rms fluctuations.

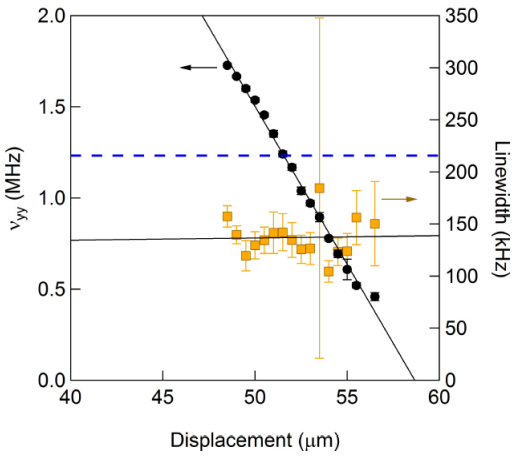

Figure 3.11: Quadrupolar splitting and quadrupolar linewidth versus displacement for the As site in $BaFe_2As_2$ at 138 K. The solid line is a linear fit to the data, and the dashed line is the value in the zero-strained case.

3.3.4 EFG control

Determining the strain, $\epsilon = (x - x_0)/L_0$, where x is the displacement and L_0 is the sample length, requires knowledge of the unstrained length, x_0. However, differential thermal contraction at cryogenic temperatures will give rise to finite strains, even if the crystal is secured at room temperature in zero strain. Although it is possible to employ a strain gauge to calibrate the displacement, a superior approach is to measure an intrinsic NMR property of the material of interest. An ideal quantity is the electric field gradient (EFG) asymmetry of a quadrupolar nucleus. The measured EFG of ^{75}As ($I = 3/2$) in $BaFe_2As_2$ is shown in Fig. 3.11 at $138K$. Above the structural transition, the EFG tensor at the As site has tetragonal symmetry, and therefore $\nu_{xx} = \nu_{yy} = -\nu_{zz}/2$ [12]. Strain, however, breaks the tetragonal symmetry and gives rise to a non-zero asymmetry parameter, $\eta = (\nu_{xx} - \nu_{yy})/\nu_{zz}$. In this case the quadrupolar splitting ν_{yy}, is a strong function of the displacement, as shown in Fig. 3.11. The strong linear variation indicates that the asymmetry parameter is changing with displacement. By comparing ν_{yy} with the value in the unstrained case, we identify $x_0 = 51.53\mu m$ as the displacement in the absence of strain at this temperature, where $\eta = 0$.

Although the epoxy securing the crystal to the device may be expected to deform, the

strong linear variation of the EFG with strain indicates that a large portion of the strain is indeed transferred to the sample. Furthermore, we find that the linewidth of the quadrupolar satellite does not exhibit any significant variation with strain, as shown in the right axis of Fig. 3.11. This result indicates that the strain remains homogeneous over the volume of the crystal within the NMR coil, otherwise we would observe broadening of the resonance with increasing strain. We observe that $d\nu_{yy}/d\epsilon = -259MHz$, whereas the average linewidth is $\delta\nu_{yy} = 125kHz$, implying an upper bound on the strain inhomogeneity of less than $\delta\epsilon \lesssim 4.8 \cdot 10^{-4}$. The strain varies from -0.002 to $+0.003$ over this range, so $\delta\epsilon/\epsilon \lesssim 16\%$ assuming strain inhomogeneity is proportional to the strain magnitude.

Chapter 4

Electronic Nematicity

4.1 Nematic Phase in Classical Liquid Crystals

The term nematic is taken from the context of liquid crystals when there exists long-range orientational order and no long-range positional order. One can observe this by measuring the refractive index of the liquid in different directions. This term is used for solid-state because of the resemblance of the Fermi surface to that of rod-like shaped molecules in the nematic liquid phase (see Fig. 4.1). However, more fundamentally, in condensed matter physics, nematicity means broken rotational symmetry when C_4 symmetry of a tetragonal lattice breaks or C_6 symmetry of a hexagonal lattice is broken.

4.2 Why do we care about nematicity?

Electronic nematic order has been observed in the iron-pnictide superconductors and is associated with the transition from the tetragonal to the orthorhombic structure. In many pnictides, as the doping level is increased, the structural transition gets suppressed and close to the optimal doping level the structural transition coincides with a superconducting transition (see Fig. 4.2). This raises the question of what is the importance of the electronic nematic order associated with the lattice distortion. Do electronic nematic fluctuations play

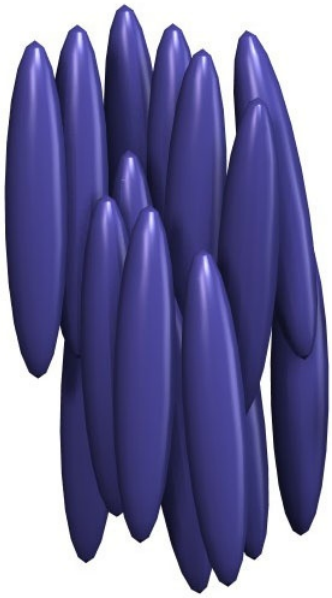

Figure 4.1: The alignment of molecules in a nemtaic liquid phase

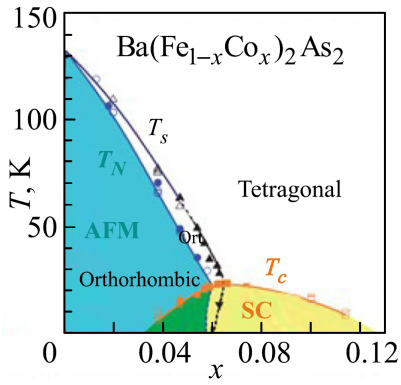

Figure 4.2: Phase diagram of Co-doped $BaFe_2As_2$

an important role in the pairing mechanism for superconductivity [27, 28]? Before addressing that, we have to understand the mechanism behind the electronic nematic phase and how large the nematic fluctuations are which we will be discussed in chapter 5. This problem is complex because there are other competing degrees of freedom - lattice and spin degrees of freedom. Another problem is the formation of structural twin domains that form below the structural transition. This domain structure can make it difficult to interpret bulk measurements like resistivity. Application of uniaxial mechanical strain allows one to fully reversibly detwin these crystals. This is similar to aligning domains in a ferromagnet.

Ferromagnetism	Nematicity
Magnetization, M	Nematic order, η
Magnetic field, H	External stress, σ
Magnetic domains	Structural twin domains

Table 4.1: Similarity between electronic nematicity and ferromagnetism

4.3 Analogy with Ferromagnetism

We know from magnetism the relationship between magnetization and magnetic field:

$$M = \chi H \tag{4.1}$$

where χ is the magnetic susceptibility. A similar relationship governs nematicity and stress:

$$\eta = \chi_{nem}\sigma \tag{4.2}$$

where σ is the uniaxial stress applied to a sample. As can be seen from these two equations stress plays the role of an external magnetic field and χ_{nem} is the nematic susceptibility. In chapter 5, we demonstrate that the nematic susceptibility exhibits Curie-Weiss dependence. Our result confirms earlier results obtained using resistivity measurements.

4.4 Strain and Stress

Strain and stress are the key parameters in studying electronic nematic properties of materials. In general these two quantities are related as:

$$\sigma_{ij} = \sum_{k=1}^{3}\sum_{l=1}^{3} C_{ijkl}\epsilon_{kl} \tag{4.3}$$

where C_{ijkl} is elastic stiffness tensor, σ_{ij} is the stress tensor whose components represent the force per area applied along i to the plane that is normal to j, and ϵ_{kl} is the strain tensor, $i, j, k, l = \{x, y, z\}$. Fig. 4.3 shows an example of shear stress σ_{yz} applied along

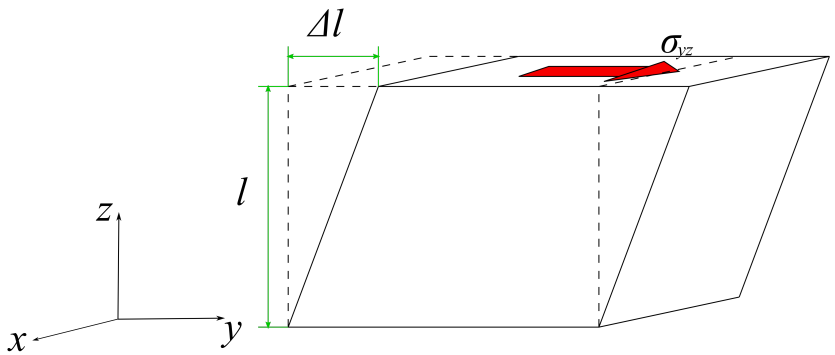

Figure 4.3: Simple illustration of the shear stress defined in the text. Δl is the displacement of top surface, σ is the force applied parallel to the top surface.

y-axis to the plane normal to z-axis. In general C_{ijkl} has 81 components. Due to symmetries associated with stress and strain tensors this number reduces down to 36. The elastic energy density consideration further reduces the number of independent components to 21. Finally, crystal symmetries further reduce the number of independent components. In the case of iron pnictides we have tetragonal symmetry with six independent coefficients. Without going into details, there are C_{11}, C_{33}, C_{44}, C_{12}, C_{13}, and C_{66}[1] (for more detailed discussion see [29]). Because of the plate-like nature of the iron pnictides' growth and the specifics of our CS100 strain device we are interested in C_{66}. Indeed, the strongest nematic response is in C_{66} symmetry channel.

To better understand the pnictides, we consider the case of in-plane stress of a tetragonal lattice. In the coordinate system of the tetragonal unit cell we can apply uniaxial stress in two ways (see Fig. 4.4). Due to the Poisson ratio, application of uniaxial stress induces strains in other directions as well leading to different linear combinations of strain. These linear combinations, in turn, correspond to different symmetry channels A_{1g}, B_{1g} and B_{2g}.

$$\epsilon_{B_{1g}} = \epsilon_{xy}$$

$$\epsilon_{B_{2g}} = \frac{1}{2}\left(\epsilon_{xx} - \epsilon_{yy}\right)$$

[1]Indices are defined as: 1$\equiv xx$, 2$\equiv yy$, 3$\equiv zz$, 4$\equiv yz$, 5$\equiv zx$, 6$\equiv xy$

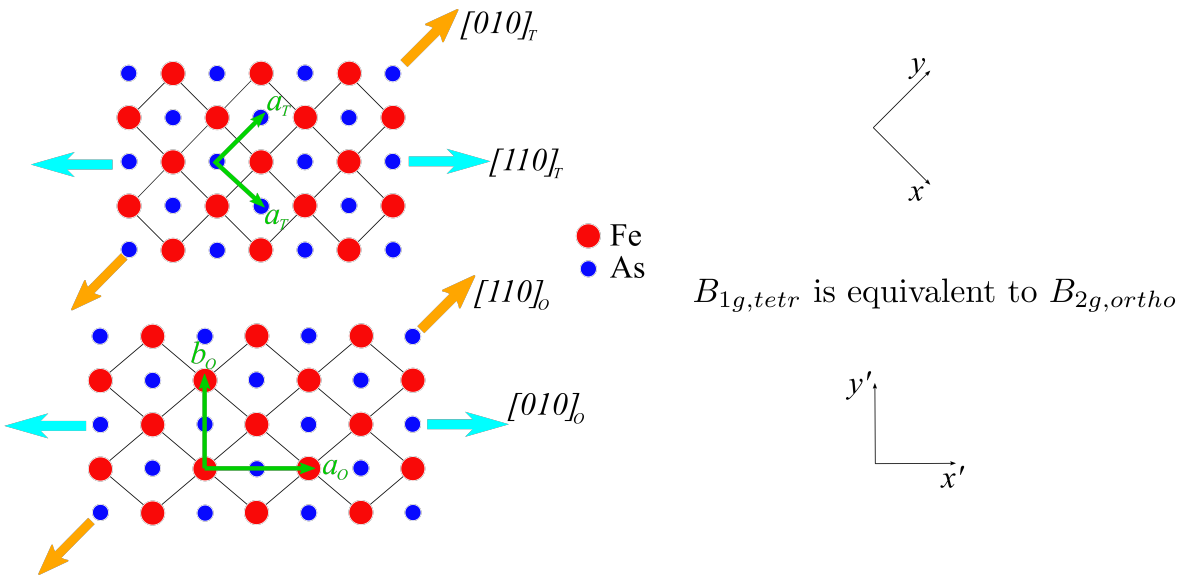

Figure 4.4: Fe-As plane in tetragonal and orthorhombic phase of $BaFe_2As_2$. Orange and cyan arrows represent two ways the uniaxial stress is applied. Green arrows are the unit cell vectors. By convention the strain symmetry channels refer to the 1-Fe unit cell. xy and $x'y'$ are the reference frames of the tetragonal and orthorhombic bases.

$$\epsilon_{A_{1g}} = \frac{1}{2}\left(\epsilon_{xx} + \epsilon_{yy}\right)$$

A_{1g} is equivalent to uniform expansion/compression in the xy plane. In general, we also have to include the strain change along the z-axis but it's ignored because, in the case of iron pnictides, most of the important physics occurs in the $x - y$ plane.

$$\begin{pmatrix} \sigma_{xx} \\ \sigma_{yy} \\ \sigma_{zz} \\ \sigma_{yz} \\ \sigma_{zx} \\ \sigma_{xy} \end{pmatrix} = \begin{pmatrix} C_{11} & C_{12} & C_{13} & 0 & 0 & 0 \\ C_{12} & C_{11} & C_{13} & 0 & 0 & 0 \\ C_{13} & C_{13} & C_{33} & 0 & 0 & 0 \\ 0 & 0 & 0 & C_{44} & 0 & 0 \\ 0 & 0 & 0 & 0 & C_{44} & 0 \\ 0 & 0 & 0 & 0 & 0 & C_{66} \end{pmatrix} \begin{pmatrix} \epsilon_{xx} \\ \epsilon_{yy} \\ \epsilon_{zz} \\ \epsilon_{yz} \\ \epsilon_{zx} \\ \epsilon_{xy} \end{pmatrix} \tag{4.4}$$

where the matrix consisting of C_{ij} is the elastic stiffness tensor. We can also define the elastic compliance tensor, the inverse of the stiffness tensor, which lets us express strain in

terms of stress:

$$\begin{pmatrix} \epsilon_{xx} \\ \epsilon_{yy} \\ \epsilon_{zz} \\ \epsilon_{yz} \\ \epsilon_{zx} \\ \epsilon_{xy} \end{pmatrix} = \begin{pmatrix} \frac{\left(C_{11}C_{33}-C_{13}^2\right)}{A} & -\frac{\left(C_{12}C_{33}-C_{13}^2\right)}{A} & -\frac{C_{13}}{B} & 0 & 0 & 0 \\ -\frac{\left(C_{12}C_{33}-C_{13}^2\right)}{A} & \frac{\left(C_{11}C_{33}-C_{13}^2\right)}{A} & -\frac{C_{13}}{B} & 0 & 0 & 0 \\ -\frac{C_{13}}{B} & -\frac{C_{13}}{B} & \frac{(C_{11}+C_{12})}{B} & 0 & 0 & 0 \\ 0 & 0 & 0 & \frac{1}{C_{44}} & 0 & 0 \\ 0 & 0 & 0 & 0 & \frac{1}{C_{44}} & 0 \\ 0 & 0 & 0 & 0 & 0 & \frac{1}{C_{66}} \end{pmatrix} \begin{pmatrix} \sigma_{xx} \\ \sigma_{yy} \\ \sigma_{zz} \\ \sigma_{yz} \\ \sigma_{zx} \\ \sigma_{xy} \end{pmatrix} \tag{4.5}$$

where $A = C_{11}^2C_{33} - 2C_{11}C_{13}^2 - C_{12}^2C_{33} + 2C_{12}C_{13}^2$, and $B = C_{11}C_{13} + C_{12}C_{33} - 2C_{13}^2$

Solving for ϵ's gives us:

$$\begin{pmatrix} \epsilon_{xx} \\ \epsilon_{yy} \\ \epsilon_{zz} \\ \epsilon_{yz} \\ \epsilon_{zx} \\ \epsilon_{xy} \end{pmatrix} = \begin{pmatrix} \frac{\left(C_{11}C_{33}-C_{13}^2\right)}{A}\sigma_{xx} - \frac{\left(C_{12}C_{33}-C_{13}^2\right)}{A}\sigma_{yy} - \frac{C_{13}}{B}\sigma_{zz} \\ -\frac{\left(C_{12}C_{33}-C_{13}^2\right)}{A}\sigma_{xx} + \frac{\left(C_{11}C_{33}-C_{13}^2\right)}{A}\sigma_{yy} - \frac{C_{13}}{B}\sigma_{zz} \\ -\frac{C_{13}}{B}\sigma_{xx} - \frac{C_{13}}{B}\sigma_{yy} + \frac{(C_{11}+C_{12})}{B}\sigma_{zz} \\ \frac{\sigma_{yz}}{C_{44}} \\ \frac{\sigma_{zx}}{C_{44}} \\ \frac{\sigma_{xy}}{C_{66}} \end{pmatrix} \tag{4.6}$$

If the uniaxial stress (normal stress) is applied along x axis, then $\sigma_{yy} = 0$ and $\sigma_{zz} = 0$ resulting in

$$\begin{pmatrix} \epsilon_{xx} \\ \epsilon_{yy} \\ \epsilon_{zz} \\ \epsilon_{yz} \\ \epsilon_{zx} \\ \epsilon_{xy} \end{pmatrix} = \begin{pmatrix} \frac{\left(C_{11}C_{33}-C_{13}^2\right)\sigma_{xx}}{A} \\ -\frac{\left(C_{12}C_{33}-C_{13}^2\right)\sigma_{xx}}{A} \\ -\frac{C_{13}\sigma_{xx}}{B} \\ 0 \\ 0 \\ 0 \end{pmatrix} \tag{4.7}$$

We can see that the application of the uniaxial stress along the x-axis results in expansion along x and contraction along y, z due to Poisson ratio. We can also write down the Poisson

coefficients:

$$\begin{aligned}\nu_{xy} &= -\frac{\epsilon_{yy}}{\epsilon_{xx}} = \frac{(C_{12}C_{33} - C_{13}^2)}{(C_{11}C_{33} - C_{13}^2)} \\ \nu_{xz} &= -\frac{\epsilon_{zz}}{\epsilon_{xx}} = \frac{C_{13}}{(C_{11}C_{33} - C_{13}^2)}\frac{A}{B}\end{aligned} \tag{4.8}$$

where ν_{xy} and ν_{xz} are the Poisson ratios along y and z when the normal stress is applied along x. If uniaxial stress (which is not shear stress!) is applied along the diagonal, then we have to change the basis, in other words rotate the compliance tensor by 45°. We do that in the following way

$$C_{45^\circ}^{-1} = R^{-1}C^{-1}R$$

The rotation matrix, R, is given by [30]:

$$R = \begin{pmatrix} cos^2\theta & cos^2\theta & 0 & 0 & 0 & 2cos\theta sin\theta \\ cos^2\theta & cos^2\theta & 0 & 0 & 0 & -2cos\theta sin\theta \\ 0 & 0 & 1 & 0 & 0 & 0 \\ 0 & 0 & 0 & cos\theta & sin\theta & 0 \\ 0 & 0 & 0 & -sin\theta & cos\theta & 0 \\ -cos\theta sin\theta & cos\theta sin\theta & 0 & 0 & 0 & cos^2\theta - sin^2\theta \end{pmatrix}$$

where $\theta = 45^\circ$. Therefore, we get the following result for the compliance tensor in the new basis rotated by 45°

$$C_{45^\circ}^{-1} = \begin{pmatrix} \frac{C_{33}}{2B} + \frac{1}{4C_{66}} & \frac{C_{33}}{2B} - \frac{1}{4C_{66}} & -\frac{C_{13}}{B} & 0 & 0 & 0 \\ \frac{C_{33}}{2B} - \frac{1}{4C_{66}} & \frac{C_{33}}{2B} + \frac{1}{4C_{66}} & -\frac{C_{13}}{B} & 0 & 0 & 0 \\ -\frac{C_{13}}{B} & -\frac{C_{13}}{B} & \frac{(C_{11}+C_{12})}{B} & 0 & 0 & 0 \\ 0 & 0 & 0 & \frac{1}{C_{44}} & 0 & 0 \\ 0 & 0 & 0 & 0 & \frac{1}{C_{44}} & 0 \\ 0 & 0 & 0 & 0 & 0 & \frac{2\left(C_{11}C_{33}-C_{13}^2\right)}{A} + \frac{2\left(C_{12}C_{33}-C_{13}^2\right)}{A} \end{pmatrix} \tag{4.9}$$

Now, if we apply the uniaxial stress (normal stress!) which corresponds to B_{2g} in the orthorhombic basis, we get:

$$\begin{aligned}\epsilon_{B_{2g,ortho}} &= \frac{1}{2}\left(\epsilon_{x'x'} - \epsilon_{y'y'}\right) \\ &= \frac{1}{2}\left\{\left(\frac{C_{33}}{2B} + \frac{1}{4C_{66}}\right)\sigma_{x'x'} - \left(\frac{C_{33}}{2B} - \frac{1}{4C_{66}}\right)\sigma_{x'x'}\right\} \\ &= \frac{1}{4C_{66}}\sigma_{x'x'}\end{aligned} \tag{4.10}$$

The $B_{2g,ortho}$ is the symmetry channel that has a large nematic response and the relevant elastic stiffness constant is C_{66}. The nematic susceptibility $\chi_{nem} \propto C_{66}^{-1}$, so when χ_{nem} is large (close to a nematic phase transition), a small stress along x' axis results in a large strain displacement.

4.5 Nematic Order Parameter

We can introduce an order parameter that describes the electronic nematic phase in the case of NMR measurements. There are actually different quantities that can be used as an order parameter. If one measures resistivity then we can write a nematic order parameter in the following way

$$\eta_\rho = \frac{\rho_{xx} - \rho_{yy}}{\rho_{xx} + \rho_{yy}} \tag{4.11}$$

Measuring a quadrupolar splitting allows us to express a nematic order parameter in terms of the EFG tensor:

$$\eta = \frac{\nu_{xx} - \nu_{yy}}{\nu_{xx} + \nu_{yy}} \tag{4.12}$$

Unlike η_ρ, η samples the local order parameter, whereas η_ρ samples the bulk order parameter and depends on the domain structure. Formation of the twin structural domains (see Fig. 4.5) masks intrinsic anisotropy due to the equal population of the structural domains just as domains in a ferromagnet can cancel out the total magnetization. Therefore, NMR is a superior technique to study nematicity in iron pnictides even in the absence of strain. In

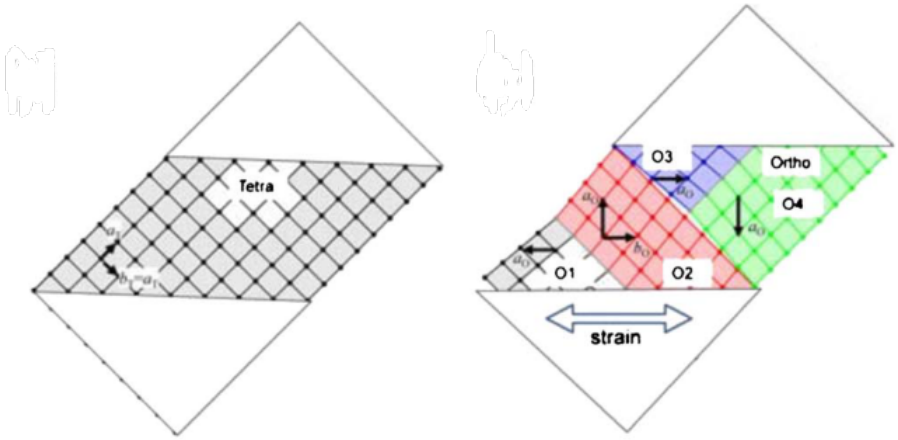

Figure 4.5: Schematics of domain formation during tetra-ortho transition. The orthorhombic phase is realized through displacement of atoms along the diagonal of the tetragonal lattice with the unit-cell volume doubling and the crystallographic axes rotating 45 degrees [3]

.

fact, Takigawa et al. [4] made angular measurements with $\mathbf{H_0}$ and showed that $\eta \neq 0$ despite the fact that the sample was twinned.

4.6 Strain imaging

In our experiments we observed that quadrupole frequencies are linearly proportional to the applied stress. If we have a crystal that has some non-uniform width then strain along the x axis is not uniform. In principle, it should be possible to cut the sample such that the strain varies linearly, $\epsilon(x) = \epsilon(0) + \beta x$, along the strain axis

$$y(x) = \frac{y(0)\,\epsilon(0)}{\epsilon(0) + \beta x} \tag{4.13}$$

where $\beta = \frac{\epsilon(L_0)-\epsilon(0)}{L_0}$. Now, we know that $\nu_{ii}(\epsilon) = \nu_{ii}(0) + \alpha\epsilon$ and $\alpha = \frac{d\nu_{ii}}{d\epsilon}$ then

$$\alpha = \frac{d\nu_{ii}}{d\epsilon} = \frac{d\nu_{ii}}{dx}\frac{dx}{d\epsilon}$$

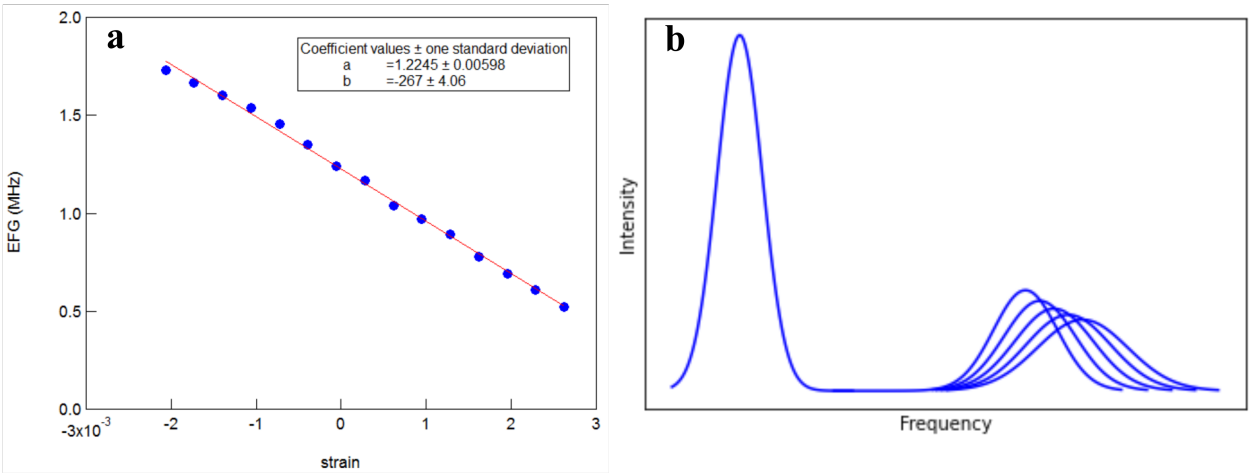

Figure 4.6: a) Quadrupolar frequency vs strain. Each data point was obtained from the full spectra measurements. b) The sketch of NMR spectra for the ^{75}As nucleus. Only the central peak and the right satellite is shown. The central peak is not affected by applied stress whereas the satellite shifts and broadens as more stress is applied

Because strain depends linearly on x we get:

$$\frac{dx}{d\epsilon} = \frac{1}{\beta}$$

This means that quadrupole frequency changes linearly along the strain axis with the slope, γ, equal to $\alpha\beta$. From Fig. 4.6a we can get the value of α which is $-267MHz$. Then γ is:

$$\gamma = |\alpha\beta| \approx 154.86\frac{MHz}{m} \approx 0.16\frac{MHz}{mm}$$

which is our resolution here. NMR spectra should look as shown in Fig. 4.6b. The shape of the intensity is a map of the width shape of a crystal. In this case, the frequency axis corresponds to the spatial axis, in the same manner as in magnetic resonance imaging (MRI). Future experiments might utilize a focused ion beam (FIB) to prepare specialized crystal shapes. Such experiments might enable one to"image" structural defects such as grain boundaries.

Chapter 5

Nematic Susceptibility in $BaFe_2As_2$

5.1 Introduction

Several techniques have been developed to probe the nematic degrees of freedom. Anisotropic resistivity [3] [31], elastoresistance [7], electronic Raman scattering [5], elastic constants [32, 33, 34, 35], thermopower [36], polarized light image color analysis [37, 38], and optical conductivity [39] probe bulk anisotropies. NMR and neutron scattering, on the other hand, have been chiefly used to investigate the effect of nematicity on the spin fluctuations [40, 26, 41, 42, 43]. The nuclear quadrupolar interaction can probe the microscopic orbital occupations directly [44]. The ^{75}As (I = 3/2) quadrupolar moment couples to the local electric field gradient (EFG), which is dominated by the on-site occupations of the As 4p electrons. These orbitals are hybridized with the Fe 3d orbitals, and thus the EFG is a sensitive probe of the d-orbital occupations. Indeed, the EFG tensor exhibits a dramatic lowering from axial symmetry at the nematic phase transition in the absence of applied strain [4]. This chapter presents data on the EFG under uniaxial strain in the paramagnetic phase applied in a controlled manner via a CS100 piezo device. We found that the EFG asymmetry parameter is linearly proportional to the in-plane strain applied to the crystal, and is thus a direct measure of the nematic susceptibility. This approach enables one to probe

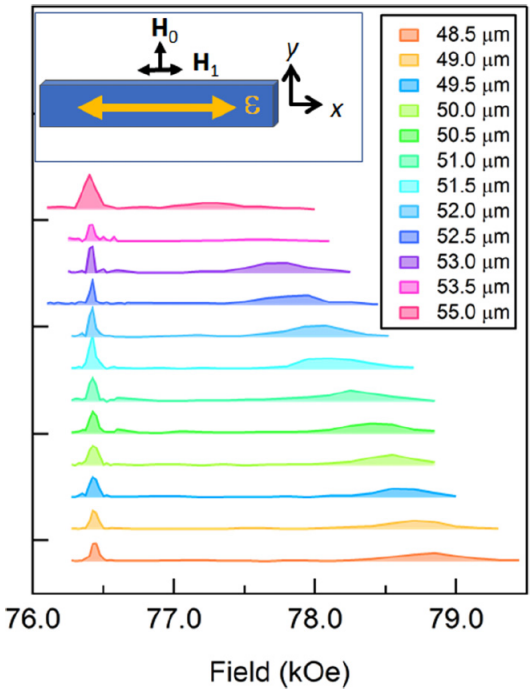

Figure 5.1: Field-swept spectra of BaFe2As2 at constant frequency $f = 55.924MHz$ at $138K$ for several different displacements of the piezoelectric device, showing the central and upper satellite transitions. Zero strain corresponds to $51.58\mu m$. Inset: Orientation of the crystal with respect to the external field $\mathbf{H_0}$, the strain axis, and the rf field $\mathbf{H_1}$. Here, x and y are parallel to the Fe-Fe directions.

the local, rather than global, nematic susceptibility. Moreover, it makes it possible to use NMR to probe the nematic properties of the superconducting state,which is not accessible by elastoresistance measurements.

5.2 Experimental details

A single crystal of $BaFe_2As_2$ was synthesized via a self-flux method and cut to dimensions of approximately 1.5mm×0.5mm with the long axis parallel to the $(110)_T$ direction in the tetragonal basis along the Fe-Fe bond direction. Here, we use x and y to denote these Fe-Fe bond directions. The sample was mounted in a custom-built NMR probe incorporating a Razorbill cryogenic strain apparatus [45]. Uniaxial stress was applied to the crystal as described in Ref. [26] by piezoelectric stacks, as illustrated in the inset of Fig. 5.1, and strain

was measured by a capacitive dilatometer. A free-standing NMR coil was placed around the crystal, and spectra were measured by acquiring echoes while sweeping the magnetic field H_0 at fixed frequency. ^{75}As has spin $I = 3/2$, with three separate resonances separated by the quadrupolar interaction. Figure 5.1 shows the central and upper transitions as a function of strain at fixed temperature. The higher quadrupolar satellite resonance occurs at field [17, 12]:

$$H_{sat} = \frac{f_0 + \nu_{\alpha\alpha}}{\gamma\left(1 + K_{\alpha\alpha}\right)} \tag{5.1}$$

where $f_0 = 55.924MHz$ is the rf frequency, $\gamma = 7.29019MHz/T$ is the gyromagnetic ratio, and $K_{\alpha\alpha}$ and $\nu_{\alpha\alpha}$ are the Knight shift and EFG tensor components in the $\alpha = (x, y, z)$ direction. The central transition field is given by [17, 12]

$$H_{cen} = \frac{f_0}{\gamma\left(1 + K_{\alpha\alpha}\right)}\left(\frac{1}{2} + \sqrt{\frac{3f_0^2 - 2\left(\nu_{\beta\beta} + \nu_{\alpha\alpha}\right)^2}{12}}\right) \tag{5.2}$$

where $\beta = (y, x, z)$ for $\alpha = (x, y, z)$. The spectrum was fit to the sum of three Gaussians to extract both the Knight shift, $K_{\alpha\alpha}$, and the EFG, $\nu_{\alpha\alpha}$ as a function of strain. The Knight shift shows essentially no change with strain [26], however, all components of the EFG tensor show strong variations, as shown in Figs. 5.2 and 5.3.

5.3 The EFG results

The EFG tensor is given by

$$\nu_{\alpha\beta} = \frac{eQ}{12h}\frac{\partial^2 V}{\partial\alpha\partial\beta} \tag{5.3}$$

where $Q = 3.14 \cdot 10^{-29}m^2$ is the quadrupolar moment of the ^{75}As and V is the electrostatic potential at the As site. This quantity is dominated by the occupation of the As $4p$ orbitals, which in turn are hybridized with the $d_{xz,yz}$ orbitals of the neighboring Fe atoms [43]. In

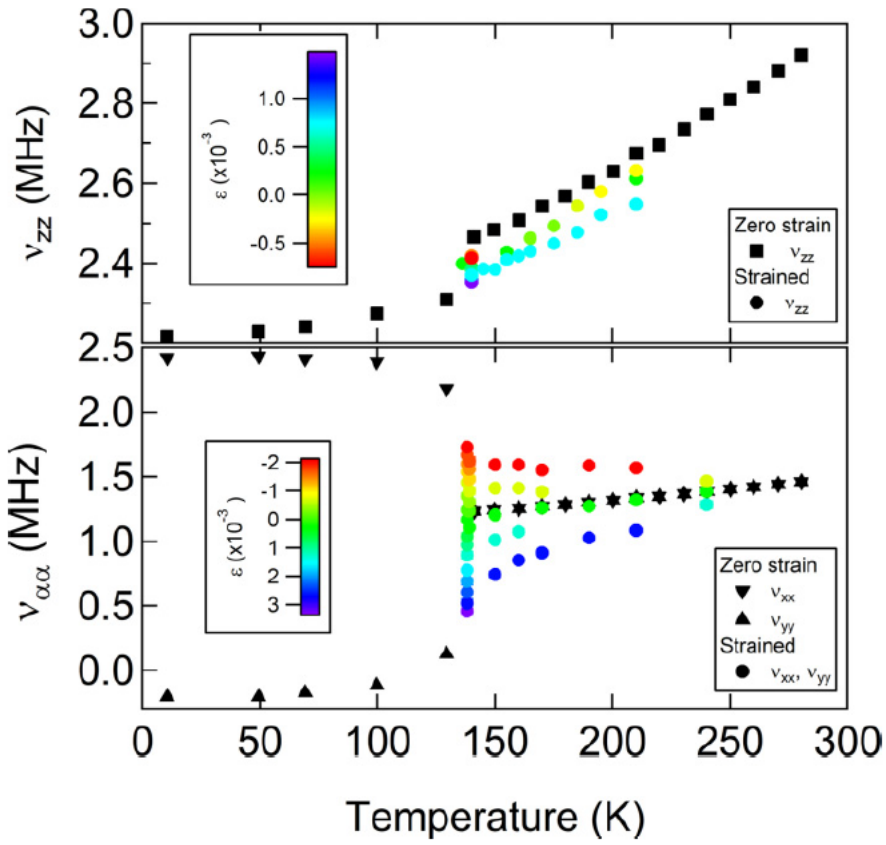

Figure 5.2: The As electric field gradient components (ν_{xx}, ν_{yy}, ν_{zz}) vs temperature for $BaFe_2As_2$ both in zero strain (reproduced from Ref. [4]) and under uniaxial strain.

the tetragonal phase, the EFG asymmetry parameter

$$\eta = \frac{\nu_{yy} - \nu_{xx}}{\nu_{xx} + \nu_{yy}} \tag{5.4}$$

vanishes because the As $4p_x$ and $4p_y$ orbitals are degenerate (i.e., $\nu_{xx} = \nu_{yy}$), as seen in Fig. 5.2. In the presence of nematic order, the C_4 symmetry of the EFG tensor is broken and $\nu_{xx} \neq \nu_{yy}$ [46]. Because the in-plane anisotropic strain field, $\epsilon_{ani} = \epsilon_{B_{2g}}$, with B_{2g} symmetry (in the coordinate system of the tetragonal unit cell) couples bilinearly to the nematic order parameter, η responds to strain in the same manner that the magnetization of a ferromagnet responds to a uniform magnetic field as discussed in Chapter 4 [7, 37, 47]. Although the applied uniaxial stress also induces strains corresponding to other elastic modes, due to the moderate Poisson ratio the dominant mode is ϵ_{B2g}, which couples to η. In our configuration

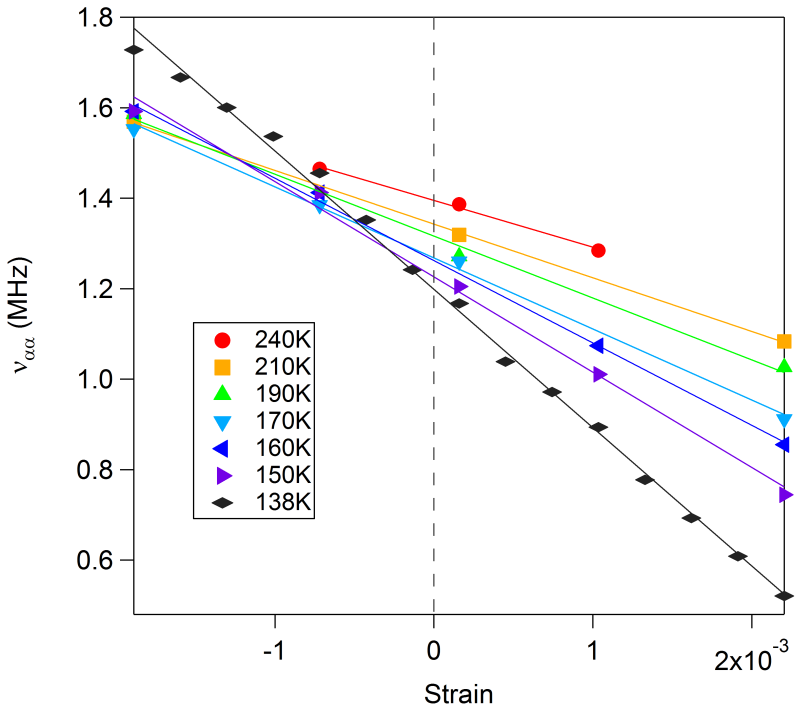

Figure 5.3: The quadrupolar splitting $\nu_{\alpha\alpha} = \nu_{yy}$ as a function of strain at several fixed temperatures. The solid lines are linear fits to the data.

we can only apply $\mathbf{H_0}$ perpendicular to the stress axis, which we denote by x. We measure both $\nu_{zz} = \nu_{cc}$ along the $\hat{c}$ axis of the crystal, and ν_{yy} for $\mathbf{H_0}$ in the basal plane. For the latter case, $\nu_{yy} = \nu_{aa}$ for compressive strain ($\epsilon_{B2g} < 0$) and $\nu_{yy} = \nu_{bb}$ for tensile strain ($\epsilon_{B2g} > 0$), and $\nu_{xx}(\epsilon_{B2g}) = \nu_{yy}(-\epsilon_{B2g})$. The EFG thus enables us to identify the zero-strain displacement x_0 by the condition $|\nu_{xx}| = |\nu_{yy}| = |\nu_{zz}|/2$. Note that η can exceed unity, since $\nu_{xx} + \nu_{yy} + \nu_{zz} = 0$. Furthermore, in the absence of strain, a bulk order parameter in a twinned sample would average to zero, whereas the local order measured by NMR reveals all domains simultaneously [4].

As seen in Fig. 5.2, the applied strain significantly alters the local EFG. Just above the structural transition the strained EFG values approach those in the spontaneously ordered phase in the absence of strain. Furthermore, the maximum strain levels as measured by the dilatometer reach approximately 60% of the spontaneous values of the orthorhombicity in the ordered phase [48].

5.4 Extracting the nematic susceptibility from the EFG

Our results show that ν_{yy} remains linear over this range, as shown in Fig. 5.3. The slope of this response is therefore a measure of the static nematic susceptibility χ_{nem}. Similar behavior was observed in elastoresistance [7], shear modulus [35], and electronic Raman scattering [5]. However, NMR probes the local nematicity in terms of the different orbital occupations reflected in the EFGs, rather than the bulk response, which can be affected by inhomogeneities. We note that, rigorously, χ_{nem} is the "bare" nematic susceptibility, i.e., without the contribution arising from the coupling to the lattice. The bare and renormalized susceptibilities are related by a Legendre transformation.

Figure 5.4 shows the temperature dependence of $d\eta/d\epsilon_{B2g}$ and compares the response to elastoresistance measurements [7]. The NMR data exhibit a similar behavior with a divergence at the structural transition, $T_s = 135$K. We fit the EFG data to the sum of a Curie-Weiss term plus a background susceptibility, $\chi_{nem} = C/(T - T_0) + \chi_0$, and find $C = 4700 \pm 700$ K, $T_0 = 116 \pm 3$ K and $\chi_0 = 54 \pm 8$. The background term reflects the intrinsic response of the lattice, whereas the Curie-Weiss term represents the nematic instability. Our observed value of T_0 is consistent with elastoresistance, but differs from that observed by Raman scattering and by shear modulus measurements [5, 35, 49]. As noted above, the difference between T_0 and T_s arises due to the fact that we are probing the bare nematic susceptibility without the lattice contribution. In order to understand the relationship between the EFG asymmetry and the splitting between the Fe d_{xz} and d_{yz} orbitals, our colleagues W. Goh and W. Pickett performed generalized gradient approximation (GGA)-based density functional theory (DFT) calculations [50, 51] for the tetragonal structure at $300K$ and $0.2GPa$ [52] under anisotropic, in-plane strain ϵ_{ani}. Their values of the EFG are consistent with previous calculations in the absence of strain, but underestimate the experimental values by approximately a factor of 3 [53, 54]. They confirm that the EFG is dominated by the occupation of the As p orbitals [44], which are hybridized with the neighboring d_{xz} and d_{yz} orbitals. They calculate that $d\eta/d\epsilon_{ani} = 33$, which is close to the experimental value

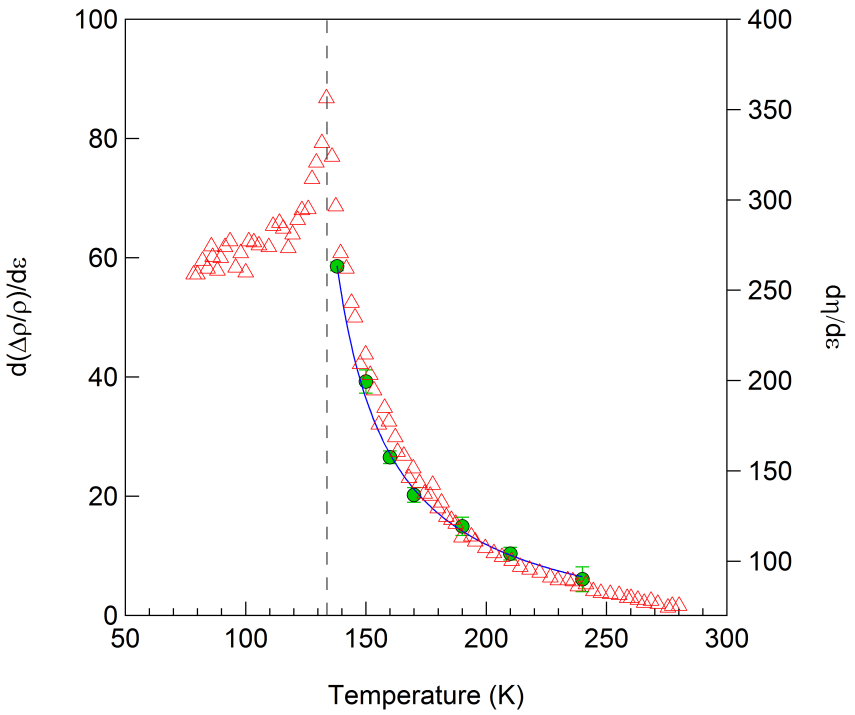

Figure 5.4: The nematic susceptibility measured by the EFG asymmetry (circles) and that measured by elastoresistance (triangles, reproduced from Ref. [3]). The solid line is a fit to the NMR data, as described in the text. The vertical dashed line indicates T_s.

of the background susceptibility, χ_0. The strong temperature-dependent divergence at T_s is a collective phenomenon driven by the electronic system and cannot be captured by the DFT calculations which are valid only at $T = 0$. Under strain, the energy doublet at the M point in $\mathbf{k}$ space corresponding to the degenerate d_{yz} and d_{xz} on-site energies develops a finite splitting, Δ_{xz-yz}. We find that $\eta = A\Delta_{xz-yz}$, where $A = 5.7/eV$. These values are consistent with angle-resolved photoemission experiments that indicate a splitting $\Delta_{xz-yz} \sim 40meV$ in the nematic phase [55], whereas NMR studies reveal a value of $\eta \sim 1.2$ [4].

Figure 5.2 also shows the response of the quadrupolar splitting ν_{zz} along the c axis to in-plane strain. This independent component of the EFG tensor does not couple to the nematic order, but nevertheless it is suppressed by the lattice distortion. Experimentally, we find that ν_{zz} varies quadratically with strain, such that $|\nu_{zz}(\epsilon_{ani})/\nu_{zz}(0)| = 1 - \beta\epsilon_{B2g}^2$, where $\beta \approx 9000$ is approximately temperature independent. The DFT calculations reveal a small quadratic suppression with $\beta = 30$, due to changes in the relative occupations of the

As p_z and $p_{x,y}$ orbitals. The difference between the experimental and theoretical values may reflect changes to the c-axis lattice parameter due to a finite Poisson ratio.

5.5 EFG response in doped pnictides

Our measurements offer insight into the behavior of the EFG in electron-doped pnictides. In doped Ba(Fe,M)$_2$As$_2$ (M=Co, Ni), the quadrupolar satellite resonances are inhomogeneously broadened ($\sim 1.0 - 1.5 MHz$) relative to those in the parent compound ($0.13 MHz$) [56, 57, 58]. A large source of this broadening may arise from local strain distributions. Local strains at dopant atoms can reach up to 3% [59], which would correspond to a shift in the As EFG parameters of $\delta\eta \sim 10$ and $\delta\nu_{zz} \sim 2.9 MHz$ at $140K$. The strain field relaxes with distance from the dopant, and possibly other types of defects, giving rise to a distribution of local EFGs. Recently, a finite EFG asymmetry $\eta \sim 0.1$ was reported in BaFe$_2$(As$_{1-x}$P$_x$)$_2$ in the nominally tetragonal phase [44]. This value would be consistent with an average strain field on the order of 0.05%. We postulate, therefore, that the origin of the finite nematicity observed in this compound reflects inhomogeneous strain fields, rather than intrinsic nematicity above the structural transition [60]. The presence of strain fields in the nominally tetragonal phase has indeed been observed directly by scanning tunneling microscopy (STM) [61]. Complex EFG distributions have also been reported in RFeAsO$_{1-x}$F$_x$ (R=La, Sm) that have been interpreted as nanoscale electronic order [62]. It is unclear whether these spatial variations arise due to ν_{zz} or η, although they may reflect a combination of both strain and/or orbital occupations.

5.6 Conclusion

We have conducted detailed measurements of the EFG under a uniform uniaxial strain, and observed a linear response that is strongly temperature dependent. The slope agrees well with other measurements of the nematic susceptibility, and demonstrates that C_4 symmetry is broken not only in the different Fe $3d$ orbital occupations, but also in the As $4p$ orbitals. Because the As-75 EFG is proportional to the orbital occupations, NMR measurements provide quantitative measures of the changes of these occupations under strain. Measurements of the local nematicity by NMR provide an important microscopic complement to other techniques, and offer a unique opportunity to measure the response in the superconducting state. We plan on conducting NMR under strain below T_c in the future. Such measurements may provide insight into the role of nematic degrees of freedom in the superconducting mechanism [28, 63].

Chapter 6

NMR study of $Ba(Fe_{1-x}Co_x)_2As_2$ x=0.048

6.1 Introduction to Co-doped $BaFe_2As_2$

We performed NMR measurements on a detwinned single crystal of $Ba(Fe_{1-x}Co_x)_2As_2$ with $x = 0.048$ suspended across a mechanical horseshoe clamp briefly discussed in 3.3 with more details provided in the next section. NMR results under uniaxial stress in these materials have not been reported previously. Spin-lattice relaxation rate measurements in twinned samples include contributions from both domains simultaneously, each domain could be strained differently and therefore the magnetization recovery may consist of a distribution of relaxation rates [64]. The material studied here is underdoped, with $T_s \approx 60$ K, $T_N \approx 50$ K, and $T_c \approx 18$ K. We find that the spin-lattice relaxation rate is anisotropic in the basal plane, reflecting strong nematic spin correlations of the Fe spins extending above T_s (As electron spins are correlated as well but the physics is driven by Fe electrons). We also find that the stretched exponential recovery persists in the detwinned crystals [1]. These results suggest that random strain fields induced by the dopants are larger than the externally applied strain used to detwin the crystal.

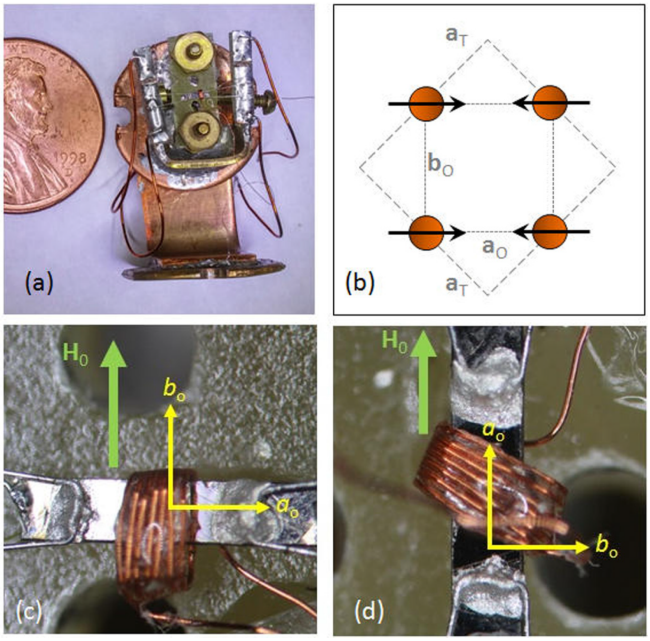

Figure 6.1: (a) Strain device with single crystal of $Ba(Fe_{0.952}Co_{0.048})_2As_2$ under strain. (b) ab plane, showing the Fe atoms and spin orientation in the ordered magnetic phase, with the orthorhombic a_O and b_O axes shown as dotted lines, and the tetragonal axes (a_T) shown as dashed lines. (c) Close-up image of the crystal oriented such that the applied field, $\mathbf{H}_0$, is along the b_O (perpendicular to the direction of applied strain) and (d) along a_O (parallel to the direction of applied strain). For the latter case, the coil was rotated by approximately 30° so that a component of the radio-frequency field $\mathbf{H}_1$ lies perpendicular to $\mathbf{H}_0$.

6.2 Application of strain and detwinning

Single crystals were synthesized by the Canfield group via a self-flux method and characterized via transport measurements and wavelength-dispersive spectroscopy to determine the Co-doping level [65]. A sample of dimensions $1.1mm \times 0.57mm \times 0.05mm$ was cut with the long axis parallel to the tetragonal [110] direction, and mounted in a mechanical horseshoe device as described in Ref. [3] and shown in Fig. 6.1. The crystal was secured using silver wires soldered to the edges of the sample. These wires serve not only to transmit tensile stress to the crystal but also as leads for resistivity measurements. Stress is applied by tightening a screw by about 1/4 to 1/2 turn, which is enough to apply stresses on the order of 10–$20MPa$ [3]. The sample was inserted into the NMR coil embedded in epoxy prior to mounting in the clamp cell. This is the first time such a device has been employed for NMR

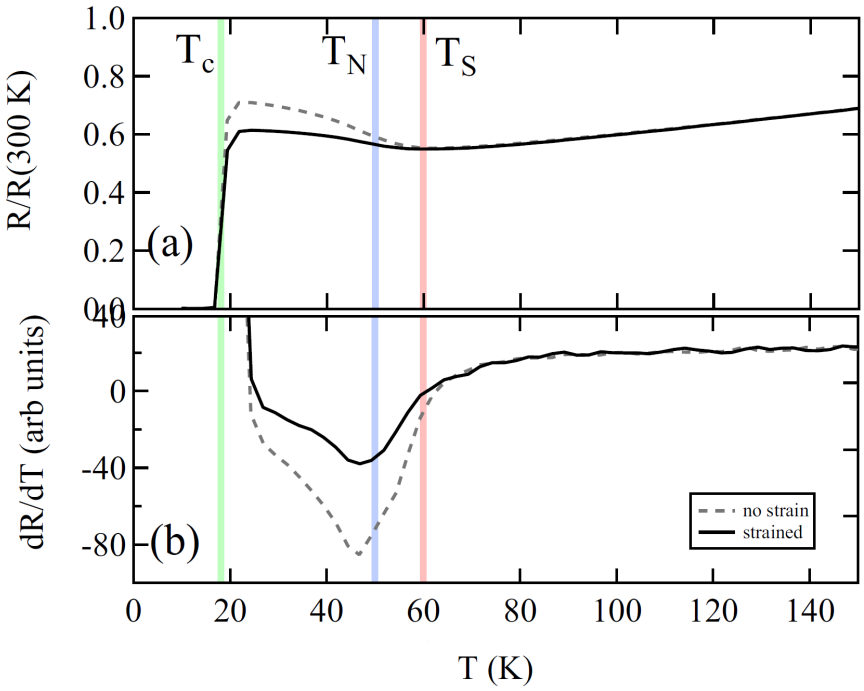

Figure 6.2: (a) Resistance and (b) derivative of resistance versus temperature for the $Ba(Fe_{0.952}Co_{0.048})_2As_2$ crystal measured with and without strain in zero field. Resistivity reaches a minimum at T_S, and the dR/dT curve exhibits a minimum at T_N. T_N transition shown in the graph is extracted from $1/(T_1T)$ measurements and is slightly different from the T_N temperature defined by the minimum in dR/dT.

measurements.

The resistance of the crystal is shown in Fig. 6.2 as a function of temperature measured in zero magnetic field. In the unstrained state, the resistivity exhibits a minimum at T_s, and the temperature derivative dR/dT curve exhibits a broad maximum close to T_N [10, 65]. Note, however, that we identify T_N not by the resistance measurements, but by the peak in T_1^{-1}, as discussed below, since that indicates a divergence in the critical spin fluctuations. In the absence of strain, the resistance includes domains oriented both along the crystallographic a_O and b_O directions. Under strain, domains oriented with the a_O axis parallel to the direction of applied tensile strain are favored, and the measured resistance changes below T_s. For sufficiently large strain, the measured resistance becomes independent of strain, indicating a fully detwinned state. Figure 6.2 shows the resistance for the fully detwinned state. This behavior is consistent with independent measurements of the resistivity along

the a_O direction [31].

6.3 Spin-Lattice Relaxation Data

The spin-lattice relaxation rate, T_1^{-1} , was measured at the central transition of the ^{75}As ($I = 3/2$) by inversion recovery [1] in a field of $H_0 = 11.73T$ for the field perpendicular to the c axis, with and without strain applied. The measurements were conducted with $\mathbf{H_0}$ oriented both parallel ($\mathbf{H_0}||a_O$) and perpendicular ($\mathbf{H_0}||b_O$) to the direction of applied strain. The nuclear magnetization was fit to a stretched exponential B.1

$$M(t) = M_0\{1 - f[\frac{9}{10}e^{-(\frac{6t}{T_1})^\beta} + \frac{1}{10}e^{-(\frac{t}{T_1})^\beta}]\} \tag{6.1}$$

where M_0 is the equilibrium magnetization, f is the inversion fraction, and β is the stretching exponent [64]. $(T_1T)^{-1}$ and β are shown as a function of temperature in Fig. 6.3 (note that the data have been offset vertically for clarity). For $\mathbf{H_0}||b_O$, the coil was naturally oriented such that the rf field $\mathbf{H_1} \perp \mathbf{H_0}$, as shown in Fig. 6.1(c); this condition is necessary in order to detect the nuclear magnetization and obtain a high signal-to-noise ratio. For $\mathbf{H_0}||a_O$ the coil was rotated by $\sim 30°$ from the strain axis as shown in Fig. 6.1(d) in order to create a component of $\mathbf{H_1}$ that is perpendicular to $\mathbf{H_0}$. The component parallel to $\mathbf{H_0}$ has no effect on the nuclear magnetization and does not affect the T_1^{-1} measurement. The clamp and suspended crystal were warmed to room temperature and rotated between Figs. 6.1(c) and 6.1(d). Because the applied stress was not changed, the level of strain was nominally identical for the two orientations.

As seen in Fig. 6.3, the relaxation rate diverges at T_N, and the stretching exponent, β, reaches a minimum of ≈ 0.5 at this temperature. The same qualitative behavior is observed

[1] Inversion recovery is a pulse techinque to measure T_1^{-1} using spin echos. First, a π pulse is applied that inverts the nuclear magnetization. Then, the system is allowed to relax for different times called t_{wait}. Finally, the spin echo pulse sequence is applied to sample the nuclear magnetization [1]

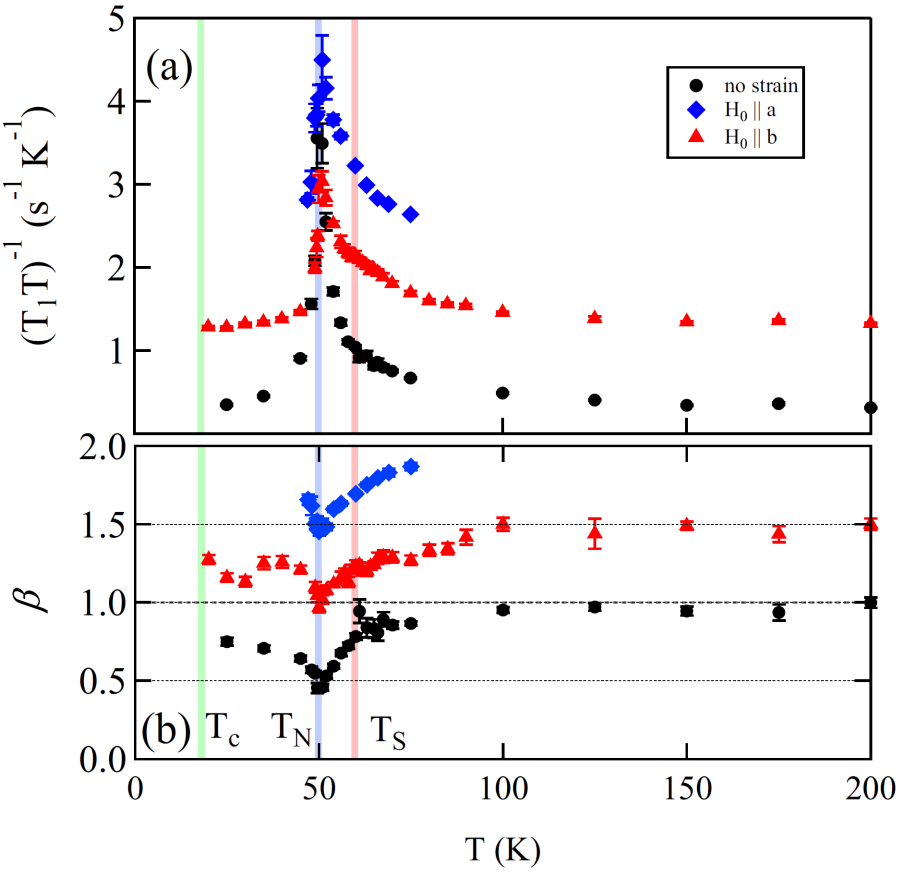

Figure 6.3: (a) $(T_1T)^{-1}$ and (b) the stretching exponent β vs temperature for $Ba(Fe_{0.952}Co_{0.048})_2As_2$ for field oriented along either the a_O or b_O directions. The data in panel (a) have been offset vertically by 1 and 2 $s^{-1}K^{-1}$ for clarity and in panel (b) by 0.5 and 1.0.

with and without strain, but there are subtle differences in $(T_1T)^{-1}$ that emerge near T_s under strain. The peak value of $(T_1T)^{-1}$ decreases by $\sim$ 30% for both directions under strain. Furthermore, the data for $\mathbf{H_0}||b_O$ appear to exhibit a small shoulder at T_s that does not appear in the data for the a_O direction. Surprisingly β does not show any significant differences under strain. β is a direct measure of the width of the distribution of local relaxation rates [21]. This distribution has been postulated to arise from random strain fields induced by the dopants that couple to nematic order, causing β to decrease from unity below a temperature on the order of $100K$ in this doping range [46]. This inhomogeneity might be expected to vanish in the presence of a homogeneous strain field that is enough to induce a single nematic domain. However, the data indicate that the level of inhomogeneity, as

measured by the size of β, remains unchanged. This result suggests that either the origin of the inhomogeneous relaxation arises from some other source of disorder or that the random strain fields induced by the Co dopant atoms [59], which are much larger than the modest homogenous strain field that is applied to detwin the crystal, are responsible for the glassy behavior.

Figure 6.4(a) shows the difference $\Delta(T_1T)^{-1}_{\alpha} = (T_1T)^{-1}_{\alpha}(\epsilon) - (T_1T)^{-1}_{\alpha}(0)$ $(\alpha = a, b)$ between the relaxation rates with and without uniaxial tensile strain for both directions. Figure 6.4(b) shows the anisotropy in the relaxation rate, $(T_1T)^{-1}_{anis} = (T_1T)^{-1}_{a} - (T_1T)^{-1}_{b}$ under strain, and the isotropic strain-induced component, $(T_1T)^{-1}_{iso} = \frac{1}{2}[(T_1T)^{-1}_{a}(\epsilon) + (T_1T)^{-1}_{b}(\epsilon)] - (T_1T)^{-1}(0)$. The relaxation was measured for both crystal directions in the absence of strain, and no differences were observed to within the error bars. All of these quantities peak at T_N, but remain finite up to and above T_s. This behavior reflects the fact that C_4 symmetry is broken by the strain field, which induces a finite nematicity above the onset of long-range nematic order, similarly to how a magnetic field induces a finite magnetization in the paramagnetic phase above the Curie temperature in a ferromagnet. Similar behavior has been observed in elastoresistance and neutron scattering measurements [7, 43, 42]. Note that the in magnitude of $(T_1T)^{-1}_{anis}$ (green data in Fig. 6.4) in the detwinned state is approximately 30% of the value of $(T_1T)^{-1}$ (black data in Fig 6.3) in the unstrained state at T_N. The width of the distribution of relaxation rates, however, far exceeds this variation due to the anisotropy, which is consistent with the observation that β is unchanged in the detwinned state.

6.4 Analysis

To analyze the results, we start with the general expression for the spin-lattice relaxation rate due to a magnetic field applied in an arbitrary direction. Hereafter, our coordinate system refers to the 1-Fe unit cell in the orthorhombic phase. In the paramagnetic state, the

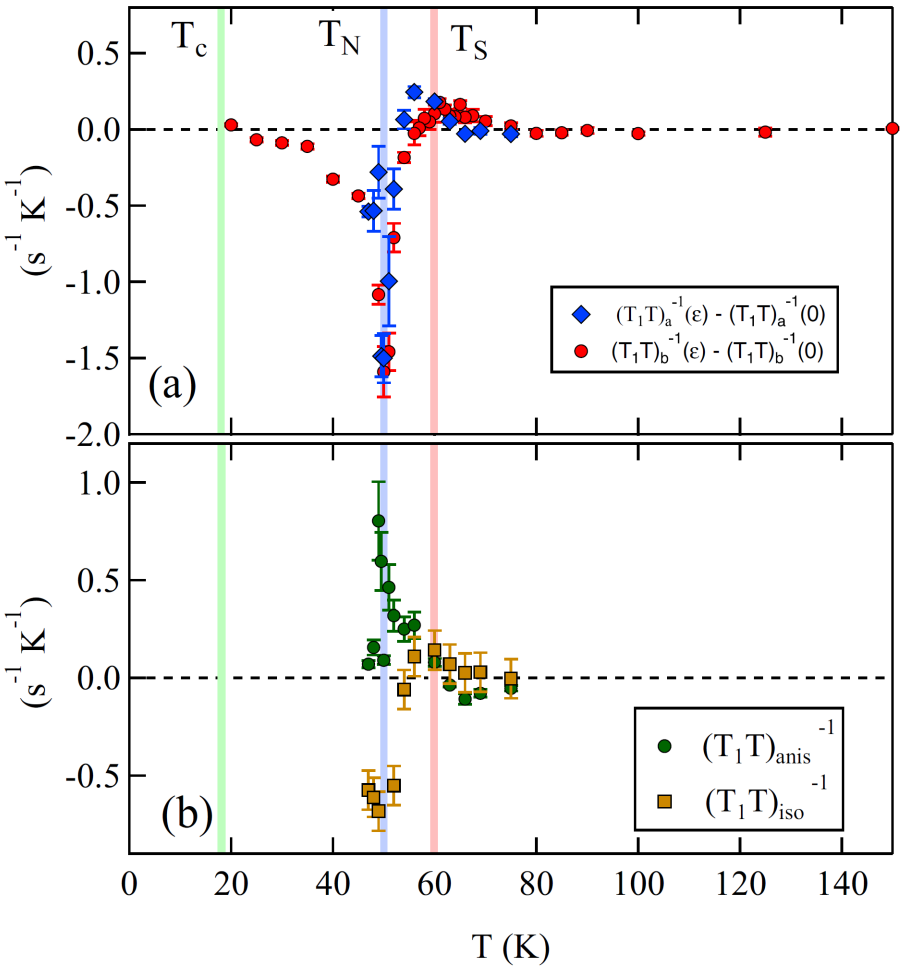

Figure 6.4: (a) $(T_1T)^{-1}(\epsilon)-(T_1T)^{-1}(0)$ for field along both the a and b directions, and (b) $(T_1T)^{-1}_{anis}$ and $(T_1T)^{-1}_{iso}$ vs temperature for $Ba(Fe_{0.952}Co_{0.048})_2As_2$.

internal field experienced by the nucleus is zero and we obtain [18]

$$\left(\frac{1}{T_1T}\right)_{\theta,\phi} = \frac{\gamma^2}{2}\sum_{\mathbf{q}}\sum_{\alpha=x,y}\left[\bar{R}\cdot\bar{A}_{\mathbf{q}}\cdot\bar{\tilde{\chi}}(\mathbf{q})\cdot\bar{A}^{\dagger}_{\mathbf{q}}\cdot\bar{R}^{\dagger}\right]_{\alpha\alpha} \tag{6.2}$$

where γ is a constant proportional to the gyromagnetic ratio of the nucleus, $\bar{A}_{\mathbf{q}}$ is the hyperfine tensor, $\bar{R}$ is the rotation matrix (shown explicitly in the A.2, and θ, ϕ are the polar and azimuthal angles describing the direction of the magnetic field with respect to the (a, b, c) crystal axis. In this coordinate system, the susceptibility is diagonal in spin space, $\bar{\chi} = diag\,(\chi_{aa}, \chi_{bb}, \chi_{cc})$. For convenience, we defined $\bar{\chi}_{\alpha\beta}(\mathbf{q}) = \lim_{\omega\to 0}\frac{\Im\chi_{\alpha\beta}(\mathbf{q},\omega)}{\omega}$. Because the sys-

tem is metallic, Landau damping[2] Γ is present and we can write $\chi^{-1}_{\alpha\beta}(\mathbf{q},\omega) = \chi^{-1}_{\alpha\beta}(\mathbf{q},\omega) - i\Gamma\omega$, yielding $\tilde{\chi}_{\alpha\beta}(\mathbf{q}) = \Gamma\chi^2_{\alpha\beta}(\mathbf{q})$.

The anisotropy in the spin-lattice relaxation rate $\left(\frac{1}{T_1T}\right)_{anis} \equiv \left(\frac{1}{T_1T}\right)_a - \left(\frac{1}{T_1T}\right)_b \equiv \left(\frac{1}{T_1T}\right)_{\phi=0,\theta=\pi/2} - \left(\frac{1}{T_1T}\right)_{\phi=\pi/2,\theta=\pi/2}$ can be calculated directly from Eq. (6.2). In general, the anisotropy in $1/T_1T$ can arise from two sources: either an anisotropy in the elements of the hyperfine tensor $\bar{A}_{\mathbf{q}}$ or an anisotropy in the elements of the susceptibility tensor $\chi_{\alpha\beta}$. The latter reflects the anisotropies of the magnetic fluctuations, whereas the former is mainly determined by the changes in the lattice environment. Since the lattice distortions are very small, hereafter we focus on the anisotropies induced by the spin spectrum only, setting $A_{aa} = A_{bb}$, $A_{bc} = A_{ac}$, and $A_{ab} = A_{ba}$. We obtain

$$\left(\frac{1}{T_1T}\right)_{anis} = \frac{g^2}{2}\sum_{\mathbf{q}}\left\{\left[F_1(\mathbf{q})A^2_{ab} - F_2(\mathbf{q})A^2_{aa}\right]\left[\tilde{\chi}_{aa}(\mathbf{q}) - \tilde{\chi}_{bb}(\mathbf{q})\right] + F_3(\mathbf{q})A^2_{cc}\tilde{\chi}_{cc}(\mathbf{q})\right\} \quad (6.3)$$

with the form factors $F_1(\mathbf{q}) = sin^2\left(\frac{q_x}{2}\right)sin^2\left(\frac{q_y}{2}\right)$, $F_2(\mathbf{q}) = cos^2\left(\frac{q_x}{2}\right)cos^2\left(\frac{q_y}{2}\right)$, and $F_3(\mathbf{q}) = \frac{1}{2}(cosq_x - cosq_y)$. The existence of a sizable spin-orbit coupling in the iron pnictides [67] enforces important symmetry constraints on the susceptibility tensor [68, 69]. Specifically, in the tetragonal paramagnetic phase, while $\chi_{aa}(\mathbf{q})$ and $\chi_{bb}(\mathbf{q})$ do not need to be C_4 (tetragonal) symmetric functions, $\chi_{aa}(\mathbf{q})$ becomes identical to $\chi_{bb}(\mathbf{q})$ upon a 90° rotation. Therefore, because the combination $\chi_{aa}(\mathbf{q}) - \chi_{bb}(\mathbf{q})$ is C_2 symmetric, while the functions $F_1(\mathbf{q})$ and $F_2(\mathbf{q})$ are C_4 symmetric, the first term in Eq. (6.3) vanishes in the tetragonal phase. Similarly, symmetry requires that $\chi_{cc}(\mathbf{q})$ is a C_4 symmetric function; thus, because $F_3(\mathbf{q})$ is C_2 symmetric, the second term vanishes as well. Hence, as expected, $(T_1T)^{-1}_{anis}$ vanishes in the tetragonal phase.

To model the magnetic spectrum of the pnictides, we note that at low energies the susceptibility is strongly peaked at the magnetic ordering vectors $\mathbf{Q_1} = (\pi, 0)$ and $\mathbf{Q_2} = (0, \pi)$,

[2]For a purely magnetic system, the spin wave excitations are slow, but if the system is metallic and there is a coupling between the magnetism and the electrons, the fast electrons will damp the magnetic excitations through a process known as Landau damping [66]

as seen by neutron scattering [70, 71]. If the susceptibilities were δ functions peaked at the ordering vectors, then the fact that $F_1(\mathbf{Q}_i) = F_2(\mathbf{Q}_i) = 0 \neq F_3(\mathbf{Q}_i)$ would imply that $(T_1T)^{-1}_{anis}$ probes only the χ_{cc} component of the susceptibility tensor. However, the system has a finite magnetic correlation length in the paramagnetic phase. To model this behavior,we consider a low-energy model in which the susceptibilities are peaked at the magnetic ordering vectors [72]:

$$\begin{aligned}
\frac{\chi_{aa}(\mathbf{q})}{\chi_0} &= \left(\xi_1^{-2} + cosq_x - cosq_y + 2\right)^{-1} \\
&\quad + \left(\xi_2^{-2} - cosq_x + cosq_y + 2\right)^{-1}, \\
\frac{\chi_{bb}(\mathbf{q})}{\chi_0} &= \left(\xi_2^{-2} + cosq_x - cosq_y + 2\right)^{-1} \\
&\quad + \left(\xi_1^{-2} - cosq_x + cosq_y + 2\right)^{-1}, \\
\frac{\chi_{cc}(\mathbf{q})}{\chi_0} &= \left(\xi_3^{-2} + cosq_x - cosq_y + 2\right)^{-1} \\
&\quad + \left(\xi_3^{-2} - cosq_x + cosq_y + 2\right)^{-1}.
\end{aligned} \tag{6.4}$$

where we defined the correlation lengths ξ_i associated with each magnetic channel (in units of the lattice constant a) and the magnetic energy scale χ_0^{-1}. In the tetragonal phase, symmetry requires that $\chi_{aa}(\mathbf{Q_1}) = \chi_{bb}(\mathbf{Q_2})$, $\chi_{bb}(\mathbf{Q_1}) = \chi_{aa}(\mathbf{Q_2})$, and $\chi_{cc}(\mathbf{Q_1}) = \chi_{cc}(\mathbf{Q_2})$ [69], which is satisfied by Eq. (6.4). The situation is different in the nematic phase, where magnetic fluctuations become anisotropic; i.e., fluctuations around $\mathbf{Q_1}$ and $\mathbf{Q_2}$ are no longer equivalent. Because the susceptibility tensor has three independent elements, one needs to introduce three so-called nematic order parameters ϕ_i, with $i = 1, 2, 3$. We introduce them in Eq. (6.4) by replacing the magnetic correlation lengths $\xi_1^{-2} \to \xi_1^{-2} \mp \phi_1$, $\xi_2^{-2} \to \xi_2^{-2} \pm \phi_2$, (where the upper sign refers to χ_{aa} whereas the lower sign refers to χ_{bb}), and $\xi_3^{-2} \to \xi_3^{-2} \mp \phi_3$ (where the upper sign corresponds to the first term in χ_{cc} whereas the lower sign refers to the second term). The physical meaning of these nematic order parameters is clear [11], as $\phi_i > 0$ ($\phi_i < 0$) implies that the $\mathbf{Q_1}$ ($\mathbf{Q_2}$) ordering vector is selected in the nematic phase. ϕ_1, ϕ_2, and ϕ_3 only become non-zero when the system breaks C_4 symmetry. They are all

proportional to one another, so they are either all non-zero when C_4 symmetry is preserved, or all non-zero when C_4 symmetry is broken. Note that the proportionality constants and their relative signs depend on microscopic considerations and are not known.

Substituting these expressions in Eq. (6.3) and expanding to leading order in the three nematic order parameters, we obtain (in units of $\frac{g^2\gamma\chi_0}{\pi}$)

$$(T_1T)^{-1}_{anis} = -2\left(A^2_{aa} - A^2_{bb}\right)\left(\phi_1\xi_1^2 - \phi_2\xi_2^2\right) - 8A^2_{ac}\phi_3\xi_3^4 \tag{6.5}$$

and

$$\Delta\,(T_1T)^{-1}_{iso} = 8A^2_{ac}\xi_1^6\phi_1^2 + \frac{1}{2}\left(A^2_{aa} + A^2_{ab}\right)\xi_2^4\phi_2^2 + 4A^2_{ac}\xi_3^6\phi_3^2 \tag{6.6}$$

In deriving these expressions, we considered ξ_i to be moderately large and kept the leading order terms for each ξ_i. We also neglected any strain-induced changes to the tetragonal hyperfine coupling tensor. As expected from symmetry consideration, $(T_1T)^{-1}_{anis}$ varies linearly with ϕ_i, whereas $(T_1T)^{-1}_{iso}$ varies quadratically. According to previous NMR investigations, $A_{aa} \approx 0.66 kOe/\mu B$ and $A_{ac} \approx 0.43 kOe/\mu B$ [4]. We do not have direct information about A_{ab}; however, all of the other elements of the hyperfine tensor are known. If we assume that one of the principal axes of the tensor lies along the Fe-As bond axis, then we can constrain $A_{ab}/A_{aa} = 0.37$ or -0.94; thus it is reasonable to assume $A_{ab} < A_{aa}$.

We are now in a position to analyze the experimental results displayed in Fig. 6.4. The presence of tensile strain ϵ along the a axis effectively induces a conjugate field that couples to the nematic order parameters, i.e., $\phi_i \propto \epsilon$. As a result, the nematic phase extends to high temperatures, and T_S signals a crossover rather than an actual phase transition. Furthermore, because in our experiment tensile strain is applied along the a axis, the $\mathbf{Q_1}$ ordering vector is selected by the external strain, with spins pointing along the a axis (see Fig. 6.1 and also Ref. [43]). As a result, $\phi_1 > 0$, although ϕ_2 and ϕ_3 could in principle have different signs.

At temperatures much larger than the magnetic transition temperature T_N, the effects

of the spin-orbit coupling are presumably small. Therefore, in this regime, the magnetic spectrum should display an isotropic behavior, with $\xi_i \approx \xi$. In this regime the last term in Eq. (6.5) dominates, and the sign of $(T_1T)^{-1}_{anis}$ is the opposite of the sign of ϕ_3. According to the data plotted in Fig. 6.4(b), within the experimental error bars, $(T_1T)^{-1}_{anis} < 0$ at high temperatures, suggesting that $\phi_3 > 0$.

As the magnetic transition is approached, the effects of the spin-orbit coupling presumably become more important. In particular, because in the magnetically ordered state the magnetic moments point parallel to the ordering vector $\mathbf{Q}_i$, ξ_1 must be the only correlation length that diverges at the magnetic transition, i.e., $\xi_1 \gg \xi_2, \xi_3$ at $T \gtrsim T_N$. Consequently, the first term in Eq. (6.5) should dominate in this regime. Because $\phi_1 > 0$ and $A_{ab} < A_{aa}$, we expect that $(T_1T)^{-1}_{anis} < 0$ near the transition. This expectation, however, does not agree with the observed behavior seen in Fig. 6.4(b).

We can also analyze the isotropic response, $(T_1T)^{-1}_{iso}$. According to Eq. (6.6), $\Delta\,(T_1T)^{-1}_{iso}$ is always positive. Indeed, neutron scattering experiments in both twinned [73] and detwinned [74] samples find enhanced magnetic fluctuations in the nematic phase. However, our data presented in Fig. 6.4(b) shows that $\Delta\,(T_1T)^{-1}_{iso}$ is positive only at high temperatures — roughly within the same regime in which $(T_1T)^{-1}_{anis} < 0$ ¡ 0 — and becomes negative as T_N is approached, in contrast with the prediction of Eq. (6.6).

There are several possible reasons for this discrepancy between the theoretical calculation and the observed data in the temperature regime near T_N, including (i) unequal strain between the two different field orientations, (ii) crystal misalignments, and (iii) higher order corrections due to noninfinitesimal strain. Note that this device nominally applies a constant stress, rather than constant strain, and differential thermal contraction between the mechanical clamp, the silver wires, and the sample likely leads to a temperature-dependent induced strain. Because the nematic order parameters ϕ_i should be proportional to the strain, these quantities may not be the same for the two different field directions in the measured values. For example, if the wires used to suspend the sample exhibit a temperature-hysteretic effect

due to thermal contractions that exceed the elastic regime, then the strain applied for the two different directions will be different.

Scenario (ii), crystal misalignment, could arise from a small component of $\mathbf{H}_0$ along the c direction that is different between different crystal orientations, which would contribute an asymmetry that would not cancel out. As the crystal is suspended in free space by the wires, it is possible that differences in thermal expansions could lead to torques that could twist the crystal, giving rise to a difference between the crystal orientation between strained and unstrained conditions. It's also possible that the equilibrium positions of the crystal were slightly different with respect to the magnetic field for the two orientations. Detailed studies of the NMR spectra (not shown) in the ordered state of undoped $BaFe_2As_2$ under strain in this device indicate that misalignments of $1-2^\circ$ are possible.

The third scenario, namely higher-order strain-induced changes to the spin-lattice relaxation rate, could be present, depending on the sensitivity of the nematic order parameters, ϕ_i, to strain. Nominally, the applied strains are small and are just enough to detwin the crystal. We observe little or no shift in the peak of $(T_1T)^{-1}_\alpha$ at T_N in Fig. 6.3, suggesting that the main effect of strain is to detwin the crystal. However, for sufficiently high strain levels, T_N is known to increase [74], and therefore the temperature dependence of the correlation lengths ξ_i will be altered.

In this regard, we note that the theoretical analysis presented here considers the linear response of $(T_1T)^{-1}_{anis}$ to strain. From generic symmetry considerations, in the linear-response regime, one expects that $\Delta\,(T_1T)^{-1}_a$ and $\Delta\,(T_1T)^{-1}_b$ display opposite behaviors. From Fig. 6.4, this does seem to be the case at higher temperatures, where in fact the theoretical predictions for $(T_1T)^{-1}_{anis}$ and $(T_1T)^{-1}_{iso}$ are in qualitative agreement with the data. As T_N is approached, however, both $\Delta\,(T_1T)^{-1}_a$ and $\Delta\,(T_1T)^{-1}_b$ display the same behavior, indicating the onset of nonlinear effects beyond the analysis presented here. To mitigate these issues, it would be interesting to control precisely the applied strain using a piezo device, as was done in Ref. [7] for resistivity measurements.

An alternative explanation for the inhomogeneity of the relaxation rates attributes it to the incommensurability of the magnetic ordering vector [75, 76, 77]. However, for the concentration studied here, high-resolution resonance magnetic x-ray diffraction reported no signs of incommensurability [78]. Neutron scattering studies have reported incommensurate order only at higher doping levels ($x > 0.056$) [79].

6.5 Conclusion

In summary, we have measured the NMR spin-lattice relaxation rate in $Ba(Fe_{1-x}Co_x)_2As_2$ with $x = 0.048$ under uniaxial tensile stress as a function of temperature and found significant changes to the relaxation rate that persist above T_s in a detwinned crystal. The strain field breaks C_4 symmetry, and the anisotropic magnetic fluctuations probed by T_1^{-1} reflect the impact of nematicity on the fluctuation spectrum. Surprisingly, the glassy behavior manifested by the broad distribution of relaxation times is unaffected under strain. This observation suggests that the local strains, introduced either by the Co dopants or by lattice defects, exceed the applied strain. Consequently the glassy behavior is not associated with large nematic domains.

We also compute the spin-lattice relaxation rate using a model for the anisotropic dynamical spin susceptibility. By introducing nematic order parameters that reflect the changes to the spin-spin correlation lengths along the three crystal axes, we estimate the leading contributions to the anisotropy of the spin-lattice relaxation rate in the presence of strain. Theoretically, we find that the strain-induced changes to $\left(T_1 T_{a,b}^{-1}\right)$ should have opposite signs. On the other hand, experimentally we find that this is the case only at high temperatures, since both quantities are suppressed as T_N is approached. This discrepancy most likely arises due to crystal misalignments between the strained and unstrained states, and/or differences in induced strains between the two different directions. Future measurements with more precise control over the orientation and amplitude of the strain will provide detailed information

about the relative sizes of the nematic order parameters, ϕ_i, under strain. Nevertheless, our experiments show that the combination of NMR and strain is a unique tool to probe the effect of nematic order not only on the unpolarized magnetic spectrum but most importantly on the polarized spin spectrum, revealing the interplay between nematicity and spin-orbit coupling.

Chapter 7

Spin Polarization under uniaxial strain in $BaFe_2As_2$

7.1 Introduction

The close relationship between nematicity and the magnetic degrees of freedom can be seen directly from the stripe-like nature of the antiferromagnetic state, which orders with one of two possible wave-vectors related by a 90° rotation: $\mathbf{Q}_1 = (\pi, 0)$ (corresponding to spins parallel along the y-axis and antiparallel along x) and $\mathbf{Q}_2 = (0, \pi)$ (corresponding to spins parallel along x and antiparallel along y). Below T_N nearest neighbor spins are parallel or antiparallel depending on whether they are connected by a short or long bond, however, in the nematic phase above T_N but below T_s the magnetic fluctuations centered around $\mathbf{Q}_1$ become weaker or stronger than those centered around $\mathbf{Q}_2$, depending on whether the b-axis is parallel or perpendicular to $\mathbf{Q}_1$, respectively. Mathematically, this allows one to define the nematic order parameter $\bar{\phi}$ in terms of the (spin unpolarized) magnetic susceptibility $\chi(\mathbf{q})$ according to $\phi \equiv \chi^{-1}(\mathbf{Q}_2) - \chi^{-1}(\mathbf{Q}_1)$[11]. Such an interplay between nematic and spin degrees of freedom has been indeed observed by neutron scattering [43, 42, 41, 80] and nuclear magnetic resonance (NMR) experiments in twinned and detwinned doped $BaFe_2As_2$,

LaFeAsO and $NaFe_{1-x}Co_xAs$ crystals [81, 82, 23, 40, 83].

7.1.1 Orbital degrees of freedom

However, orbital degrees of freedom also participate actively in the nematic phase. This leads to the well-known effect that tetragonal symmetry-breaking is also manifested by a ferro-orbital polarization that makes the occupation of the Fe d_{xz} orbitals different than the occupation of the Fe d_{yz} orbitals [84]. Spin-orbit coupling (SOC), which converts anisotropies in real space into anisotropies in spin space, plays a central role controlling the interplay between spin and nematic degrees of freedom [67]. On one hand, SOC forces the spins to point along the ordering vector direction below T_N. This effect takes place even at zero applied strain, and is manifested by the fact that the three diagonal magnetic susceptibilities, $\chi_{\alpha\alpha}(\mathbf{Q}_1)$, where $\alpha = x, y, z$, are different already in the paramagnetic tetragonal phase. Indeed, the distinct behavior of in-plane and out-of-plane spin fluctuations is well documented in the literature via polarized neutron scattering measurements [85, 86], NMR measurements [18, 87, 88], and theoretical considerations [69].

7.1.2 Spin structure of the nematic order

The evolution of the spin fluctuation anisotropy under strain has been less explored, but can shed light on the unique spinspace structure of the nematic order parameter. This is defined mathematically by $\bar{\phi}_{\alpha\beta} = \chi^{-1}_{\alpha\alpha}(\mathbf{Q}_2) - \chi^{-1}_{\beta\beta}(\mathbf{Q}_1)$. Clearly, the nematic order parameter $\bar{\phi}$ defined above can be understood as an average over all possible polarizations, $\bar{\phi} = \frac{1}{9}\sum_{\alpha\beta}\phi_{\alpha\beta}$. As discussed in A.1, the space-group symmetry of the iron pnictides forces many of these combinations to vanish, yielding only three non-zero-independent components: ϕ_{xy}, ϕ_{yx}, and ϕ_{zz}. This important property of spin-nematicity has not been discussed previously in the literature. Experimentally, probing the spin structure of the nematicity would require polarized neutron scattering measurements in detwinned samples above the magnetic transition temperature. Polarized experiments inside the magnetically ordered phase probe a completely

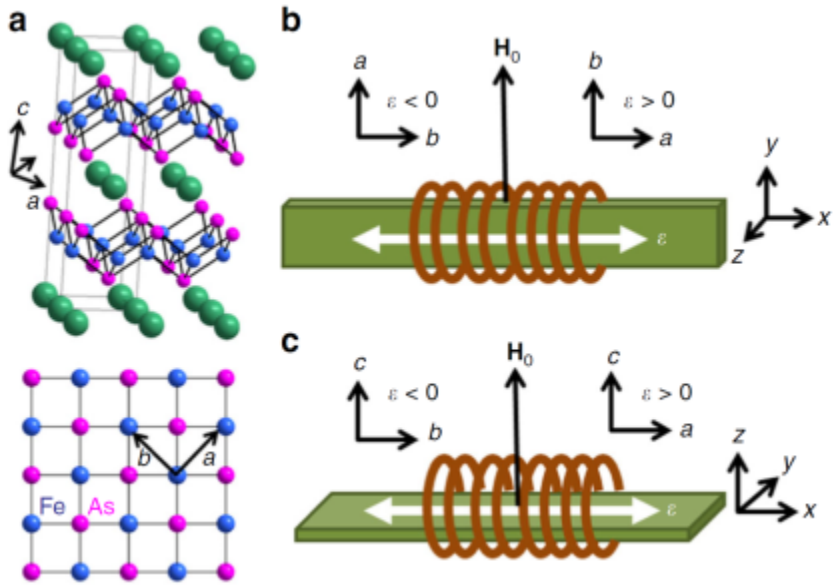

Figure 7.1: Application of uniaxial strain. **a** Crystal structure of $BaFe_2As_2$, with Ba (green), Fe (blue) and As (magenta) sites shown. Lower panel shows the Fe–As layer in the tetragonal phase, with arrows indicating the unit cell axes of the orthorhombic phase $\left(a \parallel (110)_{tet}, b \parallel (1\bar{1}0)_{tet}\right)$. **b**, **c** Orientation of the magnetic field with respect to the coil ($\mathbf{H}_1$) and strain axis for $\mathbf{H}_0 \perp c$ (**b**) and $\mathbf{H}_0 \parallel c$ (**c**). For positive (tensile) strain $\mathbf{H}_0$ is parallel to (**b**), whereas for negative (compressive) strain $\mathbf{H}_0$ is along (**a**)

different type of anisotropy, related to long-range magnetic order, and not to the fluctuation spectrum [89, 90, 91]. Elucidating this hitherto unknown spin structure of the nematic order parameter is fundamental to shed light on the intricate interplay between orbital, spin, and lattice degrees of freedom, which are ultimately responsible for the superconducting instability of the system.

7.2 Results

We have performed NMR spin-lattice relaxation measurements to probe the anisotropy of the spin fluctuations under fixed strain in the paramagnetic phase of $BaFe_2As_2$. The role of the applied uniaxial strain is to provide a small tetragonal symmetry-breaking field, akin to externally applied magnetic fields in ferromagnets. In contrast to previous works, here we probe the magnetic fluctuation anisotropy both in real space and in spin space—more specif-

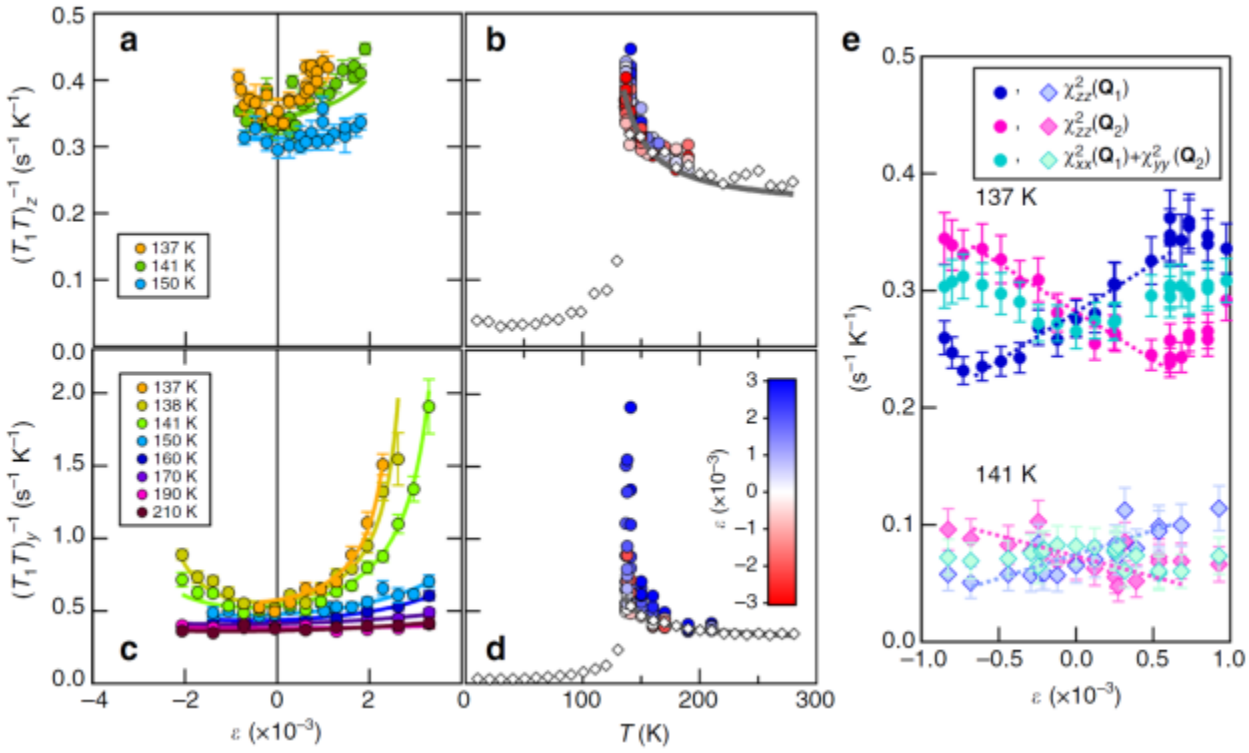

Figure 7.2: Strain and temperature dependence of the spin-lattice relaxation rate. $T_1T_{yz}^{-1}$ vs. strain (**a**, **c**) and vs. temperature (**b**, **d**). The solid lines are fits as described in the text, and error bars are determined from least squares fitting as described in A.3. The open diamonds in b, d are reproduced from [4]. **e** $\chi^2_{zz}(\mathbf{Q}_1)$, $\chi^2_{zz}(\mathbf{Q}_2)$, and $\chi^2_{xx}(\mathbf{Q}_1)+\chi^2_{yy}(\mathbf{Q}_2)$ as a function of strain at 137 K and 141 K. The data have been displaced vertically for clarity. The dashed lines are guides to the eye, and the error bars are determined by propagating the errors in **a-d**

ically, we determine each of the nematic susceptibilities associated with the three nematic components ϕ_{xy}, ϕ_{yx}, and ϕ_{zz}. Our main result is that the three nematic components respond differently to external strain, i.e., nematic order induces not only real-space anisotropy, but also affects the spin-space anisotropy. In particular, we find that the out-of-plane spin fluctuations centered at $\mathbf{Q} \parallel \hat{a}$ are more strongly enhanced by the strain, as compared to the spin fluctuations polarized along the longer in-plane axis. This raises the interesting possibility of reversing the spin polarization of the system from in-plane to out-of-plane by applying a sufficiently strong in-plane strain. Importantly, these observations were confirmed by neutron scattering measurements [92]. The easy axis for the spins changes from in-plane to out-of-plane depending on the applied stress. More broadly, our results thus open a new

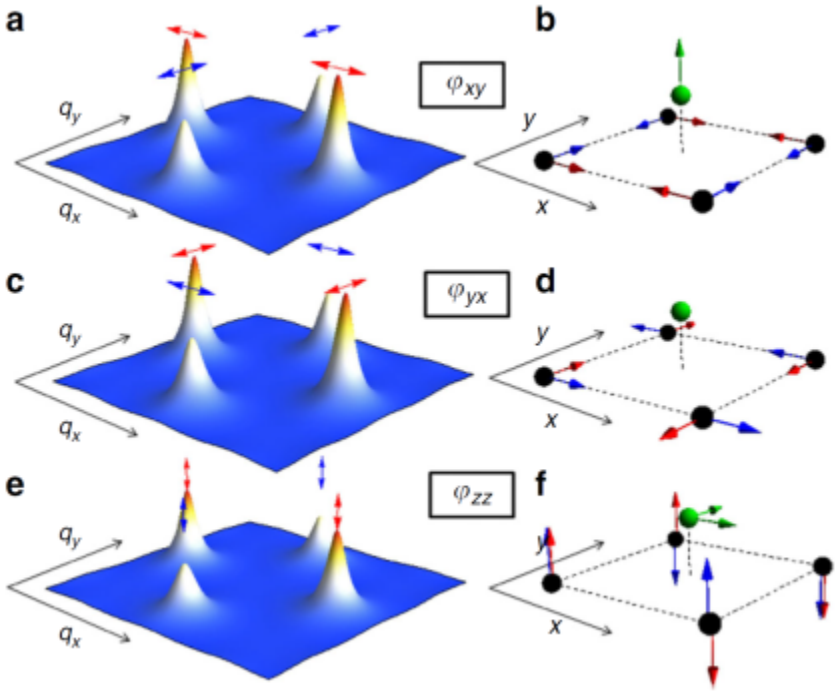

Figure 7.3: Spin-space structure of the spin-nematic order parameter. Spin fluctuations in momentum space (left) and in real space (right) and polarization directions of the Fe spins for the three nematic components, ϕ_{xy} (**a**, **b**), ϕ_{yx} (**c**, **d**), and ϕ_{zz} (**e**, **f**). The red arrows correspond to the magnetic ordering vector $\mathbf{Q}_1 = (\pi, 0)$ and the blue arrows correspond to $\mathbf{Q}_2 = (0, \pi)$. The black spheres are the Fe sites, the green sphere is the As site, and the green arrows indicate the direction of the hyperfine field

avenue toward magneto-mechanical manipulation of strongly correlated systems that display nematic order.

7.2.1 Experimental setup

Single crystals of $BaFe_2As_2$ were cut along the tetragonal (110) direction and mounted in the cryogenic CS100 strain cell with field oriented both parallel and perpendicular to the crystallographic *c*-axis, as shown in Fig. 7.1.A free-standing NMR coil was placed around the sample prior to securing the ends of the crystal in the strain device with epoxy. The radiofrequency field $\mathbf{H}_1$ is oriented parallel to the strain axis, which is always perpendicular to the external field, $\mathbf{H}_0$. In our device, strain is always applied along the x-axis defined in Fig. 7.1; since the *b*-axis is defined as the shorter axis, positive (i.e., tensile) strain corresponds

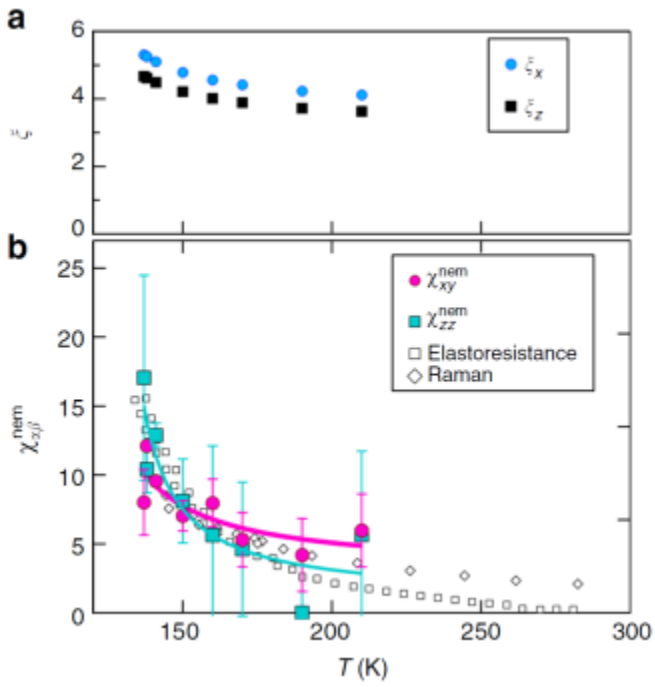

Figure 7.4: Temperature dependence of the nematic susceptibilities. **a** Correlation lengths $\xi_{x,z}(0)$ at zero strain, and **b** nematic susceptibilities $\chi^{nem}_{xy,zz}$ vs. temperature, based on the fits (solid lines) shown in Fig 7.2. Also shown are the nematic susceptibilities measured by Raman and elastoresistance measurements, reproduced from refs. [5, 6, 7], respectively. The solid lines are fits as described in the text. The error bars are determined from least squared minimization fits, holding the $\xi_{x,z}(0)$ parameters fixed, as described in Supplementary Note 4

to $x \parallel a$ and $y \parallel b$, whereas negative (i.e., compressive) strain gives $y \parallel a$ and $x \parallel b$. When the crystal is strained by applying voltage to the piezoelectric stacks, the displacement, x, is measured by a capacitive dilatometer, and strain is calculated as $\epsilon = (x - x_0)/L_0$, where L_0 is the unstrained length of the crystal. To account for differential thermal contraction, the zero-strain displacement, x_0, was determined by the condition that the quadrupolar splitting $\nu_{\alpha\alpha}$ satisfies the tetragonal-symmetry relationship $|\nu_{xx}| = |\nu_{yy}| = |\nu_{zz}|/2$, as described in 7.3. The linear relationship between $\nu_{\alpha\alpha}$ and strain (Figure 7.5) indicates that both positive and negative strains are achieved, without bowing of the crystal. The field $\mathbf{H}_0$ was oriented either along the z-direction parallel to the crystalline c-axis, or in the plane of the crystal along the y-direction, as shown in Fig. 7.1.

7.3 Spectral Measurements

When the crystal is strained by applying voltage to the piezoelectric stacks, the displacement, x, is measured by a capacitive position sensor, and strain is calculated as $\epsilon = (x - x_0)/L_0$, where L_0 is the unstrained length of the crystal. It is crucial to determine the unstrained displacement, x_0, at cryogenic temperatures due to differential thermal contraction between the strain device and the sample. This value can be obtained by observing the asymmetry of the electric field gradient (EFG) tensor. The spectra were measured by acquiring echoes while sweeping the magnetic field H_0 at fixed frequency. The quadrupolar satellite resonances occur at fields $H_{sat} = (f_0 \pm \nu_{\alpha\alpha})/\gamma(1 + K_{\alpha\alpha})$, where f_0 is the radiofrequency, $\gamma = 7.29019$MHz/T is the gyromagnetic ratio, $K_{\alpha\alpha}$ and $\nu_{\alpha\alpha}$ are the Knight shift and EFG tensor components in the $\alpha = (x, y, z)$ direction [17, 12]. The central transition field is given by: $H_{cen} = \frac{f_0}{\gamma(1+K_{\alpha\alpha})}\left(\frac{1}{2} + \sqrt{\frac{3f_0^2 - 2\left(\nu_{\beta\beta}+\nu_{\alpha\alpha}\right)^2}{12}}\right)$, where $\beta = (y, x, z)$ for $\alpha = x, y, z$.

Figure 7.5(b) shows a typical field-swept NMR spectrum of ^{75}As, revealing a narrow central transition ($I_z = 1/2 \leftrightarrow -1/2$) and two quadrupolar satellite peaks ($\pm 3/2 \leftrightarrow \pm 1/2$). The spectrum was fit to the sum of three Gaussians to extract both the Knight shift, $K_{\alpha\alpha}$, and the EFG, $\nu_{\alpha\alpha}$. The EFG tensor is given by $\nu_{\alpha\beta} = (eQ/12h)\,\partial^2 V/\partial x_\alpha \partial x_\beta$, where Q is the quadrupolar moment of the ^{75}As and V is the electrostatic potential at the As site. This quantity is dominated by the occupation of the $d_{xz,yz}$ orbitals of the neighboring Fe atoms, and the EFG asymmetry $\eta = (\nu_{yy} - \nu_{xx})/(\nu_{yy} + \nu_{xx})$ is a measure of the nematic order parameter [46, 44]. Note that the magnetic field lies along the shorter b-axis under tensile strain ($\epsilon > 0$), and along the longer a-axis under compressive strain ($\epsilon < 0$), as shown in Figure A.1 of the main text. The EFG enables us to identify the zero-strain displacement, x_0, by the condition $|\nu_{xx}| = |\nu_{yy}| = |\nu_{zz}|$. As shown in Figure 7.5(c), ν_{yy}, and hence $\eta(\epsilon) = (\nu_{yy}(\epsilon) - \nu_{yy}(-\epsilon))/(\nu_{yy}(\epsilon) + \nu_{yy}(-\epsilon))$, varies linearly with strain.

Despite the fact that the EFG varies with strain, we find no significant variation of the satellite linewidth with strain. The strong variation of the EFG with strain explains the

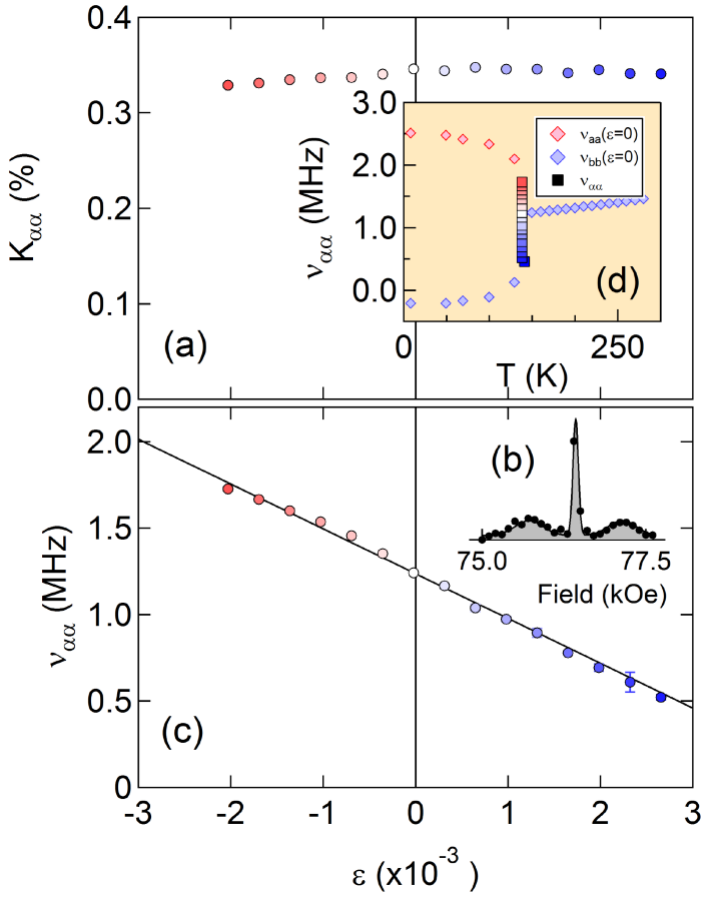

Figure 7.5: Knight shift and EFG Versus Strain. (a) Knight shift versus strain at 138K. (b) The ^{75}As spectrum at 138K for a strain level of 0.0265% at frequency 55.924MHz. The solid line is a fit to the spectrum as described in the text. (c) The quadrupolar splitting versus strain, and (d) versus temperature. The zero-strain points (diamonds) are reproduced from Ref. [4]

quadrupolar broadening observed in Co, Ni or Cu-doped $Ba(Fe,M)_2As_2$ [56, 57, 58]. The dopant atoms create an inhomogeneous strain field that gives rise to a distribution of local EFGs. Recently a finite value of $\eta \sim 0.1$ was reported in the tetragonal phase of unstrained $BaFe_2(As_{1-x}P_x)_2$ above T_s [44]. The origin of this finite nematicity is likely due to local defects, and based on our results the strain fields are on the order of 0.05%.

The Knight shift is shown versus strain in Figure 7.5(a) for $\mathbf{H}_0 \perp c$. The in-plane Knight shift shows little or no variation with ϵ, such that $(K_{xx} - K_{yy})/K_{yy} \leq 3\%$ at the highest strain levels in this material. This result is surprising because the same quantity is approximately 6% in the nematic phase of FeSe [93]. Recent static susceptibility measurements in

$BaFe_2As_2$ under strain indicate that χ_{xx} and χ_{yy} in the paramagnetic phase differ by only 5% [34]. This result suggests that $\chi_{\alpha\alpha}(\mathbf{q}=0)$ couples only weakly to the strain.

7.3.1 Response of spin susceptibility to strain

The ^{75}As ($I = 3/2$) spin lattice relaxation rate divided by temperature, $(T_1T)^{-1}_{\mu}$, for different field orientations $\mu = z, y$ is shown in Fig. 7.2 both as a function of strain ϵ and temperature T. It is striking that while $(T_1T)^{-1}_{z}$ increases by $\sim$ 30% at 137K for the largest applied strain ($\sim$ 0.3%), $(T_1T)^{-1}_{y}$ increases by 500%. In both cases, both positive and negative strain increase $(T_1T)^{-1}$ in a nonlinear fashion. This behavior is a manifestation of the spin anisotropy induced by nematic order, and the enhancement of T_N under strain. More precisely, the spin lattice relaxation rate is primarily dominated by the fluctuations of the local hyperfine field at the As site, which in turn is determined by the neighboring iron spins according to:

$$\left(\frac{1}{T_1T}\right)_{\mu} = \frac{\gamma^2}{2}\lim_{\omega\to 0}\sum_{\mathbf{q},\alpha,\beta}\mathcal{F}^{(\mu)}_{\alpha\beta}(\mathbf{q})\frac{Im\chi_{\alpha\beta}(\mathbf{q},\omega)}{\hbar\omega} \tag{7.1}$$

where γ is the nuclear gyromagnetic factor, $\mathcal{F}^{(\mu)}_{\alpha\beta}$ are the hyperfine form factors, which depend on the field direction μ A.2, $\chi_{\alpha\beta}(\mathbf{q},\omega)$ is the dynamical magnetic susceptibility, and $\alpha, \beta = \{x, y, z\}$ [18]. Because the system is metallic, spin fluctuations experience Landau damping, resulting in the low energy dynamics $\chi^{-1}_{\alpha\beta}(\mathbf{q},\omega) = \chi^{-1}_{\alpha\beta}(\mathbf{q},\omega) - i\hbar\omega/\Gamma$, where Γ is the Landau damping, as seen by neutron scattering experiments [94]. Consequently, $\lim_{\omega\to 0}\frac{Im\chi_{\alpha\beta}(\mathbf{q},\omega)}{\hbar\omega} = \frac{1}{\Gamma}\chi^2_{\alpha\beta}(\mathbf{q})$, i.e., the spin-lattice relaxation rate is proportional to the squared susceptibility integrated over the entire Brillouin zone.

Since the magnetically ordered state has wave-vectors $\mathbf{Q}_1 = (\pi, 0)$ and $\mathbf{Q}_2 = (0, \pi)$, one expects that the susceptibility is peaked at these two momenta, as demonstrated in Fig. 7.3. Indeed, neutron scattering experiments confirm that the magnetic spectral weight is strongly peaked at $\mathbf{Q}_1$ and $\mathbf{Q}_2$ [41]. A finite nematicity corresponds to a difference in the relative weights of these peaks, and the physical meaning of each component of the

nematic order, $\phi_{\alpha\beta}$, is depicted in Fig. 7.3; for instance, ϕ_{xy} is a measure of the asymmetry between spin fluctuations peaked at $\mathbf{Q}_1$ and polarized along the x-axis, and spin fluctuations peaked at $\mathbf{Q}_2$ and polarized along the y-axis. The magnetic fluctuations associated with each spin polarization pattern generate very different types of fluctuating local hyperfine fields experienced by the As, which couples to the four nearest neighbor Fe spins via a transferred hyperfine interaction (Fig. 7.3) [18].

As an initial step to elucidate the effect of strain on the spin fluctuation anisotropy, we consider that the susceptibility is sharply peaked at these two magnetic ordering vectors. Evaluation of the hyperfine form factors yields the following:

$$\begin{aligned}
(T_1T)_x^{-1} &\propto \chi_{xx}^2(\mathbf{Q}_1) + \chi_{yy}^2(\mathbf{Q}_2) + \chi_{zz}^2(\mathbf{Q}_2), \\
(T_1T)_y^{-1} &\propto \chi_{xx}^2(\mathbf{Q}_1) + \chi_{yy}^2(\mathbf{Q}_2) + \chi_{zz}^2(\mathbf{Q}_1), \\
(T_1T)_z^{-1} &\propto \chi_{zz}^2(\mathbf{Q}_1) + \chi_{zz}^2(\mathbf{Q}_2)
\end{aligned} \tag{7.2}$$

where the prefactors are approximately the same in all equations (see A.2), and proportional to the off-diagonal hyperfine matrix element $\mathcal{F}_{xz}$ coupling in-plane Fe spin fluctuations to out-of-plane As hyperfine fields (and vice-versa). The fact that $\chi_{zz}(\mathbf{Q}_i)$ contributes to T_1 for all directions of the applied magnetic field is thus consistent with the hyperfine field analysis depicted in Fig. 7.3, since out-of-plane spin fluctuations on the Fe sites produce hyperfine fluctuating fields in the As sites along both in-plane directions. Similarly, the fact that only $\chi_{xx}(\mathbf{Q}_1)$ and $\chi_{yy}(\mathbf{Q}_2)$ contribute to T_1 for external fields applied along the plane is a consequence of the fact that these spin fluctuations generate hyperfine fields in the As site oriented out of the plane.

Because by symmetry $(T_1T)_x^{-1}(\epsilon) = (T_1T)_y^{-1}(-\epsilon)$, the NMR data can be used to extract the strain and temperature dependence of the three polarized spin-susceptibility combinations $\chi_{zz}^2(\mathbf{Q}_1)$, $\chi_{zz}^2(\mathbf{Q}_2)$, and $\chi_{xx}^2(\mathbf{Q}_1) + \chi_{yy}^2(\mathbf{Q}_2)$, as shown in Fig. 7.2e. This analysis provides several interesting insights. First, focusing on the out-of-plane fluctuations, in-plane strain enhances spin fluctuations around one of the two ordering vectors ($\chi_{zz}(\mathbf{Q}_1)$ for $\epsilon > 0$

and $\chi_{zz}(\mathbf{Q}_2)$ for $\epsilon < 0$) at the same time as it suppresses the fluctuations around the other ordering vector. Therefore, in-plane strain transfers magnetic spectral weight between the two dominant out-of-plane spin-fluctuation channels. This is consistent with neutron scattering experiments in detwinned pnictides [43], which, however, only probed the unpolarized susceptibility. More importantly, this behavior is a direct manifestation of the response of the nematic order parameter ϕ_{zz} to strain, since $\phi_{zz} = \chi_{zz}^{-1}(\mathbf{Q}_2) - \chi_{zz}^{-1}(\mathbf{Q}_1)$.

Turning now to the average in-plane fluctuations $\chi_{xx}^2(\mathbf{Q}_1) + \chi_{yy}^2(\mathbf{Q}_2)$, we note that, in contrast to the quantity $\chi_{zz}^{-1}(\mathbf{Q}_1) - \chi_{zz}^{-1}(\mathbf{Q}_2)$, it is an even function of the applied strain. This behavior can be attributed to the response of the nematic order parameter $\phi_{xy} = \chi_{xx}^{-1}(\mathbf{Q}_2) - \chi_{yy}^{-1}(\mathbf{Q}_1)$ to strain. Similarly to ϕ_{zz}, ϕ_{xy} promotes a transfer of magnetic spectral weight, but now between x-polarized spin fluctuations around $\mathbf{Q}_1$ and y-polarized spin fluctuations around $\mathbf{Q}_2$. Since only the combination $\chi_{xx}^2(\mathbf{Q}_1) + \chi_{yy}^2(\mathbf{Q}_2)$ contributes to the spin-lattice relaxation rate, the total magnetic spectral weight remains the same to linear order in ϕ_{xy}, since what is suppressed in, say, $\chi_{yy}(\mathbf{Q}_2)$ is tranferred to $\chi_{xx}(\mathbf{Q}_1)$. Of course, as strain is enhanced, nonlinear effects quadratic in ϕ_{xy}^2 take place, in agreement with the behavior displayed in Fig. 7.2e. Note that the third nematic order parameter, $\phi_{yx} = \chi_{yy}^{-1}(\mathbf{Q}_2) - \chi_{xx}^{-1}(\mathbf{Q}_1)$, does not affect the in-plane fluctuations that contribute the most to the spin-lattice relaxation rate. This is not unexpected, since the spin fluctuations associated with $\chi_{yy}(\mathbf{Q}_1)$ and $\chi_{xx}(\mathbf{Q}_2)$ do not generate hyperfine fields in the As sites, as shown in Fig. 7.3.

The most striking feature of Fig. 7.2e is that the out-of-plane spin fluctuations seem to have a larger response to in-plane strain than the in-plane spin fluctuations. This observation suggests that the nematic susceptibility associated with ϕ_{zz}, $\chi_{zz}^{nem} \equiv \partial\phi_{zz}/\partial\epsilon$, is larger than the nematic susceptibility associated with ϕ_{xy}, $\chi_{xy}^{nem} \equiv \partial\phi_{xy}/\partial\epsilon$, and is a manifestation of the fact that nematic order induces not only real-space anisotropy, but also spin-space anisotropy. To make this analysis more quantitative, we fit the full temperature, strain, and field orientation dependence of T_1 to a model that incorporates the fact that the magnetic

fluctuations are not infinitely peaked at the ordering vectors $\mathbf{Q}_{1,2}$, since the magnetic correlation length is finite above the magnetic transition. In the tetragonal phase, there are three different magnetic correlation lengths, ξ_x, ξ_y, and ξ_z, associated, respectively, with the pairs of peaks ($\chi_{xx}(\mathbf{Q}_1)$, $\chi_{yy}(\mathbf{Q}_2)$); ($\chi_{yy}(\mathbf{Q}_1)$, $\chi_{xx}(\mathbf{Q}_2)$), and ($\chi_{zz}(\mathbf{Q}_1)$, $\chi_{zz}(\mathbf{Q}_2)$). This spin anisotropy is intrinsic to the tetragonal crystalline symmetry and is enforced by the spin-orbit coupling even in the absence of nematic order as shown previously by polarized neutron scattering [85, 86, 89, 90, 91]. Nematic order induced by strain breaks the equivalence between these pairs of peaks, splitting the correlation lengths into $\xi_x^{-2} = \xi_x^{-2} \mp \phi_{xy}$, $\xi_y^{-2} = \xi_y^{-2} \mp \phi_{yx}$, and $\xi_z^{-2} = \xi_z^{-2} \mp \phi_{zz}$. This model is similar to the one used previously in ref. [23] and is described in A.2.

The fits for $(T_1T)_z^{-1}$ and $(T_1T)_y^{-1}$ in the absence of strain are shown as solid gray lines in Fig. 7.2b, d for $\xi_x = \xi_y$. We find $\xi_z/\xi_x = 0.88$, in agreement with the fact that in the absence of strain the spins point along the plane ((since $\xi_x > \xi_z$, spins are more correlated along x)). Moreover, the temperature dependence of $\xi_x(T)$, shown in Fig. 7.4a, gives values consistent with those measured by inelastic neutron scattering [95]. Having fixed the unstrained parameters, we perform fits in the presence of strain, shown by the solid lines in Fig. 7.2a, c. The only parameters introduced in this case are ϕ_{xy} and ϕ_{zz}. The good agreement between the fitted and the experimental curves of both $(T_1T)_z^{-1}$ and $(T_1T)_y^{-1}$ over a wide temperature-strain regime demonstrates the suitability of the phenomenological model employed in our analysis.

The temperature and strain behaviors of the nematic order parameters $\phi_{\alpha\beta}$ allow us to extract the temperature dependence of the nematic susceptibilities χ_{xy}^{nem} and χ_{zz}^{nem}, as shown in Fig. 7.4b. The data suggest that $\chi_{zz}^{nem} > \chi_{xy}^{nem}$, particularly close to the magnetic transition. This quantitative analysis corroborates the qualitative conclusion above, namely that nematic order induces anisotropies in spin-space, and that the out-of-plane spin fluctuations are more strongly enhanced by in-plane strain than the in-plane spin fluctuations. The in-plane spin fluctuations, are nevertheless larger, giving rise to in-plane ordering at T_N.

It is interesting to compare χ_{xy}^{nem} and χ_{zz}^{nem} with the nematic susceptibility extracted from elastoresistance [7] and from electronic Raman spectroscopy experiments [5]. As shown in Fig. 7.4b, the values are consistent, and the NMR-extracted nematic susceptibilities also follow a Curie–Weiss type of behavior [6], with a Curie temperature $T_0 = 116$K comparable to that extracted from the elastoresistance [7]. Note, however, that, in contrast to our NMR analysis, the other probes for the nematic susceptibility are not sensitive to the spin-space structure of the nematic susceptibility.

7.4 Conclusion

The surprising anisotropic response of different nematic components to in-plane strain reveals that the spin polarization can be controlled by lattice distortions, similar to a piezomagnetic effect. In particular, the result $\chi_{zz}^{nem} > \chi_{xy}^{nem}$ implies that for sufficiently large strain $\epsilon*$, the dominant spin polarization will shift from in-plane to out-of-plane. Recent NMR and neutron studies in unstrained FeSe have uncovered similar evidence for a large spin susceptibility along the c-axis in the nematic phase, above T_c [93, 96]. However, the observation of large c-axis spin fluctuations in FeSe does not reveal information about the temperature dependence of the various nematic susceptibility components, $\chi_{\alpha\alpha}^{nem}$, which necessarily require the application of strain. For $BaFe_2As_2$, the value of $\epsilon*$ can be estimated from the condition that the out-of-plane magnetic correlation length $\tilde{\chi}_z^{-2} = \chi_z^{-2} - \chi_{zz}^{nem}\epsilon$ becomes larger than the in-plane magnetic correlation length $\tilde{\chi}_x = \chi_x - \chi_{xy}^{nem}\epsilon$, yielding $\epsilon* \approx 0.4\%$ close to the magnetic transition temperature, assuming a linear strain response. Such a strain value, which is just beyond the capability of our specific piezo device, can reasonably be achieved by similar types of devices, however. More importantly, this analysis opens a new avenue to control spin polarization in nematic materials without using magnetic fields, but instead by using mechanical strain. Since nematic order has been observed in other correlated materials

such as cuprates and ruthenates, it will be interesting to investigate whether similar sizable effects are present in these systems as well.

Chapter 8

Conclusion

Our studies indicate that iron-based superconductors are very sensitive to uniaxial strain. We utilized two methods to apply strain. For our initial NMR experiments we used a simple U-shaped horseshoe assembly that allowed us to observe T_1 anisotropy in Co-doped $BaFe_2As_2$. This motivated us to go further and use a novel piezoelectric based device that allowed in-situ strain control to measure NMR quantities such as the T_1 and the electric quadrupole splitting versus uniaxial strain.

The EFG results on the parent $BaFe_2As_2$ showed a linear response to the external strain. The nematic susceptibility was extracted from the slopes of EFG vs strain. The nematic susceptibility showed a Curie-Weiss dependence. This result shows that nematicity in iron-based superconductors acts similar to ferromagnetic materials. The sensitivity of the EFG reponse to the applied strain allows us to determine the strain homogeneity in the sample. Comparison of the width of the As satellites with the EFG response shows that the applied strain across the sample was very homogeneous. This observation stimulated the idea of non-invasive detection of defects in the materials that have strong response to the external strain.

This work also presents the results of T_1 measurements under uniaxial strain for the parent and Co-doped $BaFe_2As_2$. For the Co-doped material, the applied strain breaks the

C_4 symmetry and the spin-lattice relaxation rate becomes anisotropic. Significant changes of the spin-lattice relaxation rate with temperature were observed as well. T_1 measurements on $BaFe_2As_2$ were performed using a CS100 device. Detailed measurements of T_1 vs strain were made for in-plane and out-of-plane orientations and we observed non-linear changes. The T_1 response for the two orientations was highly anisotropic with 30% increase for field parallel to z and 500% increase for y. This big response is due to strong spin-orbit coupling in this material. This interplay between lattice and spin degrees of freedom suggests the possible control of the material's magnetic properties via piezomagnetism.

To the best of our knowledge, our results are the first to reveal the internal spin structure of the nematic order parameter in iron-based superconductors. This behavior is a clear manifestation of the entanglement between spin, orbital, and lattice degrees of freedom in the normal state of these compounds. Since superconductivity emerges from this unique state, the rich interplay between these different degrees of freedom revealed by our NMR analysis will certainly affect the properties of the superconducting state.

Appendix A

Spin-Lattice Relaxation Model

A.1 Spin-space structure of the nematic order parameter

To fully understand the NMR results, it is vital to understand both the spatial structure and vector orientations of the Fe spins. This information is contained in the spin susceptibility tensor, $\chi_{\alpha\beta}(\mathbf{r}, t)$, where $\alpha, \beta = x, y, z$. The nematicity in this system depends on the q-space structure of $\chi_{\alpha\beta}$, which is defined as:

$$\chi_{\alpha\beta}(\mathbf{q}) = \frac{1}{2\pi^3} \int d\mathbf{r}^3 e^{i\mathbf{r}\cdot\mathbf{q}} \chi_{\alpha\beta}(\mathbf{r}) \tag{A.1}$$

The nematic order parameter naturally acquires an internal spin structure, since one defines $\phi_{\alpha\beta} = \chi^{-1}_{\alpha\alpha}(\mathbf{Q}_2) - \chi^{-1}_{\beta\beta}(\mathbf{Q}_1)$ where $\mathbf{Q_1}$ and $\mathbf{Q_2}$ are the propagation vectors corresponding to stripes of anti-parallel spins along the x axis, $\mathbf{Q_1} = (\pi, 0)$, and stripes of anti-parallel spins along the y axis, $\mathbf{Q_2} = (0, \pi)$, respectively. The space-group symmetry of the iron pnictides forces many of these combinations to vanish, yielding only three non-independent components: ϕ_{xy}, ϕ_{yx}, and ϕ_{zz}. To make these points sharper, we employ simple Ginzburg-Landau considerations. There are two magnetic order parameters, $\mathbf{M}_1$ and $\mathbf{M}_2$, which correspond

to the propagation vectors $\mathbf{Q}_1 = (\pi, 0)$ and $\mathbf{Q}_2 = (0, \pi)$, respectively. These are Heisenberg spins, thus the vectors have 3 components. If the spins were completely uncoupled to the lattice, the free energy F would be isotropic in spin space, and therefore would depend only on $M_1^2 = M_{1,x}^2 + M_{1,y}^2 + M_{1,z}^2$ and $M_2^2 = M_{2,x}^2 + M_{2,y}^2 + M_{2,z}^2$. Because M_1 and M_2 are related by a 90° rotation and because the system is tetragonal, M_1 and M_2 are not two independent parameters but are constrained. As a result, the free energy must depend only on the combination $(M_1^2 + M_2^2)$, i.e. $F = a\left(M_1^2 + M_2^2\right) + \mathcal{O}\left(M^4\right)$, where $a \propto T - T_N$, and T_N is the mean-field transition temperature [72]. Note that, here, below T_N, the magnetization can point in any direction in spin space.

Now, in the real systems, the spins are coupled to the crystal fields via spin-orbit coupling (SOC). This induces spin anisotropies that force the spins to point along certain directions. As demonstrated in Ref. [69], in a tetragonal system (i.e. above T_N and the nematic/structural transition T_s), there are three spin-anisotropic terms generated by the SOC:

$$F = (a + \alpha_1)\left(M_{1,x}^2 + M_{2,y}^2\right) + (a + \alpha_2)\left(M_{1,y}^2 + M_{2,x}^2\right) + (a + \alpha_3)\left(M_{1,z}^2 + M_{2,z}^2\right) + \mathcal{O}\left(M^4\right) \tag{A.2}$$

The first additional term corresponds to $\mathbf{M}_i \parallel \mathbf{Q}_i$, the second additional term corresponds to $\mathbf{M}_i \perp \mathbf{Q}_i$ and in-plane, and the third additional term corresponds to $\mathbf{M}_i \perp \mathbf{Q}_i$ and out-of-plane. Clearly, the smaller α_i determines the direction of the magnetization below the magnetic transition temperature. Importantly, note that tetragonal symmetry is fully preserved: spin fluctuations polarized along $x/y/z$ and centered at $\mathbf{Q}_1$ are equivalent to spin fluctuations polarized along $y/x/z$ (respectively) and centered at $\mathbf{Q}_2$. Polarized inelastic neutron scattering or NMR spin-lattice relaxation rate measurements in the paramagnetic phase probe precisely these terms. This has been widely explored in the literature.

Nematic order is manifested in the spin spectrum as an inequivalence between magnetic fluctuations centered around $\mathbf{Q}_1$ and $\mathbf{Q}_2$. If the system had full spin-rotational invariance,

the spin-nematic order parameter would be then simply:

$$\phi = \langle M_1^2 \rangle - \langle M_2^2 \rangle$$

This is precisely the order parameter that has been widely explored in the theoretical literature, and measured experimentally in unpolarized inelastic neutron scattering measurements in detwinned samples. However, because the SOC introduces spin anisotropies, there are actually different combinations of spin-polarized fluctuations centered around $\mathbf{Q}_1$ and $\mathbf{Q}_2$. They can be derived from symmetry considerations: as shown in the free energy A.2, tetragonal symmetry imposes that spin fluctuations polarized along $x/y/z$ and centered at $\mathbf{Q}_1$ are equivalent to spin fluctuations polarized along $y/x/z$ (respectively) and centered at $\mathbf{Q}_2$. Thus, there are three different combinations that break the equivalence between fluctuations centered around $\mathbf{Q}_1$ and $\mathbf{Q}_2$:

$$\begin{aligned} \phi_{xy} &= \langle M_{1,x}^2 \rangle - \langle M_{2,y}^2 \rangle \\ \phi_{yx} &= \langle M_{1,y}^2 \rangle - \langle M_{2,x}^2 \rangle \\ \phi_{zz} &= \langle M_{1,z}^2 \rangle - \langle M_{2,z}^2 \rangle \end{aligned} \tag{A.3}$$

The fact that these three terms break the same tetragonal symmetry implies that they must be either all zero or all non-zero. However, the SOC enforces different values for these three order parameters. In other words, the nematic order parameter naturally acquires a spin structure due to the SOC, i.e. the real-space anisotropy becomes entangled with the spin-space anisotropy.

The uniaxial strain ϵ applied to the system breaks explicitly the tetragonal symmetry and induces an additional contribution to the free energy:

$$\delta F = \lambda_1 \epsilon \left(M_{1,x}^2 - M_{2,y}^2 \right) + \lambda_2 \epsilon \left(M_{1,y}^2 - M_{2,x}^2 \right) + \lambda_3 \epsilon \left(M_{1,z}^2 - M_{2,z}^2 \right)$$

By varying the external strain ϵ, we can then extract the nematic susceptibility of each spin-nematic order parameter separately:

$$\chi_{xy}^{nem} = \frac{\partial \phi_{xy}}{\partial \epsilon},\ \chi_{yx}^{nem} = \frac{\partial \phi_{yx}}{\partial \epsilon},\ \chi_{zz}^{nem} = \frac{\partial \phi_{zz}}{\partial \epsilon}$$

A.2 Spin-Lattice Relaxation Model

As stated in the main text, the spin-lattice relaxation rate is given by:

$$\left(\frac{1}{T_1 T}\right)_\mu = \frac{\gamma^2}{2} \sum_{\mathbf{q},\alpha,\beta} \mathcal{F}_{\alpha\beta}^{(\mu)}(\mathbf{q}) \frac{Im\chi_{\alpha\beta}(\mathbf{q},\omega)}{\hbar\omega} \tag{A.4}$$

where γ is the gyromagnetic ratio of the nuclear spin, and $\mathcal{F}_{\alpha\beta}^{(\mu)}$ is a form factor that depends on the direction of the applied field (indicated by μ), and $\alpha, \beta = \{x, y, z\}$. The coordinate system is defined such that x and y connect nearest neighbor Fe atoms. Ref. [18] derived the form factor for an As nucleus subject to an arbitrary field direction. In the paramagnetic state, one obtains (see also Ref. [23]):

$$\left(\frac{1}{T_1 T}\right)_\mu = \frac{\gamma^2}{2} \sum_{\mathbf{q}} \sum_{\alpha=x,y} \left[\bar{R}^{(\mu)} \cdot \bar{A}_{\mathbf{q}} \cdot \bar{\bar{\chi}}(\mathbf{q}) \cdot \bar{A}_{\mathbf{q}}^\dagger \cdot \left(\bar{R}^\dagger\right)\right]_{\alpha\alpha} \tag{A.5}$$

All quantities with an overbar are 3×3 matrices. The matrix $\bar{\bar{\chi}}$ is diagonal; its matrix elements are related to the magnetic susceptibility elements according to:

$$\tilde{\chi}_{\alpha\alpha}(\mathbf{q}) \equiv \lim_{\omega\to 0} \frac{Im\chi_{\alpha\alpha}(\mathbf{q},\omega)}{\hbar\omega} = \frac{1}{\Gamma}\chi_{\alpha\alpha}^2(\mathbf{q}) \tag{A.6}$$

where Γ is the Landau damping term. Furthermore, we have the hyperfine tensor:

$$\bar{A}_{\mathbf{q}} = 4\begin{pmatrix} A_{xx}\cos\left(\frac{q_x}{2}\right)\cos\left(\frac{q_y}{2}\right) & -A_{xy}\sin\left(\frac{q_x}{2}\right)\sin\left(\frac{q_y}{2}\right) & iA_{xz}\sin\left(\frac{q_x}{2}\right)\cos\left(\frac{q_y}{2}\right) \\ -A_{yx}\sin\left(\frac{q_x}{2}\right)\sin\left(\frac{q_y}{2}\right) & A_{yy}\cos\left(\frac{q_x}{2}\right)\cos\left(\frac{q_y}{2}\right) & iA_{yz}\cos\left(\frac{q_x}{2}\right)\sin\left(\frac{q_y}{2}\right) \\ iA_{zx}\sin\left(\frac{q_x}{2}\right)\cos\left(\frac{q_y}{2}\right) & iA_{zy}\cos\left(\frac{q_x}{2}\right)\sin\left(\frac{q_y}{2}\right) & A_{zz}\cos\left(\frac{q_x}{2}\right)\cos\left(\frac{q_y}{2}\right) \end{pmatrix} \tag{A.7}$$

and the rotation matrix:

$$\bar{R}^{(\mu)} = \begin{pmatrix} \sin^2\phi + \cos\theta\,\cos^2\phi & -\sin 2\phi\,\sin^2\frac{\theta}{2} & \cos\phi\,\sin\theta \\ -\sin 2\phi\,\sin^2\frac{\theta}{2} & \cos^2\phi + \cos\theta\,\sin^2\phi & \sin\phi\,\sin\theta \\ -\cos\phi\,\sin\theta & -\sin\phi\,\sin\theta & \cos\theta \end{pmatrix} \tag{A.8}$$

This is the rotation matrix to go from the basis that diagonalizes the hyperfine tensor to the crystalline basis [18]. Here, the field direction μ is described by the angles θ, ϕ according to $\hat{\mathbf{h}} = \cos\phi\sin\theta\hat{\mathbf{x}} + \sin\phi\sin\theta\hat{\mathbf{y}} + \cos\theta\hat{\mathbf{z}}$. Because the lattice distortion is very small, we consider hereafter that the hyperfine tensor remains essentially tetragonal, i.e. $A_{xx} = A_{yy}$, $A_{yz} = A_{xz}$, and $A_{xy} = A_{yx}$.

It is now straightforward to obtain the expressions for $1/\left(T_1T\right)_\mu$ for different field directions μ. We find:

$$\begin{aligned} \left(\frac{1}{T_1T}\right)_x =& 8\gamma^2\sum_{\mathbf{q}}\left[\sin^2\left(\frac{q_x}{2}\right)\sin^2\left(\frac{q_y}{2}\right)A_{xy}^2 + \sin^2\left(\frac{q_x}{2}\right)\cos^2\left(\frac{q_y}{2}\right)A_{xz}^2\right]\tilde{\chi}_{xx}\left(\mathbf{q}\right) \\ & 8\gamma^2\sum_{\mathbf{q}}\left[\cos^2\left(\frac{q_x}{2}\right)\cos^2\left(\frac{q_y}{2}\right)A_{yy}^2 + \cos^2\left(\frac{q_x}{2}\right)\sin^2\left(\frac{q_y}{2}\right)A_{yz}^2\right]\tilde{\chi}_{yy}\left(\mathbf{q}\right) \\ & 8\gamma^2\sum_{\mathbf{q}}\left[\cos^2\left(\frac{q_x}{2}\right)\sin^2\left(\frac{q_y}{2}\right)A_{yz}^2 + \cos^2\left(\frac{q_x}{2}\right)\cos^2\left(\frac{q_y}{2}\right)A_{zz}^2\right]\tilde{\chi}_{zz}\left(\mathbf{q}\right) \end{aligned} \tag{A.9}$$

$$\begin{aligned}\left(\frac{1}{T_1T}\right)_y =& 8\gamma^2\sum_{\mathbf{q}}\left[\cos^2\left(\frac{q_x}{2}\right)\cos^2\left(\frac{q_y}{2}\right)A_{xx}^2+\sin^2\left(\frac{q_x}{2}\right)\cos^2\left(\frac{q_y}{2}\right)A_{xz}^2\right]\tilde{\chi}_{xx}\left(\mathbf{q}\right)\\ & 8\gamma^2\sum_{\mathbf{q}}\left[\sin^2\left(\frac{q_x}{2}\right)\sin^2\left(\frac{q_y}{2}\right)A_{xy}^2+\cos^2\left(\frac{q_x}{2}\right)\sin^2\left(\frac{q_y}{2}\right)A_{yz}^2\right]\tilde{\chi}_{yy}\left(\mathbf{q}\right)\\ & 8\gamma^2\sum_{\mathbf{q}}\left[\sin^2\left(\frac{q_x}{2}\right)\cos^2\left(\frac{q_y}{2}\right)A_{xz}^2+\cos^2\left(\frac{q_x}{2}\right)\cos^2\left(\frac{q_y}{2}\right)A_{zz}^2\right]\tilde{\chi}_{zz}\left(\mathbf{q}\right)\end{aligned} \tag{A.10}$$

and:

$$\begin{aligned}\left(\frac{1}{T_1T}\right)_z =& 8\gamma^2\sum_{\mathbf{q}}\left[\cos^2\left(\frac{q_x}{2}\right)\cos^2\left(\frac{q_y}{2}\right)A_{xx}^2+\sin^2\left(\frac{q_x}{2}\right)\sin^2\left(\frac{q_y}{2}\right)A_{xy}^2\right]\tilde{\chi}_{xx}\left(\mathbf{q}\right)\\ & 8\gamma^2\sum_{\mathbf{q}}\left[\cos^2\left(\frac{q_x}{2}\right)\cos^2\left(\frac{q_y}{2}\right)A_{yy}^2+\sin^2\left(\frac{q_x}{2}\right)\sin^2\left(\frac{q_y}{2}\right)A_{xy}^2\right]\tilde{\chi}_{yy}\left(\mathbf{q}\right)\\ & 8\gamma^2\sum_{\mathbf{q}}\left[\sin^2\left(\frac{q_x}{2}\right)\cos^2\left(\frac{q_y}{2}\right)A_{xz}^2+\cos^2\left(\frac{q_x}{2}\right)\sin^2\left(\frac{q_y}{2}\right)A_{zz}^2\right]\tilde{\chi}_{zz}\left(\mathbf{q}\right)\end{aligned} \tag{A.11}$$

If we approximate the magnetic susceptibility as delta-functions peaked at the magnetic ordering vectors $\mathbf{Q}_1=(\pi,0)$ and $\mathbf{Q}_2=(0,\pi)$, we obtain:

$$\left(T_1T\right)_x^{-1}=\frac{8\gamma^2A_{xz}^2}{\Gamma}\left[\chi_{xx}^2\left(\mathbf{Q}_1\right)+\chi_{yy}^2\left(\mathbf{Q}_2\right)+\chi_{zz}^2\left(\mathbf{Q}_2\right)\right] \tag{A.12}$$

$$\left(T_1T\right)_y^{-1}=\frac{8\gamma^2A_{xz}^2}{\Gamma}\left[\chi_{xx}^2\left(\mathbf{Q}_1\right)+\chi_{yy}^2\left(\mathbf{Q}_2\right)+\chi_{zz}^2\left(\mathbf{Q}_1\right)\right] \tag{A.13}$$

$$\left(T_1T\right)_x^{-1}=\frac{8\gamma^2A_{xz}^2}{\Gamma}\left[\chi_{zz}^2\left(\mathbf{Q}_1\right)+\chi_{zz}^2\left(\mathbf{Q}_2\right)\right] \tag{A.14}$$

These equations can be inverted to extract the quantities:

$$\chi_{zz}^2\left(\mathbf{Q}_1\right)=\frac{\Gamma}{16\gamma^2A_{xz}^2}\left[-\left(T_1T\right)_y^{-1}\left(-\epsilon\right)+\left(T_1T\right)_y^{-1}\left(\epsilon\right)+\left(T_1T\right)_z^{-1}\left(\epsilon\right)\right] \tag{A.15}$$

$$\chi_{zz}^2\left(\mathbf{Q}_2\right)=\frac{\Gamma}{16\gamma^2A_{xz}^2}\left[\left(T_1T\right)_y^{-1}\left(-\epsilon\right)-\left(T_1T\right)_y^{-1}\left(\epsilon\right)+\left(T_1T\right)_z^{-1}\left(\epsilon\right)\right] \tag{A.16}$$

$$\chi_{xx}^2\left(\mathbf{Q}_1\right)+\chi_{yy}^2\left(\mathbf{Q}_2\right)=\frac{\Gamma}{16\gamma^2A_{xz}^2}\left[\left(T_1T\right)_y^{-1}\left(-\epsilon\right)+\left(T_1T\right)_y^{-1}\left(\epsilon\right)-\left(T_1T\right)_z^{-1}\left(\epsilon\right)\right] \tag{A.17}$$

using the fact that $(T_1T)_x^{-1}(\epsilon) = (T_1T)_y^{-1}(-\epsilon)$. These quantities are plotted in 7.2(e) of the main text.

Although useful for a qualitative analysis, this approximation neglects the important fact that the magnetic fluctuations have finite correlation length ξ. To model this effect, we consider susceptibilities peaked at $\mathbf{Q}_1$ and $\mathbf{Q}_2$, as seen by the neutron scattering experiments (the amplitude χ_0 of the susceptibilities is absorbed in Γ, for convenience) [43].

$$\begin{aligned}
\Gamma\tilde{\chi}_{xx}(\mathbf{q}) &= \frac{1}{\left[(\xi_x^{-2}-\phi_{xy})+(\cos q_x-\cos q_y+2)\right]^2}+\frac{1}{\left[\left(\xi_y^{-2}+\phi_{yx}\right)+(-\cos q_x+\cos q_y+2)\right]^2}\\
\Gamma\tilde{\chi}_{yy}(\mathbf{q}) &= \frac{1}{\left[\left(\xi_y^{-2}-\phi_{yx}\right)+(\cos q_x-\cos q_y+2)\right]^2}+\frac{1}{\left[(\xi_x^{-2}+\phi_{xy})+(-\cos q_x+\cos q_y+2)\right]^2}\\
\Gamma\tilde{\chi}_{zz}(\mathbf{q}) &= \frac{1}{\left[(\xi_z^{-2}-\phi_{zz})+(\cos q_x-\cos q_y+2)\right]^2}+\frac{1}{\left[(\xi_z^{-2}+\phi_{zz})+(-\cos q_x+\cos q_y+2)\right]^2}
\end{aligned} \tag{A.18}$$

Note that we have three different correlation lengths: ξ_x corresponds to in-plane spin fluctuations with spins parallel to the ordering vector direction; ξ_y corresponds to in-plane spin fluctuations with spins perpendicular to the ordering vector direction; and ξ_z corresponds to out-of-plane spin fluctuations. This spin anisotropy originates from the spin-orbit coupling, as shown in Ref. [69]. The nematic order parameters $\phi_{\alpha\beta}$ split the tetragonal degeneracy between $\chi_{xx}(\mathbf{Q}_1)$ and $\chi_{yy}(\mathbf{Q}_2)$, between $\chi_{xx}(\mathbf{Q}_2)$ and $\chi_{yy}(\mathbf{Q}_1)$, and between $\chi_{zz}(\mathbf{Q}_1)$ and $\chi_{zz}(\mathbf{Q}_2)$. They are related to the external strain ϵ according to the nematic susceptibilities $\chi_{\alpha\beta}^{nem}$, i.e. $\phi_{\alpha\beta} = \chi_{\alpha\beta}^{nem}\epsilon$.

Substituting these expressions in Eqs. A.9, A.10, and A.11 give:

$$\begin{aligned}
\frac{\Gamma}{8\gamma^2}\left(\frac{1}{T_1T}\right)_x =& A_{xy}^2\left[J_1\left(\xi_x^{-2}-\phi_{xy}\right)+J_1\left(\xi_y^{-2}+\phi_{yx}\right)\right]+A_{xz}^2\left[J_3\left(\xi_x^{-2}-\phi_{xy}\right)+J_2\left(\xi_y^{-2}+\phi_{yx}\right)\right]\\
&+A_{yy}^2\left[J_1\left(\xi_y^{-2}-\phi_{yx}\right)+J_1\left(\xi_x^{-2}+\phi_{xy}\right)\right]+A_{yz}^2\left[J_2\left(\xi_y^{-2}-\phi_{yx}\right)+J_3\left(\xi_x^{-2}+\phi_{xy}\right)\right]\\
&+A_{yz}^2\left[J_2\left(\xi_z^{-2}-\phi_{zz}\right)+J_3\left(\xi_z^{-2}+\phi_{zz}\right)\right]+A_{zz}^2\left[J_1\left(\xi_z^{-2}-\phi_{zz}\right)+J_1\left(\xi_z^{-2}+\phi_{zz}\right)\right]
\end{aligned} \tag{A.19}$$

as well as

$$\begin{aligned}\frac{\Gamma}{8\gamma^2}\left(\frac{1}{T_1T}\right)_y =& A_{xx}^2\left[J_1\left(\xi_x^{-2}-\phi_{xy}\right)+J_1\left(\xi_y^{-2}+\phi_{yx}\right)\right]+A_{xz}^2\left[J_3\left(\xi_x^{-2}-\phi_{xy}\right)+J_2\left(\xi_y^{-2}+\phi_{yx}\right)\right]\\ &+A_{xy}^2\left[J_1\left(\xi_y^{-2}-\phi_{yx}\right)+J_1\left(\xi_x^{-2}+\phi_{xy}\right)\right]+A_{yz}^2\left[J_2\left(\xi_y^{-2}-\phi_{yx}\right)+J_3\left(\xi_x^{-2}+\phi_{xy}\right)\right]\\ &+A_{xz}^2\left[J_3\left(\xi_z^{-2}-\phi_{zz}\right)+J_2\left(\xi_z^{-2}+\phi_{zz}\right)\right]+A_{zz}^2\left[J_1\left(\xi_z^{-2}-\phi_{zz}\right)+J_1\left(\xi_z^{-2}+\phi_{zz}\right)\right]\end{aligned} \tag{A.20}$$

$$\begin{aligned}\frac{\Gamma}{8\gamma^2}\left(\frac{1}{T_1T}\right)_z =& A_{xx}^2\left[J_1\left(\xi_x^{-2}-\phi_{xy}\right)+J_1\left(\xi_y^{-2}+\phi_{yx}\right)\right]+A_{xy}^2\left[J_1\left(\xi_x^{-2}-\phi_{xy}\right)+J_1\left(\xi_y^{-2}+\phi_{yx}\right)\right]\\ &+A_{yy}^2\left[J_1\left(\xi_y^{-2}-\phi_{yx}\right)+J_1\left(\xi_x^{-2}+\phi_{xy}\right)\right]+A_{xy}^2\left[J_1\left(\xi_y^{-2}-\phi_{yx}\right)+J_1\left(\xi_x^{-2}+\phi_{xy}\right)\right]\\ &+A_{xz}^2\left[J_3\left(\xi_z^{-2}-\phi_{zz}\right)+J_2\left(\xi_z^{-2}+\phi_{zz}\right)\right]+A_{yz}^2\left[J_2\left(\xi_z^{-2}-\phi_{zz}\right)+J_3\left(\xi_z^{-2}+\phi_{zz}\right)\right]\end{aligned} \tag{A.21}$$

Here, we defined the integrals:

$$\begin{aligned}J_1(r) &= \int_{-\pi}^{\pi}\int_{-\pi}^{\pi}\frac{dq_xdq_y}{2\pi}\frac{\cos^2\left(\frac{q_x}{2}\right)\cos^2\left(\frac{q_y}{2}\right)}{\left[r+(\cos q_x-\cos q_y+2)\right]^2}\equiv\int_{-\pi}^{\pi}\int_{-\pi}^{\pi}\frac{dq_xdq_y}{2\pi}\frac{\sin^2\left(\frac{q_x}{2}\right)\sin^2\left(\frac{q_y}{2}\right)}{\left[r+(\cos q_x-\cos q_y+2)\right]^2}\\ J_2(r) &= \int_{-\pi}^{\pi}\int_{-\pi}^{\pi}\frac{dq_xdq_y}{2\pi}\frac{\cos^2\left(\frac{q_x}{2}\right)\sin^2\left(\frac{q_y}{2}\right)}{\left[r+(\cos q_x-\cos q_y+2)\right]^2}\\ J_3(r) &= \int_{-\pi}^{\pi}\int_{-\pi}^{\pi}\frac{dq_xdq_y}{2\pi}\frac{\sin^2\left(\frac{q_x}{2}\right)\cos^2\left(\frac{q_y}{2}\right)}{\left[r+(\cos q_x-\cos q_y+2)\right]^2}\end{aligned} \tag{A.22}$$

In the limit $\xi_i^{-2}\pm\phi_{\alpha\beta}\ll 1$, we can approximate the integrals by expanding the integrand near $(\pi,0)$, yielding:

$$\begin{aligned}J_1(r) &\approx \frac{1}{4\pi}\ln\left(\frac{\Lambda_1}{\sqrt{r}}\right)\\ J_2(r) &\approx \frac{1}{8\pi}\left[1-\frac{r}{2}\ln\left(\frac{\Lambda_2}{\sqrt{r}}\right)\right]\\ J_3(r) &\approx \frac{1}{2\pi r}\end{aligned} \tag{A.23}$$

where $\Lambda_1 \approx 1.45$, and $\Lambda_2 \approx 3.2$ for $r < 0.5$, according to numerical evaluations of the integrals. Note that, as expected from symmetry considerations, $(T_1T)_x^{-1}(-\epsilon) = (T_1T)_y^{-1}(\epsilon)$ and $(T_1T)_z^{-1}(-\epsilon) = (T_1T)_z^{-1}(\epsilon)$.

A.3 Fitting The Spin-Lattice Relaxation Rate Data

The expressions for $(T_1T)_\alpha^{-1}$ given above depend on six parameters: ξ_x, ξ_y, ξ_z, ϕ_{xy}, ϕ_{yx}, and ϕ_{zz}. We first fit the zero-strain data shown in Figs. 7.2(b) and 7.2(d) of the main text assuming all the $\phi_{\alpha\beta} = 0$, and that $\xi_y = \xi_x$. Because the Landau damping term, Γ, is unknown, one cannot simply extract the $\xi_{x,z}$ directly from the data. However, the ratio of $(T_1T)_x^{-1} / (T_1T)_z^{-1}$ does constrain the data and enable us to fit the data using the temperature-dependent correlation lengths shown in Fig. 7.4(a) of the main text. The hyperfine coupling constants are given by: $A_{xx} = A_{yy} = 0.66T/\mu_B$, $A_{zz} = 0.47T/\mu_B$, and $A_{xz} = A_{yz} = 0.43T/\mu_B$ [4], and we assume the value $A_{xy} = 0.33T/\mu_B$[23].

Using these values for $\xi_{x,z}$ and assuming that $\xi_y = \xi_x$, we then proceed to fit the strain-dependent $(T_1T)^{-1}$ data to the three nematic order parameters, $\phi_{xy} = \chi_{xy}^{nem}\epsilon$, $\phi_{yx} = \chi_{yx}^{nem}\epsilon$, and $\phi_{zz} = \chi_{zz}^{nem}\epsilon$ where the $\chi_{\alpha\beta}^{nem}$ are the static nematic susceptibilities of the three components of the nematic order. These data are shown in Fig. 7.4(b) of the main text as a function of temperature.

A.4 Sample Characterization and Resistivity Anisotropy

In Fig. A.1 we plot the resistivity of the two samples used in this study (in $H \parallel a$ and $H \parallel c$ configurations). The samples had residual resistivity ratios (RRR)) of 7.1 and 6.2, respectively, with very similar $\rho(T)$ temperature dependences. For reference we show the temperature-dependent resistivity of As-grown samples studied by Tanatar et al. [3] with residual resistivity ratio ~ 3, and long-term annealed samples with residual resistivity ratio of ~ 30 [8]. Reducing residual resistivity in the samples leads to an increase of the structural

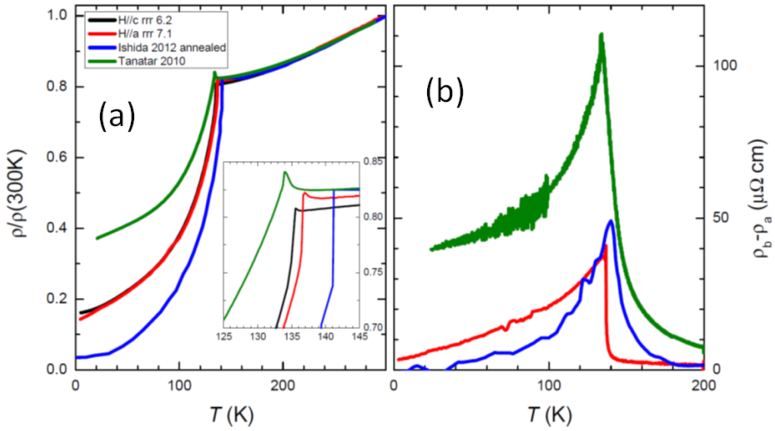

Figure A.1: Resistivity Versus Temperature of Measured Samples. (a) Temperature-dependent electrical resistivity $\rho(T)$, of the samples used in this work for $H \parallel a$ and $H \parallel c$ configurations, shown using a normalized $\rho/\rho(300K)$ scale. For reference we show data on as-grown samples (Green, Tanatar *et al.* [3][2]), and on annealed samples (Blue, Ishida *et al.* [8]). The inset shows the same data focusing on the structural/magnetic transition, revealing a systematic shift of the T_s feature to higher temperatures with increase of residual resistivity ratio. (b) The in-plane resistivity difference $\rho_b - \rho_a$ in the orthorhombic phase for the same samples.

transition temperature, as shown in inset in the left panel. For the two samples studied T_s was 136.7K ($H \parallel a$) and 135.6K ($H \parallel c$), intermediate between low and high residual resistivity ratio samples.

In the right panel of Fig. A.1 we plot the difference of the principal components of the in-plane resistivity in the orthorhombic phase, $\rho_b - \rho_a$, for low (green line, RRR$\sim$ 3, Ref. [3]) and high (blue line, RRR$\sim$ 30, Ref. [8]) residual resistivity ratio samples. While in the former a big anisotropy is found in the $T = 0$ limit, negligible anisotropy is found in the later. The samples used in this study show negligible difference in $T = 0$ limit, similar to high quality samples.

This sample characterization suggests that the samples used in this study do not reveal extrinsic high anisotropy in $T = 0$ limit. They are representative of high quality annealed samples. Comparisons of the difference curves for annealed samples [8] and samples of our study reveal comparable differences in magnitude at the maximum immediately below T_s, supporting this conclusion.

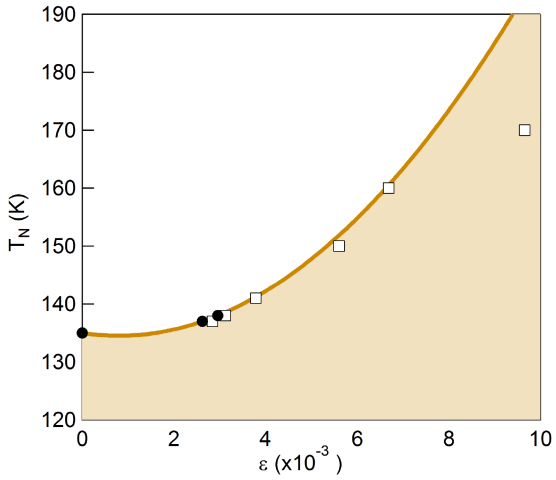

Figure A.2: T_N Versus Strain. T_N versus strain measured directly (solid black circles) and based on the measured fit parameters for ξ_a and χ_{xy}^{nem} (open squares). The solid line is a guide to the eye.

A.5 Enhancement of T_N Under Strain

Fig. A.2 shows T_N versus strain for three data points based on our observations of the NMR spectra for $\mathbf{H}_0 \perp \mathbf{c}$. When the system orders antiferromagnetically, a static internal field develops along the $\mathbf{c}$ axis that shifts the resonance frequency. The strain and temperature values shown in the figure represent the points where we observe shifts of the spectrum consistent with the presence of such a field. This behavior arises because the large nematic susceptibility increases the correlation length, ξ, which gives rise to a non-linear effect in which T_N is enhanced by strain. In fact, one can estimate the strain dependence of T_N because χ diverges when $\xi_x^{-2}(T) - \chi_{xy}^{nem}(T)\,\epsilon = 0$. Using the fitted parameters for ξ_x and χ_{xy}^{nem} we estimate T_N versus ϵ, and the result agrees well with the measured values. These results agree with previous neutron scattering studies [74].

References

[1] A. P. Dioguardi, *Nuclear Magnetic Resonance Studies of the 122 Iron-Based Superconductors*, Ph.D. thesis, University of California, Davis (2013).

[2] W. W. Warren and W. G. Clark, Knight Shift and Nuclear Spin-Lattice Relaxation Rate in Solid and Liquid Copper **1**, 24 (1970).

[3] M. A. Tanatar, E. C. Blomberg, A. Kreyssig, M. G. Kim, N. Ni, A. Thaler, S. L. Bud'ko, P. C. Canfield, A. I. Goldman, I. I. Mazin, and R. Prozorov, Uniaxial-strain mechanical detwinning ofCaFe2As2andBaFe2As2crystals: Optical and transport study, *Physical Review B* **81** (2010).

[4] K. Kitagawa, N. Katayama, K. Ohgushi, M. Yoshida, and M. Takigawa, Commensurate Itinerant Antiferromagnetism in BaFe2As2:75As-NMR Studies on a Self-Flux Grown Single Crystal, *Journal of the Physical Society of Japan* **77**, 114709 (2008).

[5] Y. Gallais, R. M. Fernandes, I. Paul, L. Chauvière, Y.-X. Yang, M.-A. Méasson, M. Cazayous, A. Sacuto, D. Colson, and A. Forget, Observation of Incipient Charge Nematicity inBa(Fe1-XCoX)2As2, *Physical Review Letters* **111** (2013).

[6] Y. Gallais and I. Paul, Charge nematicity and electronic Raman scattering in iron-based superconductors, *Comptes Rendus Physique* **17**, 113 (2016).

[7] J.-H. Chu, H.-H. Kuo, J. G. Analytis, and I. R. Fisher, Divergent Nematic Susceptibility in an Iron Arsenide Superconductor, *Science* **337**, 710 (2012).

[8] S. Ishida, T. Liang, M. Nakajima, K. Kihou, C. H. Lee, A. Iyo, H. Eisaki, T. Kakeshita, T. Kida, M. Hagiwara, Y. Tomioka, T. Ito, and S. Uchida, Manifestations of multiple-carrier charge transport in the magnetostructurally ordered phase of BaFe2As2, *Physical Review B* **84** (2011).

[9] B. Cowan, *Nuclear Magnetic Resonance and Relaxation* (Cambridge University Press, 1997).

[10] P. C. Canfield and S. L. Bud'Ko, FeAs-based superconductivity: a case study of the effects of transition metal doping on BaFe2As2, *Annu. Rev. Condens. Matter Phys.* **1**, 27 (2010).

[11] R. M. Fernandes, A. V. Chubukov, J. Knolle, I. Eremin, and J. Schmalian, Preemptive nematic order, pseudogap, and orbital order in the iron pnictides, *Physical Review B* **85** (2012).

[12] C. P. Slichter, *Principles of magnetic resonance* (Springer Science & Business Media, 1989), 3rd edition.

[13] C. Kittel, P. McEuen, and P. McEuen, *Introduction to solid state physics*, vol. 8 (Wiley New York, 1996).

[14] R. K. Wangsness, Geometrical Solution for a Nuclear Moment in a Magnetic Field, *American Journal of Physics* **21**, 274 (1953).

[15] E. L. Hahn, Spin Echoes, *Physical Review* **80**, 580 (1950).

[16] W. D. Knight, Nuclear Magnetic Resonance Shift in Metals, *Physical Review* **76**, 1259 (1949).

[17] G. C. Carter, L. H. Bennett, and D. Kahan, Metallic Shifts in NMR. A Review of the Theory and Comprehensive Critical Data Compilation of Metallic Materials. Part I. Review Chapters NMR Tables, Evaluated Knight Shifts in Metals Together with

other Solid State and Nuclear Properties, Technical report, NATIONAL STANDARD REFERENCE DATA SYSTEM (1977).

[18] A. Smerald and N. Shannon, Angle-resolved NMR: Quantitative theory of75AsT1relaxation rate in BaFe2As2, *Physical Review B* **84** (2011).

[19] T. Moriya, The Effect of Electron-Electron Interaction on the Nuclear Spin Relaxation in Metals, *Journal of the Physical Society of Japan* **18**, 516 (1963).

[20] H. Choi, I. Vinograd, C. Chaffey, and N. Curro, Inverse Laplace transformation analysis of stretched exponential relaxation **331**, 107050 (2021).

[21] D. C. Johnston, Stretched exponential relaxation arising from a continuous sum of exponential decays, *Physical Review B* **74** (2006).

[22] T. Shiroka, F. Casola, J. Mesot, W. Bachmann, and H.-R. Ott, A two-axis goniometer for low-temperature nuclear magnetic resonance measurements on single crystals, *Review of Scientific Instruments* **83**, 093901 (2012).

[23] T. Kissikov, A. P. Dioguardi, E. I. Timmons, M. A. Tanatar, R. Prozorov, S. L. Bud'ko, P. C. Canfield, R. M. Fernandes, and N. J. Curro, NMR study of nematic spin fluctuations in a detwinned single crystal of underdoped $Ba(Fe_{1-x}Co_x)_2As_2$, *Physical Review B* **94** (2016).

[24] C. W. Hicks, M. E. Barber, S. D. Edkins, D. O. Brodsky, and A. P. Mackenzie, Piezoelectric-based apparatus for strain tuning, *Review of Scientific Instruments* **85**, 065003 (2014).

[25] N. Ni, A. Thaler, J. Q. Yan, A. Kracher, E. Colombier, S. L. Bud'ko, P. C. Canfield, and S. T. Hannahs, Temperature versus doping phase diagrams forBa(Fe1-xTMx)2As2(TM=Ni,Cu,Cu/Co)single crystals, *Physical Review B* **82** (2010).

[26] T. Kissikov, R. Sarkar, M. Lawson, B. T. Bush, E. I. Timmons, M. A. Tanatar, R. Prozorov, S. L. Bud'ko, P. C. Canfield, R. M. Fernandes, and N. J. Curro, Uniaxial strain control of spin-polarization in multicomponent nematic order of $BaFe_2As_2$, *Nature Communications* **9** (2018).

[27] Y. Schattner, S. Lederer, S. A. Kivelson, and E. Berg, Ising Nematic Quantum Critical Point in a Metal: A Monte Carlo Study, *Physical Review X* **6** (2016).

[28] S. Lederer, Y. Schattner, E. Berg, and S. Kivelson, Enhancement of Superconductivity near a Nematic Quantum Critical Point, *Physical Review Letters* **114** (2015).

[29] J. F. Nye, *Physical Properties of Crystals* (Oxford University Press, 1985).

[30] P. Malinowski, Q. Jiang, J. J. Sanchez, J. Mutch, Z. Liu, P. Went, J. Liu, P. J. Ryan, J.-W. Kim, and J.-H. Chu, Suppression of superconductivity by anisotropic strain near a nematic quantum critical point, *Nature Physics* **16**, 1189 (2020).

[31] J.-H. Chu, J. G. Analytis, K. D. Greve, P. L. McMahon, Z. Islam, Y. Yamamoto, and I. R. Fisher, In-Plane Resistivity Anisotropy in an Underdoped Iron Arsenide Superconductor, *Science* **329**, 824 (2010).

[32] R. M. Fernandes, L. H. VanBebber, S. Bhattacharya, P. Chandra, V. Keppens, D. Mandrus, M. A. McGuire, B. C. Sales, A. S. Sefat, and J. Schmalian, Effects of Nematic Fluctuations on the Elastic Properties of Iron Arsenide Superconductors, *Physical Review Letters* **105** (2010).

[33] A. Böhmer, T. Arai, F. Hardy, T. Hattori, T. Iye, T. Wolf, H. Löhneysen, K. Ishida, and C. Meingast, Origin of the Tetragonal-to-Orthorhombic Phase Transition in FeSe: A Combined Thermodynamic and NMR Study of Nematicity, *Physical Review Letters* **114** (2015).

[34] M. He, L. Wang, F. Ahn, F. Hardy, T. Wolf, P. Adelmann, J. Schmalian, I. Eremin, and C. Meingast, Dichotomy between in-plane magnetic susceptibility and resistivity anisotropies in extremely strained BaFe2As2, *Nature Communications* **8** (2017).

[35] A. E. Böhmer and C. Meingast, Electronic nematic susceptibility of iron-based superconductors, *Comptes Rendus Physique* **17**, 90 (2016).

[36] S. Jiang, H. S. Jeevan, J. Dong, and P. Gegenwart, Thermopower as a Sensitive Probe of Electronic Nematicity in Iron Pnictides, *Physical Review Letters* **110** (2013).

[37] E. C. Blomberg, A. Kreyssig, M. A. Tanatar, R. M. Fernandes, M. G. Kim, A. Thaler, J. Schmalian, S. L. Bud'ko, P. C. Canfield, A. I. Goldman, and R. Prozorov, Effect of tensile stress on the in-plane resistivity anisotropy in BaFe2As2, *Physical Review B* **85** (2012).

[38] M. Tanatar, A. Böhmer, E. Timmons, M. Schütt, G. Drachuck, V. Taufour, K. Kothapalli, A. Kreyssig, S. Bud'ko, P. Canfield, R. Fernandes, and R. Prozorov, Origin of the Resistivity Anisotropy in the Nematic Phase of FeSe, *Physical Review Letters* **117** (2016).

[39] C. Mirri, A. Dusza, S. Bastelberger, M. Chinotti, L. Degiorgi, J.-H. Chu, H.-H. Kuo, and I. Fisher, Origin of the Resistive Anisotropy in the Electronic Nematic Phase of-BaFe2As2Revealed by Optical Spectroscopy, *Physical Review Letters* **115** (2015).

[40] F. L. Ning, M. Fu, D. A. Torchetti, T. Imai, A. S. Sefat, P. Cheng, B. Shen, and H.-H. Wen, Critical behavior of the spin density wave transition in underdopedBa(Fe1-xCox)2As2(x≤0.05):As75NMR investigation, *Physical Review B* **89** (2014).

[41] P. Dai, Antiferromagnetic order and spin dynamics in iron-based superconductors, *Reviews of Modern Physics* **87**, 855 (2015).

[42] H. Man, X. Lu, J. S. Chen, R. Zhang, W. Zhang, H. Luo, J. Kulda, A. Ivanov, T. Keller, E. Morosan, Q. Si, and P. Dai, Electronic nematic correlations in the stress-free tetragonal state ofBaFe2-xNixAs2, *Physical Review B* **92** (2015).

[43] X. Lu, J. T. Park, R. Zhang, H. Luo, A. H. Nevidomskyy, Q. Si, and P. Dai, Nematic spin correlations in the tetragonal state of uniaxial-strained BaFe2-xNixAs2, *Science* **345**, 657 (2014).

[44] T. Iye, M.-H. Julien, H. Mayaffre, M. Horvatić, C. Berthier, K. Ishida, H. Ikeda, S. Kasahara, T. Shibauchi, and Y. Matsuda, Emergence of Orbital Nematicity in the Tetragonal Phase of BaFe2(As1-xPx)2, *Journal of the Physical Society of Japan* **84**, 043705 (2015).

[45] T. Kissikov, R. Sarkar, B. T. Bush, M. Lawson, P. C. Canfield, and N. J. Curro, Nuclear magnetic resonance probe head design for precision strain control, *Review of Scientific Instruments* **88**, 103902 (2017).

[46] A. Dioguardi, T. Kissikov, C. Lin, K. Shirer, M. Lawson, H.-J. Grafe, J.-H. Chu, I. Fisher, R. Fernandes, and N. Curro, NMR Evidence for Inhomogeneous Nematic Fluctuations inBaFe2(As1-xPx)2, *Physical Review Letters* **116** (2016).

[47] H.-H. Kuo, J.-H. Chu, J. C. Palmstrom, S. A. Kivelson, and I. R. Fisher, Ubiquitous signatures of nematic quantum criticality in optimally doped Fe-based superconductors, *Science* **352**, 958 (2016).

[48] N. Ni, S. L. Bud'ko, A. Kreyssig, S. Nandi, G. E. Rustan, A. I. Goldman, S. Gupta, J. D. Corbett, A. Kracher, and P. C. Canfield, Anisotropic thermodynamic and transport properties of single-crystallineBa1-xKxFe2As2(x=0and 0.45), *Physical Review B* **78** (2008).

[49] V. K. Thorsmølle, M. Khodas, Z. P. Yin, C. Zhang, S. V. Carr, P. Dai, and G. Blumberg, Critical quadrupole fluctuations and collective modes in iron pnictide superconductors, *Physical Review B* **93** (2016).

[50] P. Blaha, K. Schwarz, G. Madsen, D. Kvasnicka, and J. Luitz, WIEN2k: An Augmented Plane Wave plus Local Orbitals Program for Calculating Crystal Properties, *Technische Universität Wien, Wien* **28** (2001).

[51] J. P. Perdew, K. Burke, and M. Ernzerhof, Generalized Gradient Approximation Made Simple, *Physical Review Letters* **77**, 3865 (1996).

[52] R. Mittal, S. K. Mishra, S. L. Chaplot, S. V. Ovsyannikov, E. Greenberg, D. M. Trots, L. Dubrovinsky, Y. Su, T. Brueckel, S. Matsuishi, H. Hosono, and G. Garbarino, Ambient- and low-temperature synchrotron x-ray diffraction study of BaFe2As2and CaFe2As2at high pressures up to 56 GPa, *Physical Review B* **83** (2011).

[53] H.-J. Grafe, G. Lang, F. Hammerath, D. Paar, K. Manthey, K. Koch, H. Rosner, N. J. Curro, G. Behr, J. Werner, N. Leps, R. Klingeler, H.-H. Klauss, F. J. Litterst, and B. Büchner, Electronic properties of LaO1-xFxFeAs in the normal state probed by NMR/NQR, *New Journal of Physics* **11**, 035002 (2009).

[54] J. Cui, Q.-P. Ding, W. R. Meier, A. E. Böhmer, T. Kong, V. Borisov, Y. Lee, S. L. Bud'ko, R. Valentí, P. C. Canfield, and Y. Furukawa, Magnetic fluctuations and superconducting properties of CaKFe4As4 studied by As75 NMR, *Physical Review B* **96** (2017).

[55] M. Yi, D. H. Lu, R. G. Moore, K. Kihou, C.-H. Lee, A. Iyo, H. Eisaki, T. Yoshida, A. Fujimori, and Z.-X. Shen, Electronic reconstruction through the structural and magnetic transitions in detwinned NaFeAs, *New Journal of Physics* **14**, 073019 (2012).

[56] F. L. Ning, K. Ahilan, T. Imai, A. S. Sefat, R. Jin, M. A. McGuire, B. C. Sales, and D. Mandrus, C59oandA75sNMR investigation of lightly dopedBa(Fe1-xCox)2As2(x=0.02,0.04), *Physical Review B* **79** (2009).

[57] A. P. Dioguardi, N. apRoberts Warren, A. C. Shockley, S. L. Bud'ko, N. Ni, P. C. Canfield, and N. J. Curro, Local magnetic inhomogeneities inBa(Fe1-xNix)2As2as seen viaA75sNMR, *Physical Review B* **82** (2010).

[58] H. Takeda, T. Imai, M. Tachibana, J. Gaudet, B. D. Gaulin, B. I. Saparov, and A. S. Sefat, Cu Substitution Effects on the Local Magnetic Properties ofBa(Fe1-xCux)2As2: A Site-SelectiveAs75andCu63NMR Study, *Physical Review Letters* **113** (2014).

[59] K. Park, D. Louca, A. Llobet, and J.-Q. Yan, Evidence of local disorder in the overdoped regime of Ba(Fe1-xCox)2As2, *Physical Review B* **84** (2011).

[60] S. Kasahara, H. J. Shi, K. Hashimoto, S. Tonegawa, Y. Mizukami, T. Shibauchi, K. Sugimoto, T. Fukuda, T. Terashima, A. H. Nevidomskyy, and Y. Matsuda, Electronic nematicity above the structural and superconducting transition in BaFe2(As1-xP x)2, *Nature* **486**, 382 (2012).

[61] E. P. Rosenthal, E. F. Andrade, C. J. Arguello, R. M. Fernandes, L. Y. Xing, X. C. Wang, C. Q. Jin, A. J. Millis, and A. N. Pasupathy, Visualization of electron nematicity and unidirectional antiferroic fluctuations at high temperatures in NaFeAs, *Nature Physics* **10**, 225 (2014).

[62] G. Lang, H.-J. Grafe, D. Paar, F. Hammerath, K. Manthey, G. Behr, J. Werner, and B. Büchner, Nanoscale Electronic Order in Iron Pnictides, *Physical Review Letters* **104** (2010).

[63] J. Kang and R. M. Fernandes, Superconductivity in FeSe Thin Films Driven by the Interplay between Nematic Fluctuations and Spin-Orbit Coupling, *Physical Review Letters* **117** (2016).

[64] A. P. Dioguardi, J. Crocker, A. C. Shockley, C. H. Lin, K. R. Shirer, D. M. Nisson, M. M. Lawson, N. apRoberts Warren, P. C. Canfield, S. L. Bud'ko, S. Ran, and N. J.

Curro, Coexistence of Cluster Spin Glass and Superconductivity in $Ba(Fe_{1-x}Co_x)_2As_2$ for 0.060≤x≤0.071, *Physical Review Letters* **111** (2013).

[65] N. Ni, M. E. Tillman, J.-Q. Yan, A. Kracher, S. T. Hannahs, S. L. Bud'ko, and P. C. Canfield, Effects of Co substitution on thermodynamic and transport properties and anisotropicHc2inBa(Fe1-xCox)2As2single crystals, *Physical Review B* **78** (2008).

[66] R. M. Fernandes and A. V. Chubukov, Low-energy microscopic models for iron-based superconductors: a review **80**, 014503 (2016).

[67] S. V. Borisenko, D. V. Evtushinsky, Z.-H. Liu, I. Morozov, R. Kappenberger, S. Wurmehl, B. Büchner, A. N. Yaresko, T. K. Kim, M. Hoesch, T. Wolf, and N. D. Zhigadlo, Direct observation of spin–orbit coupling in iron-based superconductors, *Nature Physics* **12**, 311 (2015).

[68] V. Cvetkovic and O. Vafek, Space group symmetry, spin-orbit coupling, and the low-energy effective Hamiltonian for iron-based superconductors, *Physical Review B* **88** (2013).

[69] M. H. Christensen, J. Kang, B. M. Andersen, I. Eremin, and R. M. Fernandes, Spin reorientation driven by the interplay between spin-orbit coupling and Hund's rule coupling in iron pnictides, *Physical Review B* **92** (2015).

[70] D. S. Inosov, J. T. Park, P. Bourges, D. L. Sun, Y. Sidis, A. Schneidewind, K. Hradil, D. Haug, C. T. Lin, B. Keimer, and V. Hinkov, Normal-state spin dynamics and temperature-dependent spin-resonance energy in optimally doped BaFe1.85Co0.15As2, *Nature Physics* **6**, 178 (2009).

[71] G. S. Tucker, R. M. Fernandes, H.-F. Li, V. Thampy, N. Ni, D. L. Abernathy, S. L. Bud'ko, P. C. Canfield, D. Vaknin, J. Schmalian, and R. J. McQueeney, Magnetic excitations in underdoped Ba(Fe1-xCox)2As2withx=0.047, *Physical Review B* **86** (2012).

[72] R. M. Fernandes and J. Schmalian, Manifestations of nematic degrees of freedom in the magnetic, elastic, and superconducting properties of the iron pnictides, *Superconductor Science and Technology* **25**, 084005 (2012).

[73] Q. Zhang, R. M. Fernandes, J. Lamsal, J. Yan, S. Chi, G. S. Tucker, D. K. Pratt, J. W. Lynn, R. McCallum, P. C. Canfield, T. A. Lograsso, A. I. Goldman, D. Vaknin, and R. J. McQueeney, Neutron-Scattering Measurements of Spin Excitations in LaFeAsO andBa(Fe0.953Co0.047)2As2: Evidence for a Sharp Enhancement of Spin Fluctuations by Nematic Order, *Physical Review Letters* **114** (2015).

[74] C. Dhital, T. Hogan, Z. Yamani, R. J. Birgeneau, W. Tian, M. Matsuda, A. S. Sefat, Z. Wang, and S. D. Wilson, Evolution of antiferromagnetic susceptibility under uniaxial pressure in Ba(Fe1-xCox)2As2, *Physical Review B* **89** (2014).

[75] Y. Laplace, J. Bobroff, F. Rullier-Albenque, D. Colson, and A. Forget, Atomic coexistence of superconductivity and incommensurate magnetic order in the pnictideBa(Fe1-xCox)2As2, *Physical Review B* **80** (2009).

[76] P. Bonville, F. Rullier-Albenque, D. Colson, and A. Forget, Incommensurate spin density wave in Co-doped BaFe 2 As 2, *EPL (Europhysics Letters)* **89**, 67008 (2010).

[77] L. P. Gor'kov and G. B. Teitel'baum, Spatial inhomogeneities in iron pnictide superconductors: The formation of charge stripes, *Physical Review B* **82** (2010).

[78] M. G. Kim, A. Kreyssig, Y. B. Lee, J. W. Kim, D. K. Pratt, A. Thaler, S. L. Bud'ko, P. C. Canfield, B. N. Harmon, R. J. McQueeney, and A. I. Goldman, Commensurate antiferromagnetic ordering inBa(Fe1-xCox)2As2determined by x-ray resonant magnetic scattering at theFe Kedge, *Physical Review B* **82** (2010).

[79] D. K. Pratt, M. G. Kim, A. Kreyssig, Y. B. Lee, G. S. Tucker, A. Thaler, W. Tian, J. L. Zarestky, S. L. Bud'ko, P. C. Canfield, B. N. Harmon, A. I. Gold-

man, and R. J. McQueeney, Incommensurate Spin-Density Wave Order in Electron-DopedBaFe2As2Superconductors, *Physical Review Letters* **106** (2011).

[80] Y. Song, X. Lu, D. L. Abernathy, D. W. Tam, J. L. Niedziela, W. Tian, H. Luo, Q. Si, and P. Dai, Energy dependence of the spin excitation anisotropy in uniaxial-strainedBaFe1.9Ni0.1As2, *Physical Review B* **92** (2015).

[81] M. Fu, D. A. Torchetti, T. Imai, F. L. Ning, J.-Q. Yan, and A. S. Sefat, NMR Search for the Spin Nematic State in a LaFeAsO Single Crystal, *Physical Review Letters* **109** (2012).

[82] A. P. Dioguardi, M. M. Lawson, B. T. Bush, J. Crocker, K. R. Shirer, D. M. Nisson, T. Kissikov, S. Ran, S. L. Bud'ko, P. C. Canfield, S. Yuan, P. L. Kuhns, A. P. Reyes, H.-J. Grafe, and N. J. Curro, NMR evidence for inhomogeneous glassy behavior driven by nematic fluctuations in iron arsenide superconductors, *Physical Review B* **92** (2015).

[83] R. Zhou, L. Y. Xing, X. C. Wang, C. Q. Jin, and G. qing Zheng, Orbital order and spin nematicity in the tetragonal phase of the electron-doped iron pnictidesNaFe1-xCoxAs, *Physical Review B* **93** (2016).

[84] S. Liang, A. Moreo, and E. Dagotto, Nematic State of Pnictides Stabilized by Interplay between Spin, Orbital, and Lattice Degrees of Freedom, *Physical Review Letters* **111** (2013).

[85] H. Luo, M. Wang, C. Zhang, X. Lu, L.-P. Regnault, R. Zhang, S. Li, J. Hu, and P. Dai, Spin Excitation Anisotropy as a Probe of Orbital Ordering in the Paramagnetic Tetragonal Phase of SuperconductingBaFe1.904Ni0.096As2, *Physical Review Letters* **111** (2013).

[86] Y. Song, H. Man, R. Zhang, X. Lu, C. Zhang, M. Wang, G. Tan, L.-P. Regnault, Y. Su, J. Kang, R. M. Fernandes, and P. Dai, Spin anisotropy due to spin-orbit coupling in optimally hole-dopedBa0.67K0.33Fe2As2, *Physical Review B* **94** (2016).

[87] Z. Li, D. L. Sun, C. T. Lin, Y. H. Su, J. P. Hu, and G. qing Zheng, Nodeless energy gaps of single-crystalline Ba0.68K0.32Fe2As2as seen viaAs75NMR, *Physical Review B* **83** (2011).

[88] J. Cui, P. Wiecki, S. Ran, S. L. Bud'ko, P. C. Canfield, and Y. Furukawa, Coexistence of antiferromagnetic and ferromagnetic spin correlations in Ca(Fe1-xCox)2As2 revealed by As75 nuclear magnetic resonance, *Physical Review B* **94** (2016).

[89] N. Qureshi, P. Steffens, S. Wurmehl, S. Aswartham, B. Büchner, and M. Braden, Local magnetic anisotropy in BaFe2As2: A polarized inelastic neutron scattering study, *Physical Review B* **86** (2012).

[90] C. Wang, R. Zhang, F. Wang, H. Luo, L. P. Regnault, P. Dai, and Y. Li, Longitudinal Spin Excitations and Magnetic Anisotropy in Antiferromagnetically OrderedBaFe2As2, *Physical Review X* **3** (2013).

[91] Y. Song, L.-P. Regnault, C. Zhang, G. Tan, S. V. Carr, S. Chi, A. D. Christianson, T. Xiang, and P. Dai, In-plane spin excitation anisotropy in the paramagnetic state of NaFeAs, *Physical Review B* **88** (2013).

[92] P. Liu, M. L. Klemm, L. Tian, X. Lu, Y. Song, D. W. Tam, K. Schmalzl, J. T. Park, Y. Li, G. Tan, Y. Su, F. Bourdarot, Y. Zhao, J. W. Lynn, R. J. Birgeneau, and P. Dai, In-plane uniaxial pressure-induced out-of-plane antiferromagnetic moment and critical fluctuations in BaFe2As2 **11** (2020).

[93] S.-H. Baek, D. V. Efremov, J. M. Ok, J. S. Kim, J. van den Brink, and B. Büchner, Orbital-driven nematicity in FeSe, *Nature Materials* **14**, 210 (2014).

[94] G. S. Tucker, R. M. Fernandes, D. K. Pratt, A. Thaler, N. Ni, K. Marty, A. D. Christianson, M. D. Lumsden, B. C. Sales, A. S. Sefat, S. L. Bud'ko, P. C. Canfield, A. Kreyssig, A. I. Goldman, and R. J. McQueeney, Crossover from spin waves to diffusive spin excitations in underdoped Ba(Fe1-xCox)2As2, *Physical Review B* **89** (2014).

[95] Y. Li, W. Wang, Y. Song, H. Man, X. Lu, F. Bourdarot, and P. Dai, Spin excitation anisotropy in the paramagnetic tetragonal phase of BaFe2As2, *Physical Review B* **96** (2017).

[96] M. Ma, P. Bourges, Y. Sidis, Y. Xu, S. Li, B. Hu, J. Li, F. Wang, and Y. Li, Prominent Role of Spin-Orbit Coupling in FeSe Revealed by Inelastic Neutron Scattering, *Physical Review X* **7** (2017).